Magnetoelastic Couplings in Epitaxial Cu/Ni/Cu/Si(001) Thin Films

by

Kin Ha

Bachelor of Science in Applied Physics
Bachelor of Science in Economics
California Institute of Technology (1990)

Submitted to the Department of Materials Science and Engineering
in partial fulfillment of the requirements for the degree of

Doctor of Philosophy in Electronic Materials

at the

Massachusetts Institute of Technology

June 1999

Author .....
Department of Materials Science and Engineering
April 30, 1999

Certified by .....
Robert C. O'Handley
Senior Research Scientist
Thesis Supervisor

Certified by .....
Eugene A. Fitzgerald
Associate Professor of Electronic Materials
Thesis Supervisor

Accepted by .....
Linn W. Hobbs
John F. Elliott Professor of Materials
Chairman, Department Committee on Graduate Students

Magnetoelastic Couplings in Epitaxial Cu/Ni/Cu/Si(001) Thin Films

by

Kin Ha

Submitted to the Department of Materials Science and Engineering
on April 30, 1999, in partial fulfillment of the
requirements for the degree of
Doctor of Philosophy in Electronic Materials

Abstract

Magnetoelastic coupling interactions in epitaxial Cu/Ni(t_{Ni})/Cu/Si(001) thin films as a function of the nickel film thickness (30Å $\leq t_{Ni} \leq$ 2000Å) are studied. The coupling coefficients are found by fitting the magnetic anisotropy data taken by a torque magnetometer. The spin-pair model is used to describe the intrinsic magnetic anisotropy which includes second-order magnetoelastic terms. The coefficients are found to deviate much from those of bulk nickel. For some, they even change sign. The deviations are due to large residual strains in the nickel layer. An effective magnetoelastic coefficient (B_{11}^{eff}) is also measured directly using a cantilever beam technique. The two results are in good agreement for the nickel films that are under a biaxial tensile strain of 1% or less.

Thesis Supervisor: Robert C. O'Handley
Title: Senior Research Scientist

Thesis Supervisor: Eugene A. Fitzgerald
Title: Associate Professor of Electronic Materials

To my sister, Judy,

who has not yet much,

who just gives and gives.

Acknowledgements

This thesis is not just the product of my many days of long hours at MIT, but is also the work of the many people whom I have had the fortune to know; directly or indirectly, through their teachings, sacrifices, and love, they have shown me the way. I would like to take this opportunity to thank them, to let them know that their effort has not been wasted.

I would like first to thank my thesis supervisor, Dr. Robert C. O'Handley, for believing in me, even at times when my research was in a slump. He always puts humanity above science. From him, I have learned much about magnetism and about becoming a humanist.

I would also like to thank members of my thesis committee for their time and interest in my research; specifically, Professor Eugene A. Fitzgerald for showing me the power of an engineering mind; Professor Craig W. Carter for keeping me on my toes; Professor Caroline A. Ross for her confidence in my work.

There are many members of the MIT Magnetism Group (past and present) whose help I would like to acknowledge: Dr. Heather E. Inglefield for showing me how to run the MBE system, which she did with a smile, even during her busiest time; Dr. Donna S. Chuang for teaching me the spin-pair model during the early stage of my thesis research; Dr. Craig Ballentine for showing me good measurement techniques; Dr. Gabriel Bochi for helping me study for the general exam; Dr. Chang-Kyung Kim for the many good laughs in the lab; Dr. Miguel Ciria for fruitful discussions on the subject of magnetostriction and for showing me that Two is more than two; Mr. Mathews Faranelli for being willing to help in the lab; Mr. Robin Lippincott for lending me his good ears when I needed them and for helping me exercise the other side of my brain.

I would like to thank many of my Belmont high school teachers who paved the road for my later success. In particular, I would like to thank Mr. Hammer and Mr. Wilkerson for preparing me well in chemistry and physics. Their dedication to teaching was phenomenal. I would like to thank Mr. Tony Velie for transforming me from a ESL to a more mature English student. His dedication to us (our high school class) was truly heartfelt. Last but not least, I would like to thank Miss A.

Jean Eldredge for her constant effort to look for opportunities for me to shine. She encouraged me to attend Caltech when I knew only a little about colleges. I am deeply indebted to her.

Many thanks to Mom and Dad for getting us (me and my siblings) out of Vietnam for a chance of a better life. Their teaching has had great influence on me, particularly on the importance of hard work and honesty.

I would like to thank my siblings (Judy, Nancy, Anthony, and Eric) for always supporting me financially and emotionally. Being the youngest in the family, I suppose I am always their baby.

I would like to thank Aeran for always being there for me. She is one of the most patient and confident people I know. A part of me is always hers.

Contents

List of Figures

List of Tables

Chapter 1

Introduction

Magnetism was known to the Chinese over 4000 years ago, and yet today it is still an active area of research in the scientific community. Like many other fields in science, its popularity rises and falls, waiting at times for the stage to be set, to reveal the many facets of its force, which is deeply rooted in the richness of quantum mechanics and relativity.

The past decade has been an exciting time for magnetics. The stage is set for the exploration and exploitation of magnetic properties in thin metallic films and multilayers. The discovery of perpendicular magnetic anisotropy in thin-film structures can lead to new applications in high-density data-storage media and devices, particularly in the area of magneto-optical recording [Johnson *et. al.*, 1996]. The discovery of giant magnetoresistance (GMR) in Fe/Cr multilayers [Baibich *et. al.*, 1988] has led to the announcement of the first commercial GMR heads for high performance desktop products by IBM in December 1997 [Belleson and Grochowski, 1999]. A new class of microelectronic devices — spin polarized devices made entirely of metal films, whose operations depend on the spin orientation of the conduction electrons — promises smaller and faster devices than the ones fabricated

with semiconductor materials [Johnson, 1994; Prinz, 1998]. We stand today on the verge of a magnetoelectronics revolution, in which new phenomena in thin metal films, combining magnetism with traditional electronic elements, will not only be explained but also exploited in devices [Prinz, 1995].

To be fair, the richness of thin structured magnetic layers was well anticipated by researchers in the late 1950s, but their pursuit could not be readily accomplished because the strict demand for quality films and surface-sensitive techniques could not be met. The pursuit was possible in the past decade due to the availability of ultra high vacuum technology and advances in surfaces science [Heinrich *et. al.*, 1989; Bland and Heinrich, 1994].

Although the journey into magnetic thin-film science has been fruitful, the road to its deeper understanding remains largely untravelled. There are still many fundamental issues that need to be addressed, among these is the the effect of film stress on magnetism.

It is often the case that large stresses are present in thin films [Ohring, 1992, p. 403]. These film stresses are typically in the range of 10^8 to 10^{10} dynes/cm^2, which is comparable to the yield strength of most bulk metals. Further, the stress state is highly dependent on the process parameters. To illustrate this, figure 1.1 shows a plot of stresses as a function of argon gas pressure for Cr, Mo, Ta, and Pt magnetron-sputtered films on glass substrates. It is found that the stress states of these films depend strongly on the argon pressure. For example, an increase in the argon gas pressure from 6 mT to 10 mT can change the stress in the Ta films from -1 GPa to 1 GPa (1 GPa = 10^{10} dynes/cm^2). This change in the stress is significant. Any physical quantities that couple with the stress must also depend on the same process parameters. The only question is, by how much are they affected?

The coupling between mechanical deformation and magnetic properties (namely,

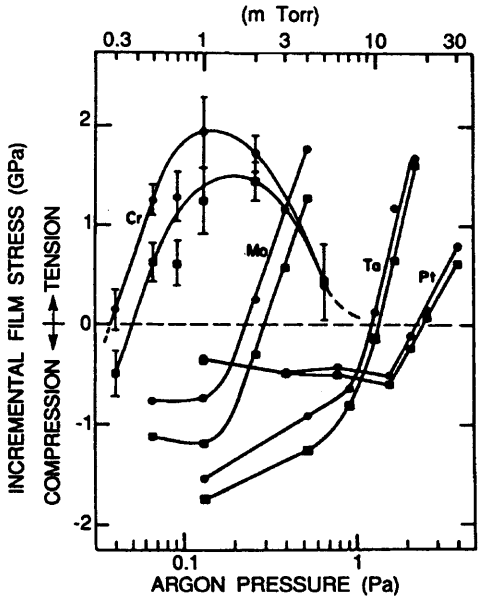

Figure 1.1: Biaxial internal stresses as a function of argon pressure for Cr, Mo, Ta, and Pt magnetron-sputtered films on glass substrates [Hoffman, 1982].

the magnetoelastic coupling) has been known for more than a century. It was discovered by Joule in 1842 when he demonstrated that an iron sphere deforms to an ellipsoid when it is magnetized in an external magnetic field. This type of magnetic-induced deformation is called magnetostrictive strain, or magnetostriction, to distinguish it from mechanical strain. It is a weak effect. The saturation magnetostriction λ_s (the strain when the material goes from a total demagnetized state to a fully saturated state) of a typical transition metal or alloy is in the order of 10^{-5}. Two orders of magnitude greater magnetostriction are observed in some rare earth metals and their alloys (e.g., Terfenol-D, $\lambda_s \approx 10^{-3}$).

However, the inverse magnetostriction effect (the change in the magnetic properties due to an applied external load) can be significant. For example, figure 1.2

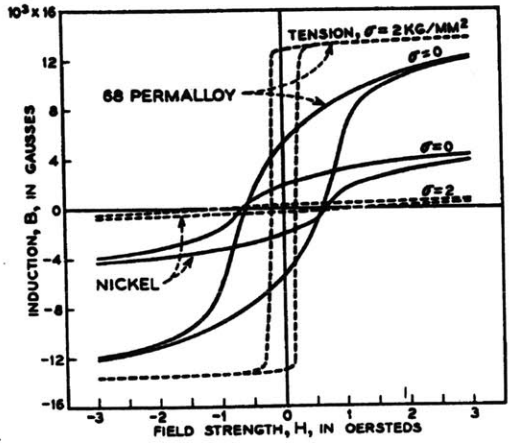

Figure 1.2: Effect of stress on the hysteresis loops of nickel and 68 Permalloy [Bozorth, 1951, p. 597].

plots the hysteresis loops of bulk nickel and 68 Permalloy (NiFe with 68% nickel) with and without applied load (the field is applied parallel to the tensile direction). The graph shows an applied unidirectional tensile stress of 2 kg/mm^2 (which is about 20 MPa, corresponding roughly to a strain of 0.01%) can *decrease* the permeability of the nickel by about ten times and *increase* the permeability of the 68 Permalloy twenty times [Bozorth, 1951, p. 595].[1]

Thus, since the internal stress in a thin film is usually large, the inverse magnetostrictive effect can play a dominant role in determining its easy direction of magnetization and the corresponding technical properties. The effect is most dramatically displayed in some systems that exhibit perpendicular magnetization (that is, the easy axis points out of the plane of the films): Au/Co/Au trilayer [Chappert and Bruno, 1988]; $\{Co/Au\}_n$ and $\{Co/Cu\}_n$ superlattices [Lee *et. al.*, 1990]; Cu/Ni/Cu(001)

[1]Bulk nickel is an example of a negative magnetostrictive material; its magnetization tends to rotate away the tensile stress direction. Bulk 68 Permalloy is a positive magnetostrictive material; its magnetization tends to follow the tensile stress direction.

trilayer [Chang, 1990b; Jungblut *et. al.*, 1994; Bochi *et. al.*, 1996]; Cu/Ni/Cu(111) trilayer [Gradmann, 1966 and 1993; Jungblut *et. al.*, 1994]; just to name a few. The transition from in-plane to out-of-plane magnetization is sometimes explained in light of the inverse magnetostrictive effect (due to the large internal stress in the film) and interfacial phenomenon. Since the magnetic anisotropy — the preference of the magnetization to point in certain crystallographic directions — is one of the most important properties of a magnetic material, a good understanding of the magnetoelastic coupling in thin films is essential if thin-film structures are to be used intelligently for technological applications [Falicov *et. al.*, 1990].

1.1 Literature Review

In the past decade, several experiments have unambiguously demonstrated that the magnetoelastic (ME) interactions in thin films can be significantly different from those in their bulk forms. The first such evidence was reported by Zuberek *et. al.* [1988]. They found that the saturation magnetostriction coefficient of $\{Ni/Ag\}_n$ multilayer varied inversely with the nickel film thickness by strain-modulated ferromagnetic resonance (SMFMR). The observed effect was attributed to the reduced local symmetry in the interfaces.

Sun and O'Handley [1991] reported the first direct measurement of the surface magnetoelastic coefficient (B^s) of a cobalt-rich ($Co_{76}Cr_4B_{20}$) and an iron-rich ($Fe_{77}Cr_6B_{17}$) amorphous alloy. By studying the spin polarization of the secondary electrons emitted from the surfaces as a function of imposed strain, they found B^s was about three times the bulk ME coefficient for the cobalt-rich alloy, and about half the bulk value for the iron-rich alloys. The observed deviations were attributed to a second-order ME effect due to the large strains at the surfaces [O'Handley and

Sun, 1992].

Song *et. al.* [1994] measured the effective ME coupling coefficients of polycrystalline NiFe/Ag/Si, NiFe/Cu/Si, and Ni/SiO_2/Si thin films by magneto-optic Kerr effect (MOKE). By straining the films and measuring the corresponding changes in the magnetization loops, they found that the effective ME coefficients diverged significantly from their bulk values for all the films that were less than 100Å. For the slightly Fe-rich permalloy films, the coefficient could even change sign. Song *et. al.* also attributed the deviations to the broken symmetry at the interfaces.

Magnetostriction was measured by Weber *et. al.* [1994] in polycrystalline iron films using a cantilever beam bending technique. Considerable deviations from the bulk iron value for film thicknesses below 100Å were also noted. For film thicknesses below 30Å film, the saturation magnetostriction changed sign. No explanations were offered for the anomaly.

Recently, Koch *et. al.* [1996] reported a direct measurement of one of the ME coefficients (B_1^{eff}) in epitaxial Fe(001) films using a cantilever beam bending technique. Since these were 1000Å films, interfacial effects could be safely neglected. But they found B_1^{eff} also varied linearly with the intrinsic stress of the samples, which was varied by changing the growth temperature of the films. For stresses greater than 0.8 GPa (which corresponds roughly to a strain of 0.3%), B_1^{eff} changed sign. The authors attributed their observation to a second-order ME effect. The second-order coupling coefficient (D_{11}) was estimated to be 1.1 GJ/m^3 (1.1 $\times$ 10^{10} ergs/cm^3).

The finding by Koch *et. al.* [1996] seems to cast doubt on some of the earlier interpretations on the observed anomalies in the ME coefficients of thin films and multilayers, particularly those by Zuberek *et. al.* [1988] and Song *et. al.* [1994]. Instead of explaining the deviations in light of broken symmetry in interfaces, the anomalies could be explained in light of second-order ME effects. There was no further

evidence to rule out one interpretation from the other in these early experiments.

Very recently, Sander *et. al.* [1998] also measured a ME coupling coefficient in epitaxial Fe/W(001) films. Using the cantilever bending method, the ME coefficient was found to depend on the film thickness. For iron layers below 30Å in thickness, the coefficient also changed sign. The authors attributed their observation to the surface ME coupling in interfaces as first suggested by Sun and O'Handley [1991].

In short, it seems clear that the ME coefficients in thin films and multilayers can deviate significantly from their respective bulk values. But what is still unclear is the cause the deviations: Is it a consequence of the large stresses in thin films that change the apparent first-order coefficients by the introduction of non-linear order terms or is it a true interfacial effect?

1.2 Motivation for the Research

The epitaxial Cu/Ni/Cu(001) system has been a good candidate for the investigation of magnetic anisotropy in thin films and multilayers. The magnetization of the nickel layer points out of the plane of the film over a wide range of the nickel film thickness (20Å $\leq t_{Ni} \leq$ 120Å) [Jungblut *et. al.*, 1994; Bochi *et. al.*, 1996]. This is unusual for thin films because of the shape magnetic anisotropy (the magnetostatic energy) that strongly favors in-plane magnetization.[2] To give a perspective, the magnetization of Fe(001)/Ag(001) bilayer points out of the plane of the film for only the first few monolayers of the iron atoms [Stampanoni *et. al.*, 1987]. $\{Co/Pd(001)\}_n$ and $\{Co/Pd(111)\}_n$ multilayers exhibit out-of-plane easy-axis anisotropy only if each of the cobalt layers is less than 3Å and 24Å thick, respectively [Engel *et. al.*, 1991]. For

[2]Perpendicular magnetization results in magnetic poles at the surfaces of the film. This is a high energy state in comparison to an in-plane magnetization state. We will discuss this shape anisotropy in more detail later.

some systems, no perpendicular magnetic anisotropy is observed for all film thicknesses (e.g., $\{Co/Cu\}_n$ and $\{Co/Ag\}_n$ multilayers, [den Broeder *et. al.*, 1991]).[3]

One key factor that is responsible for the perpendicular magnetization in the Cu/Ni/Cu(001) films is the inverse magnetostriction in the nickel layer [Chang, 1990b; Jungblut *et. al.*, 1994; Bochi *et. al.*, 1996]. Nickel atoms, upon deposited on copper buffer layer, are under biaxial tension due to the lattice mismatch between bulk nickel and copper (2.6%). Since bulk nickel is a negative magnetostrictive material, the in-plane biaxial strain would tend to drive the magnetization out of the film plane; for some film thicknesses, the magnetostrictive force is strong enough to even overcome the shape magnetic anisotropy. Thus, the wide window of perpendicular magnetization also makes the Cu/Ni/Cu(001) films a model system for the study of the inverse magnetostriction effect in thin films and multilayers.

The peculiar feature about the magnetic anisotropy of the Cu/Ni/Cu(001) system is that there is a tendency for the magnetization to go back to the film plane as the thickness of the nickel layer decreases. [4] For the thicker films, it is clear that the magnetization wants to be in-plane due to the magnetostatic energy, which is proportional to the thickness of the film. But what is the driving force that undermines the preference for out-of-plane magnetization as the nickel layer becomes thinner?

Two major models — one by Jungblut *et. al.* [1994], the other by Bochi *et. al.* [1996] — have been proposed to explain this thickness dependence of the magnetic anisotropy. In the Jungblut model, the tendency for the re-entry of the in-plane magnetization for the thinner nickel films is explained in term of the Néel interface

[3]For a more complete list of system that show perpendicular magnetization, please consult the review article by Johnson *et. al.* [1996].

[4]Although no transition from out-of-plane to in-plane easy magnetic axis with decreasing film thickness has been reported in the Cu/Ni/Cu(001) system in the literature, such a transition is observed in the uncapped Ni/Cu(001) system. The critical thickness was reported to be about 7 monolayer of nickel [Huang *et. al.*, 1994; Schulz and Baberschke, 1994].

term — the strain-*independent* part of the magnetic anisotropy of the interfacial atoms. The idea is that as the thickness of the nickel layer decreases, the effective interfacial contribution to the total anisotropy energy density increases. Since the nickel magnetization tends to go back in-plane with the decrease in the film thickness, the model suggests that the Néel interface term must favor in-plane magnetization.

In the Bochi model, the tendency for the reorientation is thought to come from the interface ME term — the strain-*dependent* part of the magnetic anisotropy of the interfacial atoms. By including this interfacial term in the total magnetic anisotropy which was then used to fit the experimental data, the authors concluded that the Néel interface term must favor out-of-plane magnetization, contrary to what is suggested by the Jungblut model.

Thus, two models have been proposed to explain the magnetic anisotropy of the Cu/Ni/Cu(001) system. One says that it is the Néel interface term that is responsible for the tendency for the magnetization to go back in the film plane for small thicknesses. The other model says that the Néel interface term favors out-of-plane magnetization; what drives the magnetization back in-plane for the thinner nickel films is the interface ME anisotropy. Clearly, only one can be right, but both can be wrong.

Indeed, it is this controversy that prompted the work for this thesis. The idea is that if we can directly measure some of the ME coefficients of the Cu/Ni/Cu/Si(001) films, we can test the validity of the Jungblut and Bochi models. Further, the direct measurement of the ME coefficients is an interesting pursuit in itself: Are these coefficients different from the respective bulk values (B_1 and B_2)? Do some of them even change sign, as in the case of the iron films [Koch *et. al.*, 1996; Sander *et. al.*, 1998]? These are important questions if the magnetic anisotropy in the Cu/Ni/Cu(001) films are to be properly understood and controlled.

1.3 Approach and Organization of the Thesis

There are many methods by which the ME coefficients can be measured, but they generally fall into two categories: i) A direct approach is one in which a ME coupling coefficient is found by either applying a stress and then studying the corresponding change in a magnetic property (usually the anisotropy energy) [Sun and O'Handley, 1991; O'Handley *et. al.*, 1993; Baril *et. al.*, 1998], or by applying a magnetic field and then measuring the corresponding magnetostrictive stresses or strains [Klokholm, 1976; Koch *et. al.*, 1996; Sander *et. al.*, 1998]. ii) An indirect approach is one in which no direct force or magnetic field is applied. Instead, a ME coefficient is estimated by fitting a particular functional form to some experimental data (usually the magnetic anisotropy data) [Bochi *et. al.*, 1994; Bochi *et. al.*, 1996].

In this thesis work, the ME coefficients of a series of Cu/Ni/Cu/Si(001) films — prepared by molecular beam epitaxy (MBE) technique — are determined both indirectly and directly. The indirect method similar to that by Bochi *et. al.*. is used to estimate all the coupling coefficients. The energy expression used to fit the anisotropy data is different from that used in the Bochi model in two important ways: i) both the linear and second- order ME terms are included in the analysis (the expression used by Bochi *et. al.* includes only the linear terms); ii) the spin-pair model is used to reduce the number of fitting parameters from seventeen to only two. A cantilever beam method is also used to measure an effective magnetoelastic coefficient (B_{11}^{eff}) directly.

The presentation of the thesis is organized as follows. The intrinsic magnetic anisotropy for a thin fcc(001) film is described using the spin-pair model (chapter 2). The purpose is to lay the foundation for the later analysis of the magnetic anisotropy data. Chapter 3 describes the epitaxy of the Cu/Ni/Cu/Si(001) system. The relevant

literature is reviewed. Chapter 4 describes the sample preparation and structural characterizations of the nickel films. Since the strains in the nickel films are important for the study of inverse magnetostriction, the result of a synchrotron x-ray study (both Bragg and grazing-incidence diffraction) is presented in some detail. Chapter 5 reports the result of the magnetic characterizations of the nickel films using vibrating sample magnetometer (VSM) and torque magnetometer. The application of the spin-pair model in analyzing the anisotropy data is presented in chapter 6. Here, the values of all the ME coefficients of the nickel layer are tabulated. Chapter 7 discusses the cantilever beam method and measurement of an effective magnetoelastic coefficient (B_{11}^{eff}). The result is compared with that obtained by the SP approach in chapter 6. Chapter 8 gives a brief discussion on some of the main findings of this thesis. Chapter 9 provides some suggested future work.

Chapter 2

Film Intrinsic Magnetic Anisotropy

There is an inherent tendency for the magnetization of a ferromagnet to lie in certain crystallographic directions which are called the intrinsic easy axes of magnetization. That is to say, the ease to magnetize the material depends on the direction of the applied field with respect to the crystal axes, even when no extrinsic origins of anisotropy such as the shape effect are present. For bulk body-centered cubic (bcc) iron, the intrinsic easy axes of magnetization are the <100> directions; for bulk face-centered cubic (fcc) nickel, they are the <111>; for bulk hexagonal close-packed (hcp) cobalt, the *c*-axis is the direction of easy magnetization [Cullity, 1972, p. 207; Chikazumi, 1997, p. 249].

The intrinsic magnetic anisotropy (IMA) of thin films and multilayers can be different from that of bulk in a fundamental way. Interface atoms experience an environment that is different from those in the interior due to the broken symmetry at the interfaces.[1] For a bulk crystal, the ratio of the number of atoms at the interfaces and those in the interior is very small; hence, the interface effect can be neglected. But for thin films, this ratio may be large; then, the presence of interface atoms must

[1]Interface is defined here to include the surface between the material and vacuum. The reason for this usage is economy. The general physics that is applied to say copper/nickel interface can also apply to the surface of nickel with vacuum.

be considered. In the extreme case of a monolayer or bilayer film, all the atoms are in fact "interface" atoms.

Two general approaches have been used to investigate the IMA of thin films and multilayers. One is by doing first-principles calculations from which information about the IMA can be obtained [Bennett and Cooper, 1971; Takayama *et. al.*, 1976; Gay and Ritchter, 1986; Victora and MacLaren, 1993; Wu *et. al.*, 1998; Uiberacker *et. al.*, 1999]. The other is to simply describe it phenomenologically [Bruno, 1988; O'Handley *et. al.*, 1993; Victora and MacLaren, 1993; Chuang *et. al.*, 1994 Lacheisserie, 1995]. Although the former has much theoretical appeal, it is computationally intensive, and so far lacks the accuracy needed to put much confidence in the results.[2] The latter approach, on the other hand, involves much less computation. In fact, the goal of a phenomenological theory is not to compute the interaction terms; rather, it is used to define them consistently with the symmetry of the system. Experiments can then be designed to measured the coefficients as defined by the phenomenological theory.

In this thesis, the spin-pair (SP) model is used to write the magnetic anisotropy phenomenologically. The model is extended to include second-order ME terms in order to describe the IMA of highly strained systems. Specific application is made for the tetragonally distorted nickel fcc(001) films in the Cu/Ni/Cu/Si(001) system. The advantages and disadvantages of the method will be discussed after the model is developed in this chapter.

[2]First-principles determination of the magnetic anisotropy (particularly the magnetoelastic coupling coefficients) in thin films and multilayers still remains a great challenge for modern electronic structure theory. The difficulty lies in poor numerical stability and the large number of sampling k-points needed for any sensible predictions [Wu *et. al.*, 1998].

2.1 The Spin-Pair (SP) Model

Néel is the first to apply to the SP model to study the interface anisotropy of a ferromagnet [Néel, 1954]. The model is based on the following assumptions:

i. There is a coupling between the magnetization and elastic strains in a ferromagnet;

ii. The total intrinsic magnetic energy of the ferromagnet is the sum of all the pair potentials in the solid;

iii. The pair potential between atom i and j depends only on the distance r between them and the angle ψ between the spins and the bond axis connecting them (see figure 2.1); that is,

$$E_{ij} = E_{ij}(r, \psi). \tag{2.1}$$

Note that Eq. 2.1 assumes the magnetic moments of the atoms are aligned in the same direction; otherwise, $E_{ij} = E_{ij}(r, \psi_i, \psi_j)$ where ψ_i and ψ_j are the angles between the spins of atom i and j with the bond axis, respectively. For a ferromagnet, the assumption that $\psi_i = \psi_j$ is good; the reason is that the spins of nearest neighboring atoms are usually strongly coupled by the Heisenberg exchange interaction.

It is common to expand the pair potential E_{ij} in terms of the even Legendre polynomials as follows [Chuang *et. al.*, 1994; Chikazumi, 1997, p. 267]:

$$E_{ij}(r, \phi) = G(r) + L(r)\left(cos^2(\psi) - \frac{1}{3}\right) + Q(r)\left(cos^4(\psi) - \frac{6}{7}cos^2(\psi) + \frac{3}{35}\right) + \ldots \tag{2.2}$$

Note that the first term $G(r)$ does not depend on ψ and thus gives no contribution to the magnetic anisotropy of the system. The second is the pseudodipolar term; it

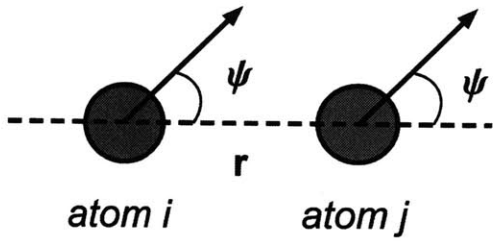

Figure 2.1: Coordinates used to describe the pair potential: r is the distance that separates the two atoms; ψ is the angle between the spin and the bond axis connecting the two atoms.

describes uniaxial anisotropy. The third is the quadrupolar term; it describes cubic anisotropy.

The r dependence is contained in the coefficients of the Legendre polynomial expansion (Eq. 2.2). Each coefficient is expanded in a Taylor series about the bulk bond length r_0 [Chuang *et. al.*, 1994; Chikazumi, 1997, p.349]. For example,

$$L(r) = L(r_0) + \frac{dL(r_0)}{dr} r_0\epsilon + \frac{1}{2}\frac{d^2L(r_0)}{dr^2} r_0^2\epsilon^2 + ... \tag{2.3}$$

where $\epsilon = (r - r_0)/r_0$ is the strain in the bond length from its bulk value. Note that the expansion in the bond distance r is a way to account for the interaction between strains and magnetism in the SP model. If the strain is small ($< 10^{-4}$), only the linear term in the Taylor expansion (Eq. 2.3) is needed [Chuang *et. al.*, 1994; Chikazumi, 1997, p. 349]. In this thesis, the second-order term will be included to account for the large misfit and residual strains in the Cu/Ni/Cu/Si(001) films.

Since the $G(r)$ term in the Legendre polynomial expansion (Eq. 2.2) does not contribute to the magnetic anisotropy, it will be ignored in the discussion. Then, the sum of all pair potentials is just the intrinsic magnetic anisotropy energy (IMAE) of the system because each term in the sum depends on the direction of the magnetization.

2.2 Categories of Energy

Since there are many energy terms as a result of the summing of pair potentials, it is useful to group them into categories. One convenient way is to partition the IMAE into magnetocrystalline (MC) and magnetoelastic (ME) energy. MC energy describes the anisotropy energy of a fixed reference structure. [3] The energy terms in this category depend only on the direction of the magnetization. ME energy describes the energy needed to distort the system from the reference structure. The energy terms in this category depend on both the direction of the magnetization and the strain associated with the deformation.

Another useful partition of the IMAE is based on the bulk/interface distinction. This distinction is important because interface atoms can exhibit anisotropy that is different from that in the bulk due to the broken symmetry at the interfaces, as discussed before. In the framework of the pair potential, the difference is viewed in terms of the number of bonds to be summed. For interface atoms, the number of neighboring bonds is less than or different from that experienced by bulk atoms (ones that are inside the material). One way of accounting for this difference is first to assume all atoms in the systems are fully coordinated as those in the interior of the material. The missing or different bond energy of the interface atoms is then subtracted from the sum to give the IMAE of the system [Chuang *et. al.*, 1994]. With this accounting scheme, the IMAE density of a film takes the following form (To see the derivation, consult Appendix A or the paper by Chuang *et. al.*, [1994]):

$$E_{film} = E_{bulk} - \frac{2E_{interface}}{t} \tag{2.4}$$

[3] The bulk structure is usually the reference structure used to describe the MC energy of the system. For example, the MC energy of a nickel film is usually taken to be the IMAE of bulk nickel. For further discussion, consult Appendix B.

where E_{bulk} is the bulk anisotropy energy density of the crystal, $E_{interface}$ is the broken bond energy per unit interface area of the crystal, and t is the thickness of the film. The factor 2 reflects the assumption that the film has two identical interfaces. With the interface/bulk and MC/ME energy distinctions, the IMAE density can then be written as follows:

$$E_{film} = (E_{bmc} + E_{mbe}) - 2\left(\frac{E_{imc}}{t} + \frac{E_{ime}}{t}\right) \tag{2.5}$$

where E_{bmc} is the bulk MC energy, E_{bme} the bulk ME energy, E_{imc} the interface MC energy, and E_{ime} the interface ME energy.

Another useful partition of the ME energy is based on the order of the strain: ϵ, ϵ^2, and so forth. This partition of the energy provides a quantitative assessment of the contribution of each ME term to the IMAE. Figure 1 summarizes schematically all the categories of energy that will be useful for later discussion. The SP model is expected to give some guidance on the relative importance of these different types of terms.

2.3 Uniaxial Magnetic Anisotropy of fcc(001) Films

The SP model is now used to write the IMAE of a fcc(001) film under a biaxial strain which is described by the following strain tensor:

$$(e_{ij}) = e_0 \begin{pmatrix} 1 & 0 & 0 \\ 0 & 1 & 0 \\ 0 & 0 & -\frac{2c_{12}}{c_{11}} \end{pmatrix} \tag{2.6}$$

where e_0 is the magnitude of the in-plane film strain, and c_{11} and c_{12} are the elastic constants of the crystal. There are also magnetostrictive strains associated with the

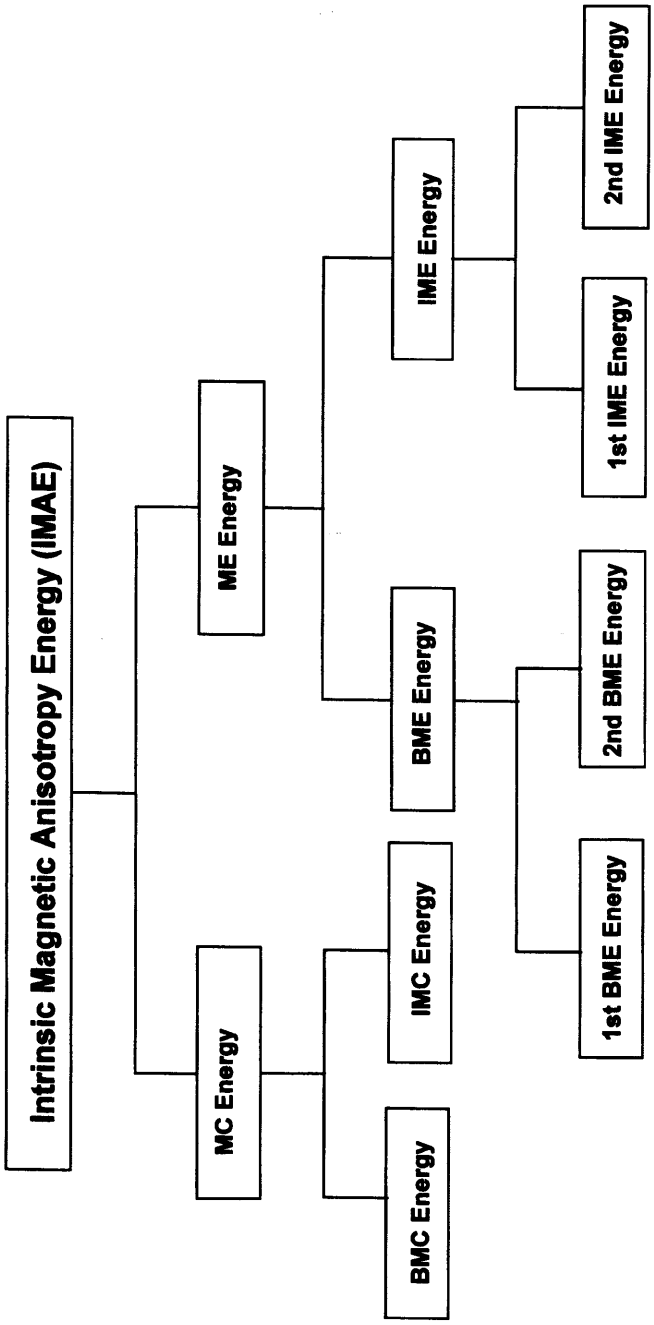

Figure 2.2: Categories of magnetic intrinsic anisotropy energy (IMAE).

direction of magnetization. Thus, the total deformation is

$$(t_{ij}) = \begin{pmatrix} e_0 + \epsilon_{11} & \epsilon_{12} & \epsilon_{13} \\ \epsilon_{21} & e_0 + \epsilon_{22} & \epsilon_{23} \\ \epsilon_{31} & \epsilon_{32} & -\frac{2c_{12}}{c_{11}} e_0 + \epsilon_{33} \end{pmatrix} \tag{2.7}$$

where $t_{ij} = t_{ji}$. The challenge is to write the ME energy terms of the film for this strain tensor.

Certainly, the pair potential between atom i and j after the deformation still has the same form as that in Eq. 2.2:

$$E'_{ij}(r', \psi') = L(r') \left(cos^2(\psi') - \frac{1}{3} \right) + Q(r') \left(cos^4(\psi') - \frac{6}{7} cos^2(\psi') + \frac{3}{35} \right) + ... \tag{2.8}$$

where r' is the new bond length, and ϕ' is the new angle between the direction of the magnetic moments and the new bond direction (see figure 2.3). Because it is desirable to write the ME energy in reference to the undeformed bulk structure (see Appendix B for the discussion), E'_{ij} is rewritten in the undeformed coordinates (namely, r and ψ).

For example, suppose atom i and j are located at $(0, 0, 0)$ and $\frac{1}{\sqrt{2}}(1, 0, 1)$, respectively, before the deformation. Assume their magnetic moments point in the common direction $\hat{m} \equiv (\alpha_1, \alpha_2, \alpha_3)$. After the deformation, the dipole term of the Legendre expansion of E'_{ij} (Eq. 2.8) can be written as follows:

$$\begin{aligned} L(r') &= L(\frac{a_0}{\sqrt{2}}) + \frac{dL(\frac{a_0}{\sqrt{2}})}{dr} \frac{a_0}{\sqrt{2}} \frac{t_{11} + t_{33} + 2t_{13}}{2} \\ &+ \frac{1}{2} \frac{d^2 L(\frac{a_0}{\sqrt{2}})}{dr^2} \left(\frac{a_0}{\sqrt{2}} \right)^2 \left(\frac{t_{11} + t_{33} + 2t_{13}}{2} \right)^2 + ... \end{aligned} \tag{2.9}$$

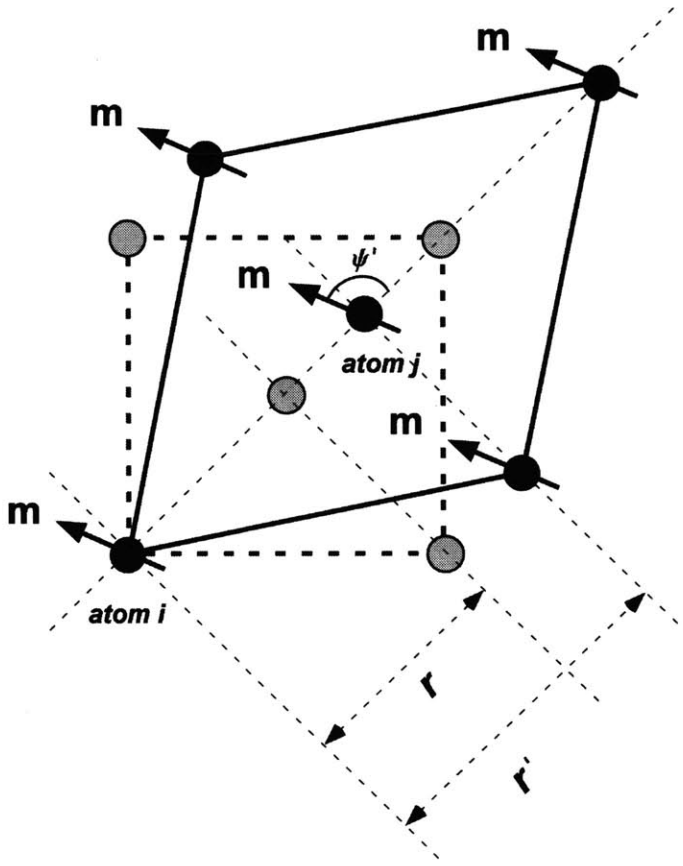

Figure 2.3: Positions of atoms before and after lattice deformation. The gray circles are the locations of atoms before the deformation; the dark circles are the positions of atoms after the deformation. $\mathbf{m}$ is the magnetic moment. r and r' are the bond lengths before and after the deformation, respectively. ψ is the angle between the magnetization and the new bond direction.

where a_0 is the lattice constant of the undeformed cubic, and (t_{ij}) is the total strain tensor of the film. For most 3d metallic films, the magnetostrictive strains are small; second-order magnetostrictive terms can be safely neglected — terms such as ϵ_{11}^2, and $\epsilon_{12}\epsilon_{13}$. Thus, Eq. 2.9 becomes

$$\begin{aligned} L(r') &= L(\frac{a_0}{\sqrt{2}}) + \frac{1}{2}\frac{dL(\frac{a_0}{\sqrt{2}})}{dr}\frac{a_0}{\sqrt{2}}\left(\epsilon_{11}+\epsilon_{33}+2\epsilon_{13}+(1-\frac{2c_{12}}{c_{11}})e_0\right) \\ &+ \frac{a_0^2}{8}\frac{d^2L(\frac{a_0}{\sqrt{2}})}{dr^2}(1-\frac{2c_{12}}{c_{11}})e_0\left(\epsilon_{11}+\epsilon_{33}+2\epsilon_{13}+\frac{1}{2}(1-\frac{2c_{12}}{c_{11}})e_0\right). \quad (2.10) \end{aligned}$$

The cosine of the angle between the new bond direction and the magnetization — i.e., $cos(\psi')$ — can be found by taking the dot product of the two unit vectors that point along these two directions. Without loss of generality, let $\hat{m} \equiv (\alpha_1, \alpha_2, \alpha_3)$ be the unit vector of the magnetization vector. The question is, where is the bond direction after the deformation?

In Appendix C, the transformation operator $\hat{\mathbf{T}}$ that maps the unit vector along the original bond direction to a new bond direction is found. For this particular pair, the old bond direction is the $\frac{1}{\sqrt{2}}[101]$; the new bond direction is

$$\begin{aligned} \hat{\mathbf{T}}\begin{pmatrix} \frac{1}{\sqrt{2}} \\ 0 \\ \frac{1}{\sqrt{2}} \end{pmatrix} &= \begin{pmatrix} 1+\epsilon_{11}+e_0 & \epsilon_{21} & \epsilon_{31} \\ \epsilon_{12} & 1+\epsilon_{22}+e_0 & \epsilon_{32} \\ \epsilon_{13} & \epsilon_{23} & 1+\epsilon_{33}-\frac{2C_{12}}{c_{11}}e_0 \end{pmatrix}\begin{pmatrix} \frac{1}{\sqrt{2}} \\ 0 \\ \frac{1}{\sqrt{2}} \end{pmatrix} \\ &= \frac{1}{\sqrt{2}}\begin{pmatrix} 1+\epsilon_{11}+\epsilon_{13}+e_0 \\ \epsilon_{12}+\epsilon_{23} \\ 1+\epsilon_{33}+\epsilon_{13}-\frac{2c_{12}}{c_{11}}e_0 \end{pmatrix}. \quad (2.11) \end{aligned}$$

By taking the dot product between $\hat{m}$ and the normal vector along the new bond direction, we get

$$cos(\psi') = \frac{(1+\epsilon_{11}+\epsilon_{13}+e_0, \epsilon_{12}+\epsilon_{23}, 1+\epsilon_{33}+\epsilon_{13}-\frac{2c_{12}}{c_{11}}e_0)}{\sqrt{(1+\epsilon_{11}+\epsilon_{13}+e_0)^2+(\epsilon_{12}+\epsilon_{23})^2+(1+\epsilon_{33}+\epsilon_{13}-\frac{2c_{12}}{c_{11}}e_0)^2}} \cdot \begin{pmatrix} \alpha_1 \\ \alpha_2 \\ \alpha_3 \end{pmatrix}. \tag{2.12}$$

The factor in the denominator is the normalization factor.

For simplicity, only the terms that are linear in the misfit and magnetostrictive strains are kept. The assumption is that second-order magnetostrictive effects come mostly from the second derivative of the coefficients of the Legendre expansion (Eq. 2.8). Thus,

$$\begin{aligned} 2cos^2(\psi') &= (\alpha_1+\alpha_3)^2+(\alpha_1^2-\alpha_3^2)(\epsilon_{11}-\epsilon_{33})+2(\alpha_1\alpha_3+\alpha_2\alpha_3)(\epsilon_{12}+\epsilon_{23}) \\ &+ (\alpha_1^2-\alpha_3^2)(1+\frac{2c_{12}}{c_{11}})e_0. \end{aligned} \tag{2.13}$$

Plugging Eqs. 2.13 and 2.10 into Eq. 2.8, and keeping all the linear terms, only the second-order terms in the misfit strains, and the terms that are the products of the misfit and magnetostrictive strains, we get that the pair interaction potential between atom i and j located at $(0,0,0)$ and $\frac{1}{\sqrt{2}}(1,0,1)$ is

$$\begin{aligned} E'_{ij} &= \left[L(\frac{a_0}{\sqrt{2}})+\frac{1}{2}\frac{dL(\frac{a_0}{\sqrt{2}})}{dr}\frac{a_0}{\sqrt{2}}\left(\epsilon_{11}+\epsilon_{33}+2\epsilon_{13}+(1-\frac{2c_{12}}{c_{11}})e_0\right)\right. \\ &\left.+\frac{a_0^2}{8}\frac{d^2L(\frac{a_0}{\sqrt{2}})}{dr^2}(1-\frac{2c_{12}}{c_{11}})e_0\left(\epsilon_{11}+\epsilon_{33}+2\epsilon_{13}+\frac{1}{2}(1-\frac{2c_{12}}{c_{11}})e_0\right)\right] \\ &\cdot \left[\frac{1}{2}\left((\alpha_1+\alpha_3)^2+(\alpha_1^2-\alpha_3^2)(\epsilon_{11}-\epsilon_{33})+2(\alpha_1\alpha_3+\alpha_2\alpha_3)(\epsilon_{12}+\epsilon_{23})\right.\right. \\ &\left.\left.+(\alpha_1^2-\alpha_3^2)(1+\frac{2c_{12}}{c_{11}})e_0\right)-\frac{1}{3}\right]. \end{aligned} \tag{2.14}$$

Expressions for the pair potentials of other neighbors can be found with the same procedure. The IMAE can then be obtained by summing all the pairs in the crystal. For simplicity, only first-nearest neighbor pairs are considered. Further, only an uniaxial theory is developed in this thesis; all the higher-order angular terms will be neglected. This choice is justifiable for the nickel film in Cu/Ni/Cu(001) system because the torque measurement (which will be presented later) shows that higher angular contribution to the magnetic anisotropy is negligible.

2.3.1 Bulk Magnetocrystalline Energy

Since the bulk reference state is used to describe the intrinsic magnetic anisotropy, the MC energy of the film is the same as that of the bulk, namely,

$$\begin{aligned} E_{bmc} &= \rho Q(\frac{a_o}{\sqrt{2}}) \left(\alpha_1^2\alpha_2^2 + \alpha_2^2\alpha_3^2 + \alpha_3^2\alpha_1^2\right) \\ &\equiv K_1 \left(\alpha_1^2\alpha_2^2 + \alpha_2^2\alpha_3^2 + \alpha_3^2\alpha_1^2\right) \end{aligned} \tag{2.15}$$

where ρ is the atomic density [Chikazumi, 1997, p. 269]. Because this energy term is quadrupolar, it is neglected in the uniaxial model.

2.3.2 Bulk Magnetoelastic (BME) Energy

The bulk magnetoelastic (BME) energy can be found by first adding all the nearest SP potentials and subtracting the MC energy from the sum. Thus, the ME energy of an atom in the interior of a fcc(001) film under a biaxial strain can be found by summing all the nearest neighbor interactions with the atom:

$$E_{bme}^{atom} = \left[L(\frac{a_0}{\sqrt{2}}) + \frac{1}{2}\frac{dL(\frac{a_0}{\sqrt{2}})}{dr}\frac{a_0}{\sqrt{2}}\left(\epsilon_{11} + \epsilon_{33} + 2\epsilon_{13} + (1 - \frac{2c_{12}}{c_{11}})e_0\right)\right.$$

$$
\begin{aligned}
&+\frac{a_0^2}{8}\frac{d^2L(\frac{a_0}{\sqrt{2}})}{dr^2}(1-\frac{2c_{12}}{c_{11}})e_0\left(\epsilon_{11}+\epsilon_{33}+2\epsilon_{13}+\frac{1}{2}(1-\frac{2c_{12}}{c_{11}})e_0\right)\Bigg]\\
\cdot\ &\left[\frac{1}{2}\left((\alpha_1+\alpha_3)^2+(\alpha_1^2-\alpha_3^2)(\epsilon_{11}-\epsilon_{33})+2(\alpha_1\alpha_2+\alpha_2\alpha_3)(\epsilon_{12}+\epsilon_{23})\right.\right.\\
&\left.\left.+(\alpha_1^2-\alpha_3^2)(1+\frac{2c_{12}}{c_{11}})e_0\right)-\frac{1}{3}\right]\\
+\ &\left[L(\frac{a_0}{\sqrt{2}})+\frac{1}{2}\frac{dL(\frac{a_0}{\sqrt{2}})}{dr}\frac{a_0}{\sqrt{2}}\left(\epsilon_{11}+\epsilon_{33}-2\epsilon_{13}+(1-\frac{2c_{12}}{c_{11}})e_0\right)\right.\\
&\left.+\frac{a_0^2}{8}\frac{d^2L(\frac{a_0}{\sqrt{2}})}{dr^2}(1-\frac{2c_{12}}{c_{11}})e_0\left(\epsilon_{11}+\epsilon_{33}-2\epsilon_{13}+\frac{1}{2}(1-\frac{2c_{12}}{c_{11}})e_0\right)\right]\\
\cdot\ &\left[\frac{1}{2}\left((\alpha_1-\alpha_3)^2+(\alpha_1^2-\alpha_3^2)(\epsilon_{11}-\epsilon_{33})+2(\alpha_1\alpha_2-\alpha_2\alpha_3)(\epsilon_{12}-\epsilon_{23})\right.\right.\\
&\left.\left.+(\alpha_1^2-\alpha_3^2)(1+\frac{2c_{12}}{c_{11}})e_0\right)-\frac{1}{3}\right]\\
+\ &\left[L(\frac{a_0}{\sqrt{2}})+\frac{1}{2}\frac{dL(\frac{a_0}{\sqrt{2}})}{dr}\frac{a_0}{\sqrt{2}}\left(\epsilon_{22}+\epsilon_{33}+2\epsilon_{23}+(1-\frac{2c_{12}}{c_{11}})e_0\right)\right.\\
&\left.+\frac{a_0^2}{8}\frac{d^2L(\frac{a_0}{\sqrt{2}})}{dr^2}(1-\frac{2c_{12}}{c_{11}})e_0\left(\epsilon_{22}+\epsilon_{33}+2\epsilon_{23}+\frac{1}{2}(1-\frac{2c_{12}}{c_{11}})e_0\right)\right]\\
\cdot\ &\left[\frac{1}{2}\left((\alpha_2+\alpha_3)^2+(\alpha_2^2-\alpha_3^2)(\epsilon_{22}-\epsilon_{33})+2(\alpha_1\alpha_2+\alpha_1\alpha_3)(\epsilon_{12}+\epsilon_{13})\right.\right.\\
&\left.\left.+(\alpha_2^2-\alpha_3^2)(1+\frac{2c_{12}}{c_{11}})e_0\right)-\frac{1}{3}\right] \qquad (2.16)\\
+\ &\left[L(\frac{a_0}{\sqrt{2}})+\frac{1}{2}\frac{dL(\frac{a_0}{\sqrt{2}})}{dr}\frac{a_0}{\sqrt{2}}\left(\epsilon_{22}+\epsilon_{33}-2\epsilon_{23}+(1-\frac{2c_{12}}{c_{11}})e_0\right)\right.\\
&\left.+\frac{a_0^2}{8}\frac{d^2L(\frac{a_0}{\sqrt{2}})}{dr^2}(1-\frac{2c_{12}}{c_{11}})e_0\left(\epsilon_{22}+\epsilon_{33}-2\epsilon_{23}+\frac{1}{2}(1-\frac{2c_{12}}{c_{11}})e_0\right)\right]\\
\cdot\ &\left[\frac{1}{2}\left((\alpha_2-\alpha_3)^2+(\alpha_2^2-\alpha_3^2)(\epsilon_{22}-\epsilon_{33})+2(\alpha_1\alpha_2-\alpha_1\alpha_3)(\epsilon_{12}-\epsilon_{13})\right.\right.\\
&\left.\left.+(\alpha_2^2-\alpha_3^2)(1+\frac{2c_{12}}{c_{11}})e_0\right)-\frac{1}{3}\right]
\end{aligned}
$$

$$
\begin{aligned}
&+ \left[L(\frac{a_0}{\sqrt{2}}) + \frac{1}{2}\frac{dL(\frac{a_0}{\sqrt{2}})}{dr}\frac{a_0}{\sqrt{2}}\left(\epsilon_{11}+\epsilon_{22}+2\epsilon_{12}+2e_0\right)\right. \\
&\quad \left. + \frac{a_0^2}{4}\frac{d^2L(\frac{a_0}{\sqrt{2}})}{dr^2}e_0\left(\epsilon_{11}+\epsilon_{22}+2\epsilon_{12}+e_0\right)\right] \\
&\cdot \left[\frac{1}{2}\left((\alpha_1+\alpha_2)^2+(\alpha_1^2-\alpha_2^2)(\epsilon_{11}-\epsilon_{22})+2(\alpha_1\alpha_3+\alpha_2\alpha_3)(\epsilon_{13}+\epsilon_{23})\right)-\frac{1}{3}\right] \\
&+ \left[L(\frac{a_0}{\sqrt{2}}) + \frac{1}{2}\frac{dL(\frac{a_0}{\sqrt{2}})}{dr}\frac{a_0}{\sqrt{2}}\left(\epsilon_{11}+\epsilon_{22}-2\epsilon_{12}+2e_0\right)\right. \\
&\quad \left. + \frac{a_0^2}{4}\frac{d^2L(\frac{a_0}{\sqrt{2}})}{dr^2}e_0\left(\epsilon_{11}+\epsilon_{22}-2\epsilon_{12}+e_0\right)\right] \\
&\cdot \left[\frac{1}{2}\left((\alpha_1-\alpha_3)^2+(\alpha_1^2-\alpha_2^2)(\epsilon_{11}-\epsilon_{22})+2(\alpha_1\alpha_3-\alpha_2\alpha_3)(\epsilon_{13}-\epsilon_{23})\right)-\frac{1}{3}\right] \\
&- E_{bmc}^{atom}.
\end{aligned}
$$

After a considerable amount of algebraic manipulation, the ME energy density of the film can be expressed in a form which can be recognized as a tetragonal generalization of the cubic magnetoelastic energy:

$$
\begin{aligned}
E_{bme} &= D_{11}^b\left(\epsilon_{11}(\alpha_1^2-\frac{1}{3})+\epsilon_{22}(\alpha_2^2-\frac{1}{3})\right)+D_{12}^b\left(\epsilon_{33}(\alpha_3^2-\frac{1}{3})\right) \\
&+ D_{13}^b\left(\epsilon_{11}(\alpha_2^2-\frac{1}{3})+\epsilon_{22}(\alpha_1^2-\frac{1}{3})\right)+D_{21}^b\left(\epsilon_{12}\alpha_1\alpha_2\right) \\
&+ D_{22}^b\left(\epsilon_{13}\alpha_1\alpha_3+\epsilon_{23}\alpha_2\alpha_3\right)+D_{rs}^b\left(e_0(\alpha_3^2-\frac{1}{3})\right) \qquad (2.17)
\end{aligned}
$$

where

$$
\begin{aligned}
D_{11}^b &= \rho\left(3L(\frac{a_0}{\sqrt{2}})+\frac{1}{2}\frac{dL(\frac{a_0}{\sqrt{2}})}{dr}\frac{a_0}{\sqrt{2}}\right)+\frac{\rho}{4}\frac{d^2L(\frac{a_0}{\sqrt{2}})}{dr^2}a_0^2e_0 \\
&\equiv B_1+A_{11}^be_0, \\
D_{12}^b &= \rho\left(3L(\frac{a_0}{\sqrt{2}})+\frac{1}{2}\frac{dL(\frac{a_0}{\sqrt{2}})}{dr}\frac{a_0}{\sqrt{2}}\right)+\frac{\rho}{8}\frac{d^2L(\frac{a_0}{\sqrt{2}})}{dr^2}a_0^2(1-\frac{2c_{12}}{c_{11}})e_0 \\
&\equiv B_1+A_{12}^be_0,
\end{aligned}
$$

$$
\begin{aligned}
D^b_{13} &= \frac{\rho}{8}\frac{d^2L(\frac{a_0}{\sqrt{2}})}{dr^2}a_0^2(1+\frac{2c_{12}}{c_{11}})e_0 \equiv A^b_{13}e_0, \\
D^b_{21} &= 2\rho\left(2L(\frac{a_0}{\sqrt{2}})+\frac{dL(\frac{a_0}{\sqrt{2}})}{dr}\frac{a_0}{\sqrt{2}}\right)+\rho\frac{d^2L(\frac{a_0}{\sqrt{2}})}{dr^2}a_0^2e_0 \equiv B_2+A^b_{21}e_0, \\
D^b_{22} &= 2\rho\left(2L(\frac{a_0}{\sqrt{2}})+\frac{dL(\frac{a_0}{\sqrt{2}})}{dr}\frac{a_0}{\sqrt{2}}\right)+\frac{\rho}{2}\frac{d^2L(\frac{a_0}{\sqrt{2}})}{dr^2}a_0^2(1-\frac{2c_{12}}{c_{11}})e_0 \\
&\equiv B_2+A^b_{22}e_0, \\
D^b_{rs} &= -\rho\left(3L(\frac{a_0}{\sqrt{2}})+\frac{1}{2}\frac{dL(\frac{a_0}{\sqrt{2}})}{dr}\frac{a_0}{\sqrt{2}}\right)\left(1+\frac{2c_{12}}{c_{11}}\right), \\
&- \frac{\rho}{16}\frac{d^2L(\frac{a_0}{\sqrt{2}})}{dr^2}a_0^2\left(3+2(\frac{2c_{12}}{c_{11}})-(\frac{2c_{12}}{c_{11}})^2\right)e_0 \equiv B^b_{rs}+A^b_{rs}e_0.
\end{aligned}
$$

Here, B_1 and B_2 are the usual bulk ME coefficients of a cubic sample; the $A's$ (namely, A^b_{11}, A^b_{12}, A^b_{13}, A^b_{21}, A^b_{22}, and A^b_{rs}) are the second-order coupling terms. D^b_{11} is the coupling coefficient for $\epsilon_{11}\alpha_1^2$ and $\epsilon_{22}\alpha_2^2$. This coupling gives the familiar magnetostrictive strain parallel to the direction of the magnetization. Similar interpretation can be applied to D^b_{12}. D^b_{13} also gives rise to second-order magnetostrictive strains that tend to be perpendicular to the direction of the magnetization. D^b_{21} and D^b_{22} are coefficients for the shear magnetostrictive strains: D^b_{21} couples ϵ_{12} with $\alpha_1\alpha_2$. D^b_{22} couples ϵ_{13} with $\alpha_1\alpha_3$ and ϵ_{23} with $\alpha_2\alpha_3$. D^b_{rs} is the effective ME coefficient due to the biaxial misfit (or residual) strain. The subscript in the coefficient is to denote that the term comes from the misfit (or residual) strain.[4]

As expected, $D^b_{11} \neq D^b_{12}$ because the film is tetragonally distorted. If $e_0 = 0$, that is, if the misfit strain is zero, then $D^b_{11} = D^b_{12}$ as expected for a cubic crystal. D^b_{13} exists only because of the tetragonal distortion. If the deformation is pure dilation, this coupling coefficient would be zero to be consistent with a cubic crystal symmetry.

[4] D^b_{rs} is used to denote this energy term instead of D^b_{ms} to avoid the confusion with magnetostatic energy

One way to check this in our result is to replace the ratio $-2c_{12}/c_{11}$ with 1.[5] Also, note that if the magnetostrictive strain tensor is to be replaced by the misfit strain tensor, then $D^b_{11} + D^b_{12} + D^b_{13} = D^b_{rs}$ because of the equivalence between magnetostriction and its inverse from the energy viewpoint.

In short, the BME energy of a fcc(001) tetragonally distorted film can be very different from that of its bulk form. In addition to the usual magnetostrictive strains, the misfit strains can contribute to the magnetic anisotropy. Moreover, the two types of strain can interact to give energy terms indicative of the distorted geometry.

2.3.3 Interface Magnetocrystalline Energy

Interface magnetocrystalline energy (IMCE), when described in reference to unrelaxed interfaces, is known as the Néel interface energy. This energy can be found by summing the missing or different bond energies of the interface atoms. For a fcc(001) film/vacuum interface, the MC energy of an interface atom can be found by summing all the nearest neighbor interactions with the atom:

$$\begin{aligned} 2E^{atom}_{imc} &= L(\frac{a_o}{\sqrt{2}})\left(\frac{(\alpha_1+\alpha_3)^2}{2}-\frac{1}{3}\right) \\ &+ Q(\frac{a_o}{\sqrt{2}})\left(\frac{(\alpha_1+\alpha_3)^4}{4}-\frac{6}{7}\frac{(\alpha_1+\alpha_3)^2}{2}+\frac{3}{35}\right) \\ &+ L(\frac{a_o}{\sqrt{2}})\left(\frac{(\alpha_1-\alpha_3)^2}{2}-\frac{1}{3}\right) \\ &+ Q(\frac{a_o}{\sqrt{2}})\left(\frac{(\alpha_1-\alpha_3)^4}{4}-\frac{6}{7}\frac{(\alpha_1-\alpha_3)^2}{2}+\frac{3}{35}\right) \\ &+ L(\frac{a_o}{\sqrt{2}})\left(\frac{(\alpha_2+\alpha_3)^2}{2}-\frac{1}{3}\right) \end{aligned} \tag{2.18}$$

[5]This is to simulate the condition that a biaxial strain in the plane of the film induce a corresponding *expansion* in the vertical direction. The end result is that the film undergoes a pure dilation.

$$
\begin{aligned}
&+ \quad Q(\frac{a_o}{\sqrt{2}})\left(\frac{(\alpha_2+\alpha_3)^4}{4} - \frac{6}{7}\frac{(\alpha_2+\alpha_3)^2}{2} + \frac{3}{35}\right) \\
&+ \quad L(\frac{a_o}{\sqrt{2}})\left(\frac{(\alpha_2-\alpha_3)^2}{2} - \frac{1}{3}\right) \\
&+ \quad Q(\frac{a_o}{\sqrt{2}})\left(\frac{(\alpha_2-\alpha_3)^4}{4} - \frac{6}{7}\frac{(\alpha_2-\alpha_3)^2}{2} + \frac{3}{35}\right).
\end{aligned}
$$

Keeping only the dipole term, the IMCE density can be written in term of $L(\frac{a_0}{\sqrt{2}})$ as follows:

$$
\begin{aligned}
E_{imc} &= \frac{\rho_I}{2} L(\frac{a_0}{\sqrt{2}})\alpha_3^2 \\
&\equiv K_N \alpha_3^2
\end{aligned}
\tag{2.19}
$$

where ρ_I is the interface atomic density; K_N is the Néel interface coefficient.

2.3.4 Interface Magnetoelastic Energy

Interface magnetoelastic energy (IMEE) is the change in the energy (due to deformation) with respect to the undeformed state of the crystal. For a fcc(001) films with two film/vacuum interfaces, the ME of an interface atom can be found from the following expression:

$$
\begin{aligned}
2E_{ime}^{atom} &= \left[L(\frac{a_0}{\sqrt{2}}) + \frac{1}{2}\frac{dL(\frac{a_0}{\sqrt{2}})}{dr}\frac{a_0}{\sqrt{2}}\left(\epsilon_{11}+\epsilon_{33}+2\epsilon_{13}+(1-\frac{2c_{12}}{c_{11}})e_0\right)\right. \\
&\quad \left. + \frac{a_0^2}{8}\frac{d^2L(\frac{a_0}{\sqrt{2}})}{dr^2}(1-\frac{2c_{12}}{c_{11}})e_0\left(\epsilon_{11}+\epsilon_{33}+2\epsilon_{13}+\frac{1}{2}(1-\frac{2c_{12}}{c_{11}})e_0\right)\right] \\
&\cdot \quad \left[\frac{1}{2}\left((\alpha_1+\alpha_3)^2 + (\alpha_1^2-\alpha_3^2)(\epsilon_{11}-\epsilon_{33}) + 2(\alpha_1\alpha_2+\alpha_2\alpha_3)(\epsilon_{12}+\epsilon_{23})\right.\right. \\
&\quad \left.\left. + (\alpha_1^2-\alpha_3^2)(1+\frac{2c_{12}}{c_{11}})e_0\right) - \frac{1}{3}\right]
\end{aligned}
$$

$$
\begin{aligned}
+ & \left[L(\frac{a_0}{\sqrt{2}}) + \frac{1}{2}\frac{dL(\frac{a_0}{\sqrt{2}})}{dr}\frac{a_0}{\sqrt{2}}\left(\epsilon_{11}+\epsilon_{33}-2\epsilon_{13}+(1-\frac{2c_{12}}{c_{11}})e_0\right)\right. \\
& \left. +\frac{a_0^2}{8}\frac{d^2L(\frac{a_0}{\sqrt{2}})}{dr^2}(1-\frac{2c_{12}}{c_{11}})e_0\left(\epsilon_{11}+\epsilon_{33}-2\epsilon_{13}+\frac{1}{2}(1-\frac{2c_{12}}{c_{11}})e_0\right)\right] \\
\cdot & \left[\frac{1}{2}\left((\alpha_1-\alpha_3)^2+(\alpha_1^2-\alpha_3^2)(\epsilon_{11}-\epsilon_{33})+2(\alpha_1\alpha_2-\alpha_2\alpha_3)(\epsilon_{12}-\epsilon_{23})\right.\right. \\
& \left.\left. +(\alpha_1^2-\alpha_3^2)(1+\frac{2c_{12}}{c_{11}})e_0\right)-\frac{1}{3}\right] \qquad (2.20) \\
+ & \left[L(\frac{a_0}{\sqrt{2}}) + \frac{1}{2}\frac{dL(\frac{a_0}{\sqrt{2}})}{dr}\frac{a_0}{\sqrt{2}}\left(\epsilon_{22}+\epsilon_{33}+2\epsilon_{23}+(1-\frac{2c_{12}}{c_{11}})e_0\right)\right. \\
& \left. +\frac{a_0^2}{8}\frac{d^2L(\frac{a_0}{\sqrt{2}})}{dr^2}(1-\frac{2c_{12}}{c_{11}})e_0\left(\epsilon_{22}+\epsilon_{33}+2\epsilon_{23}+\frac{1}{2}(1-\frac{2c_{12}}{c_{11}})e_0\right)\right] \\
\cdot & \left[\frac{1}{2}\left((\alpha_2+\alpha_3)^2+(\alpha_2^2-\alpha_3^2)(\epsilon_{22}-\epsilon_{33})+2(\alpha_1\alpha_2+\alpha_1\alpha_3)(\epsilon_{12}+\epsilon_{13})\right.\right. \\
& \left.\left. +(\alpha_2^2-\alpha_3^2)(1+\frac{2c_{12}}{c_{11}})e_0\right)-\frac{1}{3}\right] \\
+ & \left[L(\frac{a_0}{\sqrt{2}}) + \frac{1}{2}\frac{dL(\frac{a_0}{\sqrt{2}})}{dr}\frac{a_0}{\sqrt{2}}\left(\epsilon_{22}+\epsilon_{33}-2\epsilon_{23}+(1-\frac{2c_{12}}{c_{11}})e_0\right)\right. \\
& \left. +\frac{a_0^2}{8}\frac{d^2L(\frac{a_0}{\sqrt{2}})}{dr^2}(1-\frac{2c_{12}}{c_{11}})e_0\left(\epsilon_{22}+\epsilon_{33}-2\epsilon_{23}+\frac{1}{2}(1-\frac{2c_{12}}{c_{11}})e_0\right)\right] \\
\cdot & \left[\frac{1}{2}\left((\alpha_2-\alpha_3)^2+(\alpha_2^2-\alpha_3^2)(\epsilon_{22}-\epsilon_{33})+2(\alpha_1\alpha_2-\alpha_1\alpha_3)(\epsilon_{12}-\epsilon_{13})\right.\right. \\
& \left.\left. +(\alpha_2^2-\alpha_3^2)(1+\frac{2c_{12}}{c_{11}})e_0\right)-\frac{1}{3}\right].
\end{aligned}
$$

Again, by expanding the above equation and collecting both linear and non-linear terms, the IMEE of the tetragonally distorted fcc(001) film is

$$
\begin{aligned}
E_{ime} &= D_{11}^I\left(\epsilon_{11}(\alpha_1^2-\frac{1}{3})+\epsilon_{22}(\alpha_2^2-\frac{1}{3})\right)+D_{12}^I\left(\epsilon_{33}(\alpha_3^2-\frac{1}{3})\right) \\
&+ D_{13}^I\left(\epsilon_{11}(\alpha_2^2-\frac{1}{3})+\epsilon_{22}(\alpha_1^2-\frac{1}{3})\right)+D_{21}^I\left(\epsilon_{12}\alpha_1\alpha_2\right)
\end{aligned}
$$

$$+ \quad D^I_{22}\left(\epsilon_{13}\alpha_1\alpha_3 + \epsilon_{23}\alpha_2\alpha_3\right) + D^I_{rs}\left(e_0(\alpha_3^2 - \frac{1}{3})\right) \tag{2.21}$$

where

$$\begin{aligned}
D^I_{11} &= \rho_I L(\frac{a_0}{\sqrt{2}}) \equiv B^I_{11}, \\
D^I_{12} &= \frac{\rho_I}{2}\left(3L(\frac{a_0}{\sqrt{2}}) + \frac{1}{2}\frac{dL(\frac{a_0}{\sqrt{2}})}{dr}\frac{a_0}{\sqrt{2}}\right) + \frac{\rho_I}{16}\frac{d^2L(\frac{a_0}{\sqrt{2}})}{dr^2}a_0^2(1 - \frac{2c_{12}}{c_{11}})e_0 \\
&\equiv B^I_{12} + A^I_{12}e_0, \\
D^I_{13} &= \frac{\rho_I}{2}\left(L(\frac{a_0}{\sqrt{2}}) - \frac{1}{2}\frac{dL(\frac{a_0}{\sqrt{2}}}{dr}\frac{a_0}{\sqrt{2}}\right) - \frac{\rho_I}{16}\frac{d^2L(\frac{a_0}{\sqrt{2}})}{dr^2}a_0^2(1 - \frac{2c_{12}}{c_{11}})e_0 \\
&\equiv B^I_{13} + A^I_{13}e_0, \\
D^I_{21} &= \rho_I L(\frac{a_0}{\sqrt{2}}) \equiv B^I_{21} \\
D^I_{22} &= \frac{\rho_I}{2}\left(L(\frac{a_0}{\sqrt{2}}) + \frac{dL(\frac{a_0}{\sqrt{2}})}{dr}\frac{a_0}{\sqrt{2}}\right) + \frac{\rho_I}{8}\frac{d^2L(\frac{a_0}{\sqrt{2}})}{dr^2}a_0^2(1 - \frac{2c_{12}}{c_{11}})e_0 \\
&\equiv B^I_{22} + A^I_{22}e_0, \\
D^I_{rs} &= \frac{\rho_I}{2}\left(-3L(\frac{a_0}{\sqrt{2}})(1 + \frac{2c_{12}}{c_{11}}) + \frac{1}{2}\frac{dL(\frac{a_0}{\sqrt{2}})}{dr}\frac{a_0}{\sqrt{2}}(1 - \frac{2c_{12}}{c_{11}})\right), \\
&+ \frac{\rho_I}{32}\frac{d^2L(\frac{a_0}{\sqrt{2}})}{dr^2}a_0^2\left(1 - 2(\frac{2c_{12}}{c_{11}}) + (\frac{2c_{12}}{c_{11}})^2\right)e_0 \equiv B^I_{rs} + A^I_{rs}e_0.
\end{aligned}$$

where the B^Is are the linear interface ME coupling coefficients, and the D^Is are the second-order ME coupling coefficients. These coupling coefficients have meanings analogous to those of the bulk coupling coefficients. Unlike the bulk energy, $D^I_{11} \neq D^I_{12}$ even if the deformation is a pure dilation. This reflects the broken symmetry at the interfaces. Note that there are no second-order corrections in D^I_{11} and D^I_{21}; that is, A^I_{11} and A^I_{21} are zero.

2.3.5 IMAE of fcc(001) films

Having found the expressions for the bulk and interface MC, and ME energy densities, the intrinsic anisotropy energy density of the film can be obtained with the help of Eq. 2.5:

$$\begin{aligned} E_{film} &= K_s^{eff}\alpha_3^2 + B_{11}^{eff}\left(\epsilon_{11}(\alpha_1^2-\frac{1}{3})+\epsilon_{22}(\alpha_2^2-\frac{1}{3})\right) + B_{12}^{eff}\left(\epsilon_{33}(\alpha_3^2-\frac{1}{3})\right) \\ &+ B_{13}^{eff}\left(\epsilon_{11}(\alpha_2^2-\frac{1}{3})+\epsilon_{22}(\alpha_1^2-\frac{1}{3})\right) + B_{21}^{eff}\left(\epsilon_{12}\alpha_1\alpha_2\right) \\ &+ B_{22}^{eff}\left(\epsilon_{13}\alpha_1\alpha_3+\epsilon_{23}\alpha_2\alpha_3\right) + D_{rs}^{eff}\left(e_0(\alpha_3^2-\frac{1}{3})\right) \end{aligned} \tag{2.22}$$

where

$$\begin{aligned} K_s^{eff} &= -2\frac{K_N}{t}, \\ B_{11}^{eff} &= D_{11}^b - 2\frac{D_{11}^I}{t} = \left(B_1 - 2\frac{B_{11}^I}{t}\right) + A_{11}^b e_0, \\ B_{12}^{eff} &= D_{12}^b - 2\frac{D_{12}^I}{t} = \left(B_1 - 2\frac{B_{12}^I}{t}\right) + \left(A_{12}^b - 2\frac{A_{12}^I}{t}\right) e_0, \\ B_{13}^{eff} &= D_{13}^b - 2\frac{D_{13}^I}{t} = -2\frac{B_{13}^I}{t} + \left(A_{13}^b - 2\frac{A_{13}^I}{t}\right) e_0, \\ B_{21}^{eff} &= D_{21}^b - 2\frac{D_{21}^I}{t} = \left(B_2 - 2\frac{B_{21}^I}{t}\right) + A_{21}^b e_0, \\ B_{22}^{eff} &= D_{22}^b - 2\frac{D_{22}^I}{t} = \left(B_2 - 2\frac{B_{22}^I}{t}\right) + \left(A_{22}^b - 2\frac{A_{22}^I}{t}\right) e_0, \\ D_{rs}^{eff} &= D_{rs}^b - 2\frac{D_{rs}^I}{t} = \left(B_{rs}^b - 2\frac{B_{rs}^I}{t}\right) + \left(A_{rs}^b - 2\frac{A_{rs}^I}{t}\right) e_0. \end{aligned}$$

Here, the effective coefficients are defined to include both linear and second-order contributions. Further, they are defined to include bulk and interface contribution to the anisotropy.

2.4 Discussion

The SP approach, being a localized moment model, is most suited for systems whose magnetic moments are localized; however, it seems to have much success in its applications to transition metals. Good prediction of the magnitude for both surface and bulk MC and ME terms have been reported using the SP approach: in NiFe/Cu system [Gradmann, 1986], in Co/Au system [Bruno, 1988], in Co/Pd system [Victora and MacLauren, 1993], in Co/Cu system [Chuang et. al., 1994]. Further, the SP method has been successfully applied to understand the induced magnetic anisotropy of Ni-Fe alloys [Chikazumi, 1997, p. 299].

Although both the SP and group theory methods consider the anisotropy energy phenomenologically , the former has the advantage over the latter in that the coupling coefficients, to a first approximation, can be expressed in terms of a few Néel parameters. For fcc(001) films, the uniaxial ME coupling coefficients (up to second-order in strain) are written in terms of $L(\frac{a_0}{\sqrt{2}})$, its first and second derivative. Alternatively, they can be expressed in terms of B_1, B_2, and A_{11}^b as shown in table 2.1.

Note that the D_{rs}^{eff} term is the dominant term among all the other ME terms (terms such as $B_{11}^{eff}\epsilon_{11}$ and $B_{12}\epsilon_{33}$) in Eq. 2.22. The reason is that the former has product of e_0e_0 which is much larger than products such as $e_0\epsilon_{11}$ which are in the other ME coefficients. Nevertheless, we choose to keep them in the expression because their values can be calculated from experiments (it will be discussed further in a later chapter). These values can be used for cases where misfit strains are small.

For simplicity, the second-order interactions are not included beyond the product of misfit and magnetostrictive strains. If the misfit strain is large ($\geq$ 0.1%), the product of the magnetostrictive strains can be neglected because magnetostriction in transition metals are usually in the order of 10^{-4}. On the other hand, when the

misfit strain is small, the product of the magnetostrictive strains can also be neglected because the linear terms are the dominant ones. Thus, in either cases, the dropping of the second-order magnetostrictive terms are justified.

The SP model includes only second-order terms that are products with the second derivative of $L(\frac{a_0}{\sqrt{2}})$. Any second-order terms that are multiplied by $L(\frac{a_0}{\sqrt{2}})$ or its first derivative are dropped because they are small compare to the linear terms.

Table 2.1: ME coupling coefficients and K_N^v (film/vacuum interface) expressed in terms of B_1, B_2, and A_{11}^b.

B_{11}^I $\frac{a_0}{16}(4B_1 - B_2)$	B_{12}^I $\frac{a_0}{4}B_1$	B_{13}^I $\frac{a_0}{8}(2B_1 - B_2)$	B_{21}^I $\frac{a_0}{16}(4B_1 - B_2)$	B_{22}^I $\frac{a_0}{32}(5B_2 - 4B_1)$	B_{rs}^I $\frac{a_0}{16}(3B_2 - 4(2 + \frac{2c_{12}}{c_{11}})B_1)$
	A_{12}^b $\frac{1}{2}(1 - \frac{2c_{12}}{c_{11}})A_{11}^b$	A_{13}^b $\frac{1}{2}(1 + \frac{2c_{12}}{c_{11}})A_{11}^b$	A_{21}^b $4\ A_{11}^b$	A_{22}^b $2(1 - \frac{2c_{12}}{c_{11}})A_{11}^b$	A_{rs}^b $\frac{1}{4}\left(-3 - 2\frac{2c_{12}}{c_{11}} + (\frac{2c_{12}}{c_{11}})^2\right)A_{11}^b$
	A_{12}^I $\frac{a_0}{8}(1 - \frac{2c_{12}}{c_{11}})A_{11}^b$	A_{13}^I $-\frac{a_0}{8}(1 - \frac{2c_{12}}{c_{11}})A_{11}^b$		A_{22}^I $\frac{a_0}{4}(1 - \frac{2c_{12}}{c_{11}})A_{11}^b$	A_{rs}^I $\frac{a_0}{16}\left(1 - 2\frac{2c_{12}}{c_{11}} + (\frac{2c_{12}}{c_{11}})^2\right)A_{11}^b$
K_N^v $\frac{a_0}{32}(4B_1 - B_2)$					B_{rs}^b $-\ B_1(1 + \frac{2c_{12}}{c_{11}})$

Chapter 3

Epitaxy of Ni/Cu/Si(001) Films

The growth of Ni/Cu/Si(001) films has been investigated extensively by many research groups [Chang, 1990a; Naik *et. al.*, 1993; Inglefield, 1995; Müller *et. al.* 1996]. The relevant literature on the epitaxy of the system is reviewed in this chapter. Equilibrium models, particularly that by Basson and Ball [1978], are also discussed to explain the strain state of the nickel layer. A synchrotron x-ray study of the films used in this thesis will be presented in the next chapter.

3.1 Background

The word *epitaxy* refers to a single-crystal film that is extended on top of a crystalline substrate [Ohring, 1992, p. 307]. If the film and substrate are made of the same material, the epitaxy is known as homoepitaxy. Heteroepitaxy refers to the case where the film and substrate are made of different materials. Epitaxial Cu/Si(001) and Ni/Cu(001) films are examples of heteroepitaxy.

Due to the chemical interaction between the film and substrate atoms at their common interface, there is a tendency for the lattice of the film to match that of the substrate in such a way to maximize bonding across the interface [Smith, 1995,

p. 222]. [1] In some cases, new phases (which would be unstable in bulk forms) can be stabilized in epitaxial forms. An example of this is the growth of fcc cobalt on a copper substrate [Fujiwara *et. al.*, 1983; Chuang *et. al.*, 1994].

There is a price to pay for having lattice matching. Due to the lattice constant difference between the film and substrate in heteroepitaxy, the film must be strained in order to maintain registry with the substrate lattice. The strain energy stored in the film increases linearly with the film thickness. There exists a critical thickness t_c below which it is energetically more favorable for the film to be coherent with the substrate lattice, and beyond which it is energetically more favorable for the film to be partially coherent to the substrate lattice by introducing extra planes (or misfit dislocations) at the interface. Figure 3.1 illustrates the two different modes of misfit accommodation in a simple cubic material. The quantity that is important in determining the critical thickness t_c is the misfit strain which can be defined as follows:

$$\eta = \frac{a_s - a_f}{a_f} \tag{3.1}$$

where a_s and a_f are the atomic distances of the substrate and film in some crystallographic direction in their *bulk* forms, respectively. For films having lattice parameter mismatch with the substrate larger than 10%, epitaxy is generally not obtainable.

Figure 3.1b is an example of an edge dislocation in the film/substrate interface with the dislocation line lying in the [010] crystallographic direction, and its Burgers vector pointing perpendicular to the dislocation line. Such an edge dislocation provides the most effective means of relieving the misfit strain in the film. [Tsao, 1993, p. 159]. On the contrary, a screw dislocation does not contribute to the relief

[1] It is assumed here that the substrate is much thicker the film. Thus, the substrate provides a rigid lattice on which the film is grown.

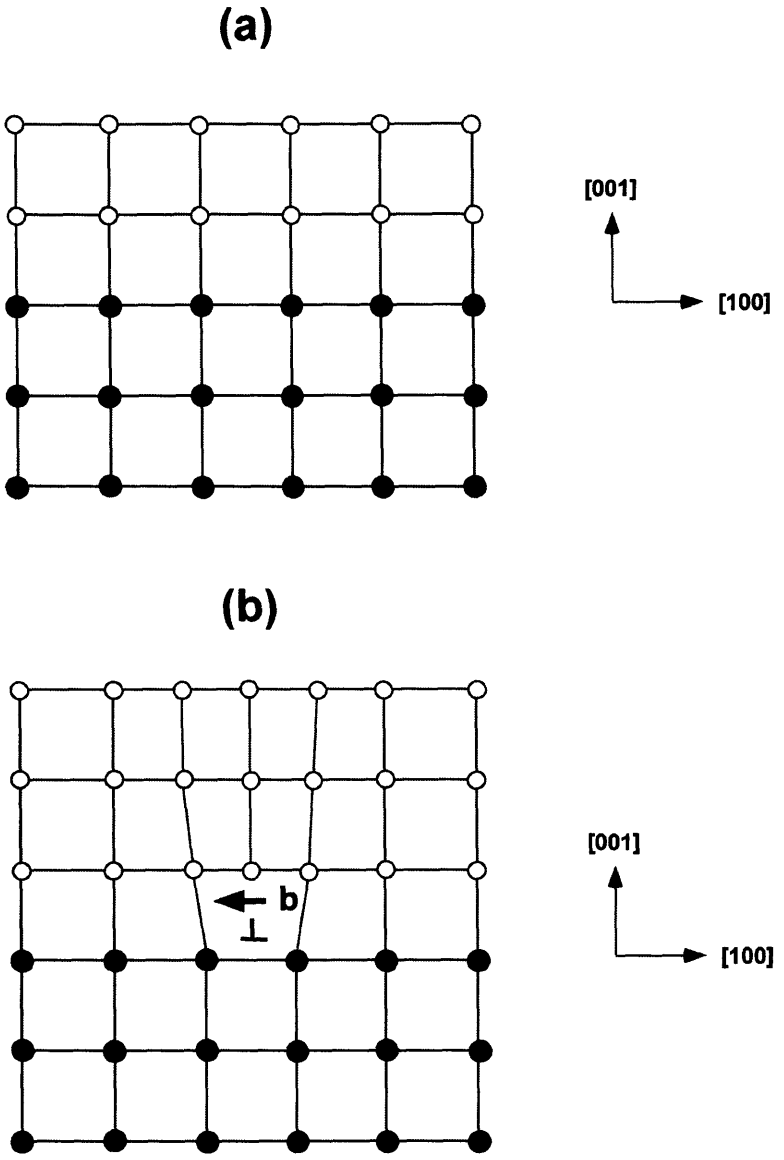

Figure 3.1: Schematics of the two general modes of misfit accommodation in a simple cubic material; a) the misfit is accommodated by straining the lattice; b) misfit strain is partially relieved by the extra atomic plane terminating at the interface, namely an edge dislocation.

of misfit strain because its Burgers vector is parallel to the dislocation line; there is no "extra" plane of atoms involved in its formation.[2]

But not all misfit dislocations (dislocations that form to relieve misfit strain in a film) are edge dislocations. For example, for a fcc metallic film such as copper or nickel, the structure of misfit dislocations tends to have both edge and screw components [Tsao, 1993, p. 161; Smith, 1995, p. 284; Inglefield, 1995, p. 42]. Figure 3.2 shows the geometry of such a mixed dislocation in a fcc (001) film. The dislocation lies on the (111) plane (which is the closest packed plane in a fcc structure), and the dislocation line points in the $[1\bar{1}0]$ direction. The Burger vector is (a/2)[110], which is the shortest possible $\vec{b}$, this being the distance between close-packed atoms. Because dislocations with shorter Burgers vectors are more energetically favorable than those with longer Burgers vectors (because dislocation energy is proportional to $b^2 \equiv |\vec{b}|^2$), this type of dislocations is more commonly observed in fcc metals.

Note that the Burgers vector forms a 60° angle with the dislocation line; hence, these mixed dislocations are also known as 60° dislocations. For the same reason, edge dislocations are also known as 90° dislocations.

3.2 Growth of Cu(001)/Si(001) Films

Epitaxial growth of Cu(001) on Si(001) might seem challenging at first, considering that their lattice parameters are 3.615 and 5.43 Å at room temperature, respectively, which would result in a lattice mismatch of about 50%. However, if the Cu lattice is rotated by 45° about its film normal direction with respect to the Si lattice (that is, the [100] axis of the Cu is parallel to the [110] of the Si), the mismatch would be reduced significantly (to about 6.2%), and thus would make the epitaxial growth

[2]In this chapter, the reader is assumed to have some basic knowledge of dislocation theory. For a review of the theory, please consult Appendix D and the references therein.

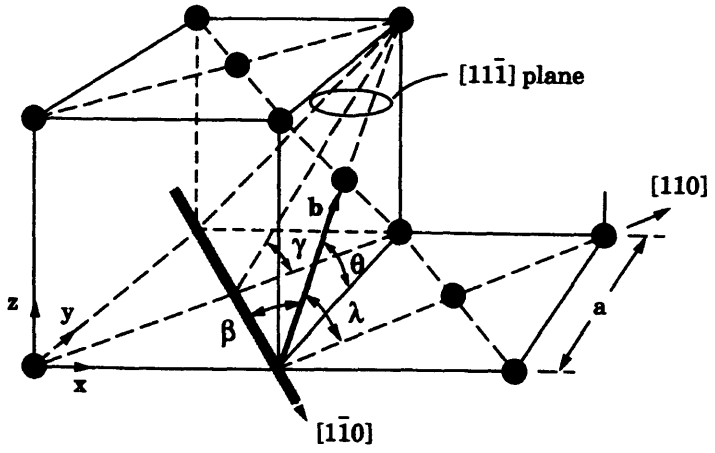

Figure 3.2: Geometry of a 60° dislocation in a fcc cubic material. Only a few of the metal atoms are shown for simplicity. The dark rod is the dislocation with the dislocation line points in the [1$\bar{1}$0] direction (after Smith, [1995], p. 285).

more possible. In fact, the growth of Cu(001) on Si(001) is obtained experimentally; the 45° rotation has been confirmed by in-plane x-ray diffraction [Chang, 1990a], x-ray pole figures [Inglefield, 1995, p.122], RHEED [Demczyk *et. al.*, 1993], and TEM [Demczyk *et. al.*, 1994; Inglefield, 1995].

The growth of Cu on Si is usually done at low temperature ($\leq$ 50°C). The reason is that the two elements form stable and metastable compounds even at room temperature [Bai, 1990; Li, 1992]. It is believed that the Cu/Si interface is initially sharp, but it becomes diffuse within months after the growth. The thickness of the silicide interface is about 100Å as determined by TEM technique [Demczyk, 1994; Inglefield, 1995, p. 124]. For growth at about 100°C, noticeable amount of silicide can be detected within hours [Inglefield, 1995, p. 124]; above 150°C, silicides can even form within minutes, as we will discussed further in the next chapter.

Figure 3.3 shows a portion of the Cu-Si phase diagram. Although the diagram shows phases above 400°C, it is included for completeness and for space group information of the compounds.

It must be said that if the growth temperature is too low ($\leq$ 0°C), no epitaxial growth of Cu(001) on Si(001) could be obtained [Demczyk *et. al.*, 1994].

The growth mode of Cu on Si(001) is still not well understood. However, it has been argued that the growth is by the Volmer-Weber mode [Naik *et. al.*, 1993]. RHEED studies show that Cu films that are less than 150Å thick shows very diffuse pattern; the pattern becomes more defined but spotted for the thicker films. This suggests that epitaxial growth is dominated by three-dimensional growth.

3.3 Growth of Ni(001)/Cu(001) Films

The growth of Ni(001) on Cu(001) is more direct: the nickel lattice is totally or partially commensurate with the Cu. Since the lattice mismatch between them is about 2.6%, epitaxial growth of Ni is favorable and has been frequently observed [Gradmann, 1966; Matthews and Crawford, 1970; Naik *et. al.*, 1993; Chang, 1990a; Inglefield, 1995].

Unlike the case of Cu on Si(001), the interface between Ni(001) and Cu(001) remains sharp at room temperature. It has been shown by Chen *et. al.* [1991] that the Ni on Cu is thermally stable against interdiffusion up to about 200°C. The stability is in part due to the fact that both elements are totally miscible below 150°C, as shown in the phase diagram (figure 3.4).

The growth mode of Ni/Cu(001) has been well studied by Shen *et. al.* [1995] using an *in situ* scanning tunneling microscope. They found that the first 3.5 monolayers of Ni are grown by the classic Frank-Van der Merwe mode (namely, layer-by-layer

Cu-Si

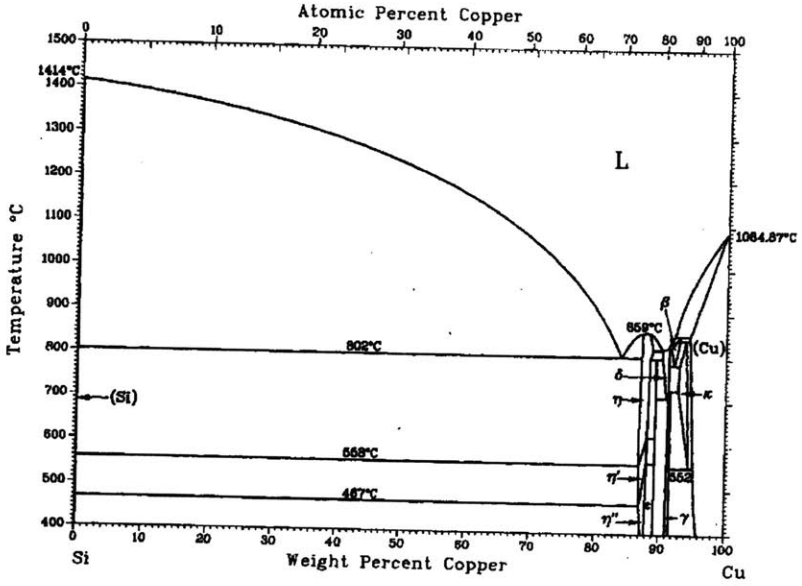

R.W. Olesinski and G.J. Abbaschian, 1986

Phase	Composition, wt% Cu	Pearson symbol	Space group
(Si)	0	*cF*8	$Fd\bar{3}m$
SiII (HP)	0	*tI*4	$I4_1/amd$
η‴(a)	87.2 to 88.16	(b)	...
η′(a)	87.0 to 88.22	(c)	$R\bar{3}$
η(a)	87.2 to 88.8	(c)	$R\bar{3}m$
ε(d)	89.3 to 89.4	(e)	...
δ	90.3 to 91.4	(f)	...
γ(g)	91.4 to 91.62	*cP*20	$P4_132$
β	91.6 to 93.2	*cI*2	$Im\bar{3}m$
κ(h)	93.0 to 94.80	*hP*2	$P6_3/mmc$
(Cu)	94.6 to ~100	*cF*4	$Fm\bar{3}m$
Other reported phases			
η″(j)	...	(f)	...
Metastable	...	(f)	...

(a) Also denoted Cu_3Si. (b) Orthorhombic. (c) Rhombohedral. (d) Also denoted $Cu_{15}Si_4$. (e) Cubic. (f) Tetragonal. (g) Also denoted Cu_5Si. (h) Also denoted Cu_7Si. (j) Originally denoted η′

Figure 3.3: Cu-Si phase diagram (after Baker [1992]).

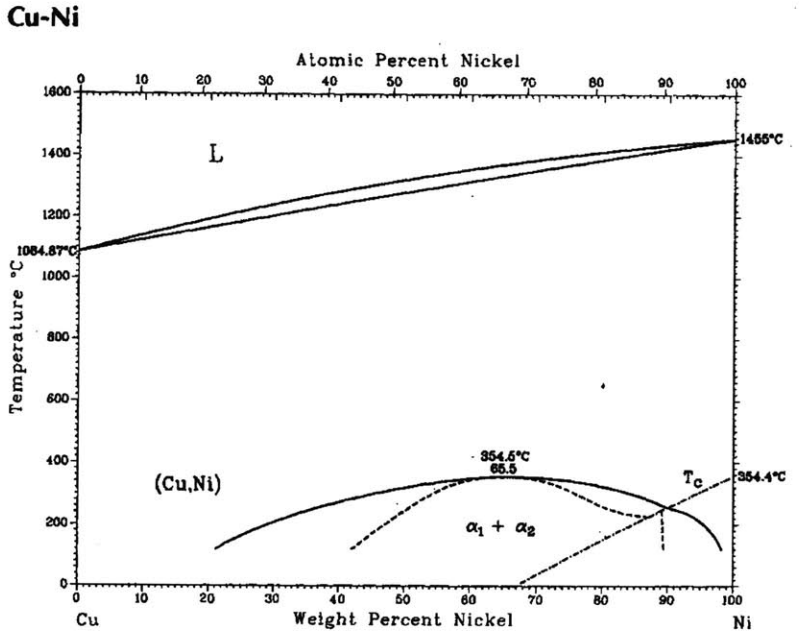

D.J. Chakrabarti, D.E. Laughlin, S.W. Chen, and Y.A. Chang, 1991

Phase	Composition, wt% Ni	Pearson symbol	Space group
(Cu,Ni)	0 to 100(a)	*cF*4	$Fm\bar{3}m$

(a) Above 354.5 °C

Figure 3.4: Cu-Ni phase diagram.

growth).[3] For the nickel films that are thicker than 6 monolayers thick, "multilayer" growth becomes more dominant. The term "multilayer" used by Shen *et. al.* [1995] is perhaps to imply that the growth happens at many layers simultaneously. Further, it was found that the islands have the shape of a three-dimensional plate, which grow in size and height as the film thickness increases. The island edges are along <110> directions, consistent with microfacets of a close-packed fcc crystal.

3.4 Equilibrium Model of Strain

In this section, we will derive an expression to account for the strains in the nickel layer in Cu/Ni/Cu(001) films. An equilibrium model will be employed. We will follow the approach by Basson and Ball closely [1970]. The result will also be used in the next chapter to explain our experimental strain data taken by synchrotron x-ray diffraction.

Equilibrium models of strain in thin films have been considered by many researchers for about five decades: Frank and van der Merwe [1949], Jesser and Matthews [1967], and Matthews and Crawford [1970]; just to name a few.[4] The basic idea is to find the lowest-energy state of the system by minimizing its areal energy density which consists of two parts:

$$U_a = U_{coh} + U_{dis} \tag{3.2}$$

Here, U_{coh} is the strain energy per unit area of the film, and U_{dis} is the excess energy to create the dislocations in a unit film area. It is expected that equilibrium models tend to underestimate the strains in the film. Although kinetic models tend to give

[3]For readers who are interested in different growth modes and stresses in thin films, please consult an excellent review article by Koch [1994].

[4]The article by Fitzgerald [1991] gives a good overview on the approach and the subject in general.

a more accurate account of the strains in thin films, they will not be discussed here. Readers who are interested in kinetic models should consult the article by Fitzgerald [1991] and the references therein.

For simplicity, the Cu buffer layer is assumed to be unaffected by the deposition of the nickel and the Cu cap layers. [5] Then, the areal energy density due to strain can be written as the sum of that of the Ni and the Cu cap layer: [Fitzgerald, 1990, p. 99; Tsao, 1993, p. 164]:

$$U_{coh} = \frac{2G(1+\nu)}{1-\nu}(t_1\epsilon_1^2 + t_2\epsilon_2^2) \tag{3.3}$$

Here, t_1 and ϵ_1 are the film thickness and in-plane strain of the nickel layer; t_2 and ϵ_2 are the film thickness and strain of the Cu cap layer. G and ν are the shear modulus and Poisson's ratio of copper or nickel, respectively (assuming that they are the same for both materials).

From Appendix D, the dislocation energy for a mixed dislocation with the Burgers vector at an angle β to the dislocation line is

$$E_d = \frac{Gb^2(1-\nu\cos^2\beta)}{4\pi(1-\nu)}\mathrm{Log}_e\left(\frac{\alpha R}{r_o}\right) \tag{3.4}$$

where the parameter α is an adjustable factor to account for the core energy, r_o is the core radius, usually taken to be the magnitude of the Burgers vector, b. R is the distance from the dislocation to be included in the energy expression. The areal energy density from the dislocation grids in the Ni and the Cu cap layer can be expressed as follows:

$$U_{dis} = \frac{Gb^2(1-\nu\cos^2\beta)}{4\pi(1-\nu)}\left(2\rho_1\mathrm{Log}_e(\frac{\alpha R_1}{b}) + 2\rho_2\mathrm{Log}_e(\frac{\alpha R_2}{b})\right) \tag{3.5}$$

[5] This assumption turns out to be quite good experimentally as it will be shown in the next chapter

where ρ_1 and ρ_2 are the *linear* dislocation densities of the Ni and the Cu cap layer. The factor of 2 is to reflect the assumption that dislocations form 2 dimensional grids in the plane of the film.

Plugging Eqs. 3.3 and 3.5 into 3.2, and minimizing the total areal energy density with respect to ρ_1 and ρ_2, the equilibrium strain for the Ni and the Cu cap layer can be obtained. But before this step can be taken, we need to express ϵ_1 and ϵ_2 in terms of ρ_1 and ρ_2, respectively. ϵ_1 can be expressed in term of ρ_1 as follows [Fitzgerald, 1990, p. 92; Tsao, 1993, p. 164]:

$$\epsilon_1 = \eta - \rho_1 b_{edge} \tag{3.6}$$

where $b_{edge} = b\sin\beta\cos\gamma$ is the edge component of the Burgers vector projected onto the interface plane: β is the angle between the Burgers vector and the dislocation line, and γ is the angle between the interfacial plane and the slip plane of the dislocation (see figure 3.2).

An expression for ϵ_2 can be obtained by making the assumption that the Cu cap layer grows pseudomorphically on the nickel. This assumption is good if the Cu cap layer is less than 50Å, which is the case in the films used in this thesis. Thus,

$$\begin{aligned} \epsilon_2 &\equiv \frac{a_2 - a_2^\circ}{a_2^\circ} \\ &= \frac{a_1 - a_2^\circ}{a_2^\circ} \\ &= \underbrace{\frac{a_1 - a_1^\circ}{a_2^\circ}}_{\approx \epsilon_1} + \underbrace{\frac{a_1^\circ - a_2^\circ}{a_2^\circ}}_{\approx \eta} \end{aligned} \tag{3.7}$$

where a_1° and a_1 are the lattice constants of bulk nickel and the nickel film, respectively. a_2° and a_2 are the lattice constants of bulk Cu and the Cu cap layer, respectively.

Plugging Eqs. 3.6, 3.7, 3.3, 3.5 into 3.2, and minimizing it with respect to ρ_1, an expression for the in-plane equilibrium strain of the nickel film ($\epsilon_{\parallel}^{e}$) can then be obtained:

$$\epsilon_{\parallel}^{e} = \frac{b}{\sin\beta\cos\gamma}\frac{(1-\nu\cos^2\beta)}{8\pi(1+\nu)}\frac{1}{t_{Cu}+t_{Ni}}\mathrm{Log}_e\left(\frac{t_{Cu}+t_{Ni}}{b/\alpha}\right)+\frac{t_{Cu}}{t_{Cu}+t_{Ni}}\eta \qquad (3.8)$$

Note that we have replaced some of the symbols in Eqn. 3.8 with more descriptive notation for the Cu/Ni/Cu system: $\epsilon_{\parallel}^{e} \equiv \epsilon_1$, $t_{Ni} \equiv t_1$, and $t_{Cu} \equiv t_2$. Also, in writing Eq. 3.8, it has been assumed that the average linear spacing between the dislocations, $1/\rho_1 \equiv s$, is greater than $2(t_{Cu}+t_{Ni})$ for all nickel film thicknesses. Although the BB model gives two different results for the two cases when s is greater and less than $2(t_{Cu}+t_{Ni})$, we find that the difference is not significant in the Cu/Ni/Cu(001) films.

The two terms in Eq. 3.8 can be interpreted as follows: the first is the strain of the film whose thickness is the sum of the film thickness of the Cu cap and nickel layer; the second accounts for the fact that Cu and Ni have different bulk lattice constants, weighed by the thickness of the cap layer. Note that for $t_{Cu} = 0$, we get the usual expression for a single misfit epilayer [Tsao, 1993, p. 166].

If the dislocations in the nickel are assumed to be purely 60° dislocations on {111} slip planes, then $\sin\beta = \sqrt{3}/2$, $\cos\gamma = 1/\sqrt{3}$, and $b = a_{Ni}^{\circ}/\sqrt{2}$ where a_{Ni}° is the lattice constant of bulk nickel. Using $\alpha = 1$, the Poisson's ratio of bulk nickel ($\nu = 0.39$)[6], the equilibrium in-plane strain of the nickel film in Cu(50Å)/Ni(t_{Ni})/Cu(2000Å)/Si(001) films can be computed as a function of the nickel film thickness, and it is plotted in figure 3.5. As expected, the strain decreases with increasing nickel film thickness.

The critical thickness t_c (the thickness below which the nickel is totally commmensurate with the Cu buffer layer) can be found by setting the equilibrium strain

[6]For transition metals, α is usually between 0.5 and 2 [Hirth and Loathe, 1992, p. 232]. We choose $\alpha = 1$ for convenience.

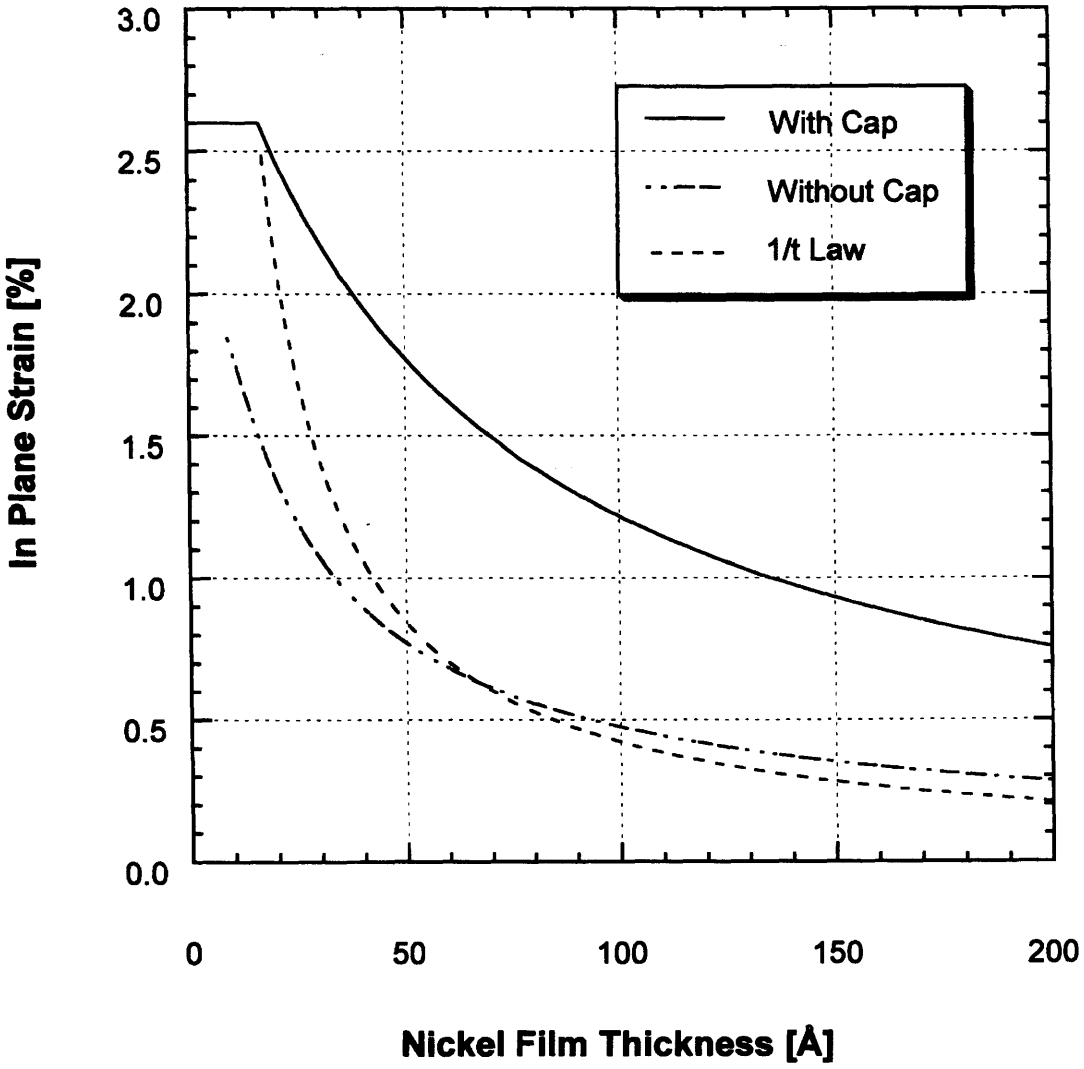

Figure 3.5: Average equilibrium in-plane strain of the nickel layer in Cu(50Å)/Ni(t_{Ni})/Cu(2000Å)/Si(001) films is plotted with the nickel film thickness for a single epilayer (i.e., with the cap Cu layer) and a double epilayers (Ni and Cu cap layer). The result is also compared with the 1/t law which is commonly accepted in the literature.

$\epsilon_{\parallel}^{e} = 2.6\%$ (which is the misfit strain of Ni on Cu), and it is computed to be about 16Å. This value agrees with the experimental result on Ni/Cu(001) system reported by Matthews and Crawford [1970] and Inglefield *et. al.* [1993] using TEM technique.

Note that the in-plane equilibrium strain for the Ni/Cu(001) system is significantly lower than that for the cap Ni layer. This phenomenon has been observed in semiconductor materials [Fitzgerald, 1991, p. 106; Tsao, 1993, p. 172]. It is interesting to note that for a single Ni/Cu(001) film, equilibrium theory fails to predict the existence of the critical thickness t_c as indicated in figure 3.5. This failure has been pointed out by Matthews and Crawford [1970]. But the fact a critical thickness t_c has been observed in the Ni/Cu(001) system suggests that its occurrence may be due to kinetic reasons.

The strain predicted by the 1/t law is also shown in figure 3.5. The equation used for the plot is

$$e_{\parallel}^{e} = \eta \frac{t_c}{t_{Ni}} \tag{3.9}$$

where $t_c = 17$ Å is assumed. Note that the strain drops much faster than that predicted by the BB model for the cap Ni films.

3.5 Summary

The relevant literature of the epitaxy of Cu/Si(001) and Ni/Cu(001) systems has been reviewed. The equilibrium model by Basson and Ball [1978] has been applied to the Cu/Ni/Cu/Si(001) system. The critical thickness is computed to be about 17Å. The theory suggests that the presence of a Cu cap layer can significantly affect the strain in the nickel layer.

Chapter 4

Sample Preparation and Structural Studies

A series of Cu(50Å)/Ni(t_{Ni})/Cu(2000Å)/Si(001) films (17Å $\leq t_{Ni} \leq$ 2000Å) were deposited by electron-beam evaporation in an ultrahigh vacuum chamber. Film epitaxy was monitored by *in situ* reflection high electron enery diffraction (RHEED). Film surface roughness was examined by RHEED and an *ex situ* atomic force microscope (AFM). Both in-plane and out-of-plane strains were measured using sychrotron x-ray radiation.

4.1 Molecular Beam Epitaxy Deposition System

The advent of molecular beam epitaxy (MBE) has made it possible to deposit high quality epitaxial films (i.e., high purity and crystallinity) in a controlled environment. The key factor of its success lies in the ultrahigh vacuum (UHV) condition: the base pressure is less than 10^{-9} torr. The good vacuum makes it possible for films to be grown at a slow rate (usually between 0.5-2.0 Å per second), which is essential for obtaining good epitaxy (incoming atoms have sufficient time to migrate on the slow growing surface). Consequently, the surface of the grown film can be atomically

smooth in many systems [Herman and Sitter, 1996, p. 1]. Another advantage of MBE technique is many surface diagnostic tools (e.g., RHEED and Auger electron spectroscopy) that can be used *in situ* to study and characterize the growth without exposing the film to the lab atmosphere. Thus, MBE is the method of choice for fabricating films whose structures must be tightly controlled.

The Cu/Ni/Cu/Si(001) films used for this thesis work were grown in such a UHV chamber. The use of MBE is important because nickel can grow epitaxially on Cu(001) in an UHV environment. Good epitaxy is essential for the observation of perpendicular magnetization in the nickel layer. Futher, the study of single crystalline nickel allows the possibility of measuring individual ME coupling coefficients independently.

The vacuum in the main chamber is achieved by using a series of pumps, each of which has its own operative pressure range. A Venturi pump is first used to pump the chamber from atomspheric pressure (760 torr) to about 50 torr. Sorption pumps are then used to bring the pressure down to about 10^{-3} torr. A cryogenic pump then takes over, and the pressure can drop to about 10^{-6} within 15 minutes of pumping. An ion pump is then turned on (with the cryogenic pump still on) to help bringing the pressure to about 10^{-8} after a few days of pumping. With a good bake (that is, the chamber is heated to about 150°C for a few days), the pressure of less than 2×10^{-10} torr can be obtained.

Figure 4.1 shows a photograph of the MBE system. A schematic view of the system is shown in figure 4.2. The main chamber is equipped with two electron-beam evaporators (Cu and Ni), a RHEED setup, and a mass spectrometer. It is connected with a load-lock chamber which is isolated by a UHV gate-valve. The load-lock chamber has its own cryogenic and ion pumps. The utility of the load-lock chamber is that samples can be loaded in or taken out without breaking the vacuum in the

main chamber. In a good day, three high-quality films can be fabricated.

Figure 4.3 illustrates the evaporation process. A stream of electrons is accelerated through a field of 10 kV and is focused onto the evaporant surface by a transverse magnetic field provided by a combination of magnetic pole pieces and an electromagnet. The electron source is supplied by a tungsten filament via thermionic emision process. The source material is evaporated due to the heating by the electron bombardment [Herman and Sitter, 1996].

4.2 Substrate Preparation and Film Growth

The Si(001) p-type substrate was dipped in dilute hydrofloric solution (5 % by volume) for ten seconds to remove the native oxide. It was then rinsed in de-ionized water for about 2 minutes and immediately transferred into the load-lock chamber to be pumped down.[1] After several hours in the lock-lock, the substrate is transferred into the main chamber. The RHEED patttern shows sharp streaky diffraction lines and Kikuchi lines, which indicate a clean Si surface.

The growth rates of the copper and nickel layers were 1.0Å/sec. The deposition rate and thickness were monitored by an Inficon photomultiplier rate monitor which was calibrated using a Dektak profilometer. The error in the film thickness is estimated to be 10% of the total thickness.

The growth temperatures of both copper and nickel started at around 20°C and could gradually increase up to about 50°C during the deposition due to the thermal radiation from the sources.

The copper buffer layers for all the samples except the 500 and 2000Å films were

[1]Lyer *et. al.* [1990] shows that the use of HF treatment of a Si substrate leaves the surface hydrogen passivated, which is inert for several minutes in air and several days in UHV at room temperature.

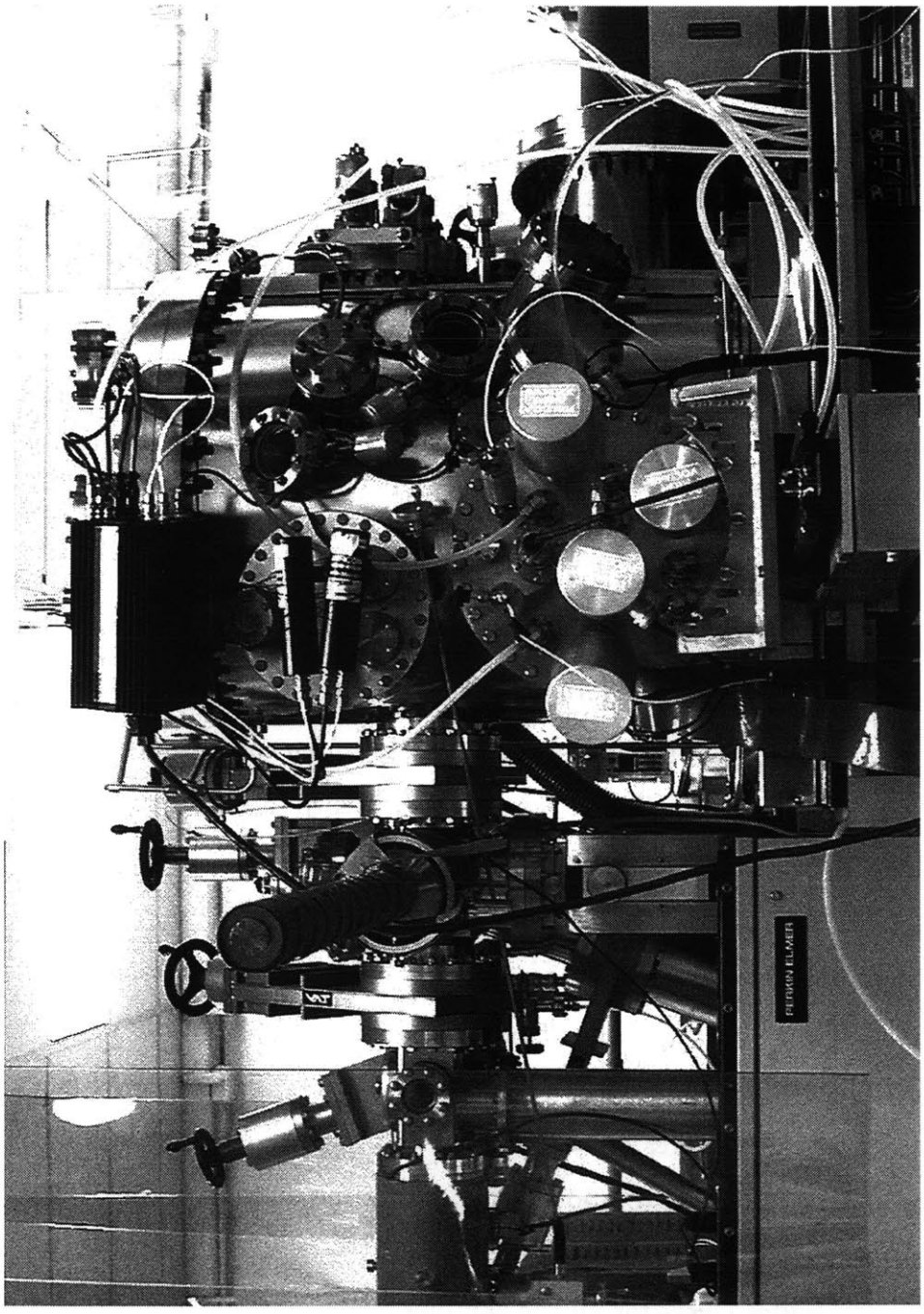

Figure 4.1: Side view of the MBE system (photographed by Hans Nembach; processed in Photoshop by Kin Ha).

7in

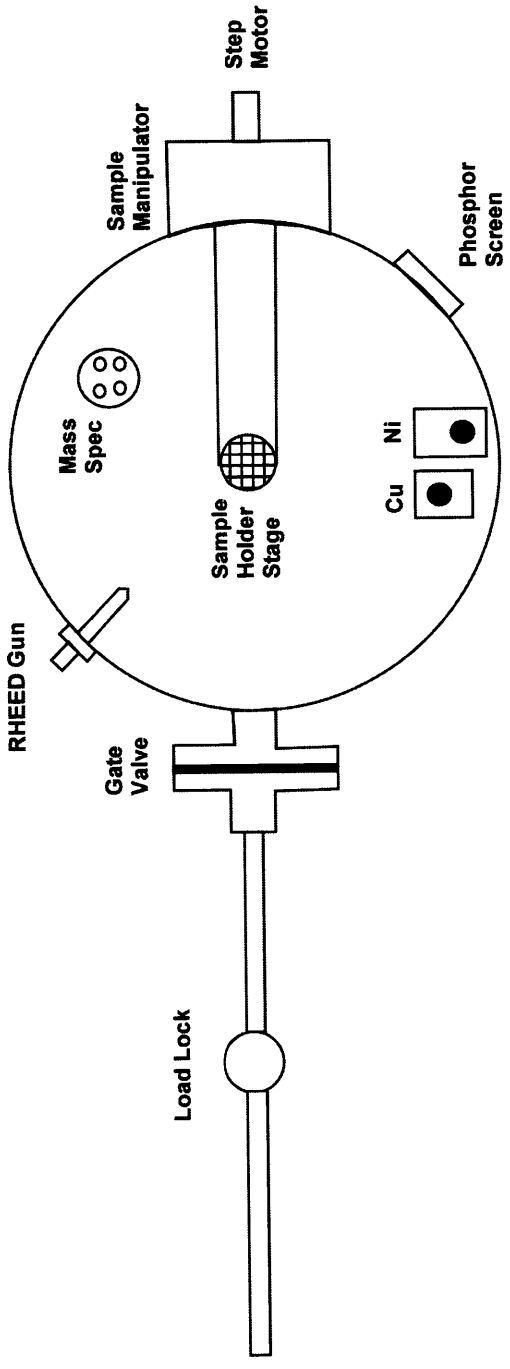

Figure 4.2: Schematic top view of the MBE system.

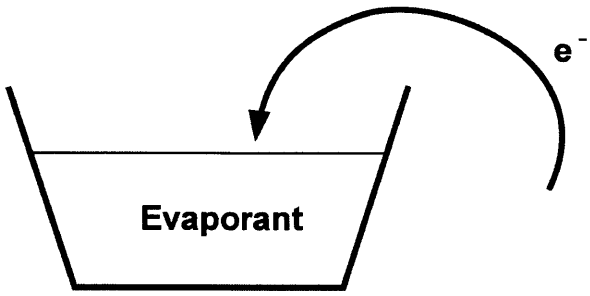

Figure 4.3: Schematic side view of the electron-beam evaporation setup.

annealed *in situ* to about 150°C for eight minutes and then cooled down to 20°C prior to the deposition of the nickel layer. The annealing process improved the flatness of the buffer layer surface. Figure 4.4a shows the RHEED pattern of a 2000Å copper film on Si(001) before the anneal. The spottedness of the pattern indicates that the surface of the copper film was atomically rough. Figure 4.4b shows the RHEED pattern of the same film after the anneal. The streaky RHEED pattern suggests that the the surface was atomically flat. Figure 4.5 shows an surface of an annealed 1000Å copper film imaged by an atomic force microscope (AFM); the root mean square (rms) roughness of the film is 6Å over a $1\mu m \times 1\mu m$ surface area. Contrary to what was reported by Shen *et. al.* [1995], the surface retains its smoothness after the deposition of the nickel and copper cap layer as suggested by RHEED patterns.

Annealing of epitaxial Cu(2000Å)/Si(001) films above 200°C appears to cause the formation of copper silicide through the copper buffer layer. Figure 4.6 is a scanning electron micrograph of a Cu(2000Å)/Si(001) film that was annealed at around 200°C for about a minute. The image shows islands of copper silicide on the copper film as indicated by Auger spectroscopy and microanalysis. X-ray study confirms that at least some of the silicide was $Cu_{15}Si_4$, as discussed later in the chapter. However, no silicon could be detected by Auger spectroscopy on the surface of the copper buffer

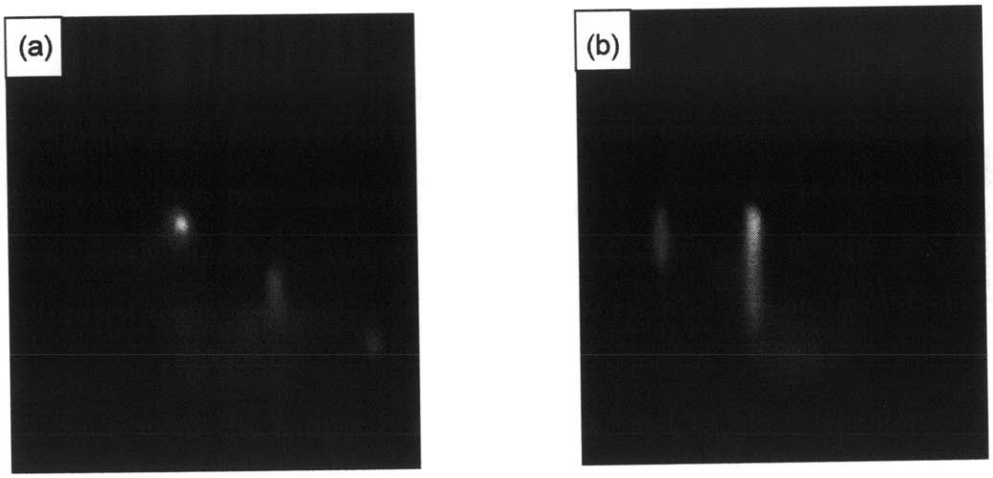

Figure 4.4: RHEED patterns recorded from a Cu(2000Å)/Si(001) surface in the [200] arimuth: a) is the surface of the copper without the intentional anneal; b) is the surface after the copper was annealed at about 200°C for about one minute.

layer that was annealed *in situ* at 150°C for less than eight minutes.

4.3 X-Ray Diffraction Study

The x-ray experiments were performed using the beamline X3B1 of the Brookhaven National Synchrotron Light Source to determine the lattice constants of the nickel and copper layers. Synchrotron radiation was used for its high intensity. The wavelength of the radiation was selected to be 1.149Å by a double crystal Si(111) monochromator; the scattered x-rays were analyzed by a Ge(111) crystal to provide high angular resolution. Both the Bragg and grazing-incidence diffraction setups (see figure 4.7) were calibrated using an Al_2O_3 powder reference standard. The resolutions for both systems were on the order of 0.02° in scattering angle 2θ.

Diffraction from the copper buffer layer was used to align the sample with the incident beam for both the in-plane and out-of-plane lattice measurements. Because

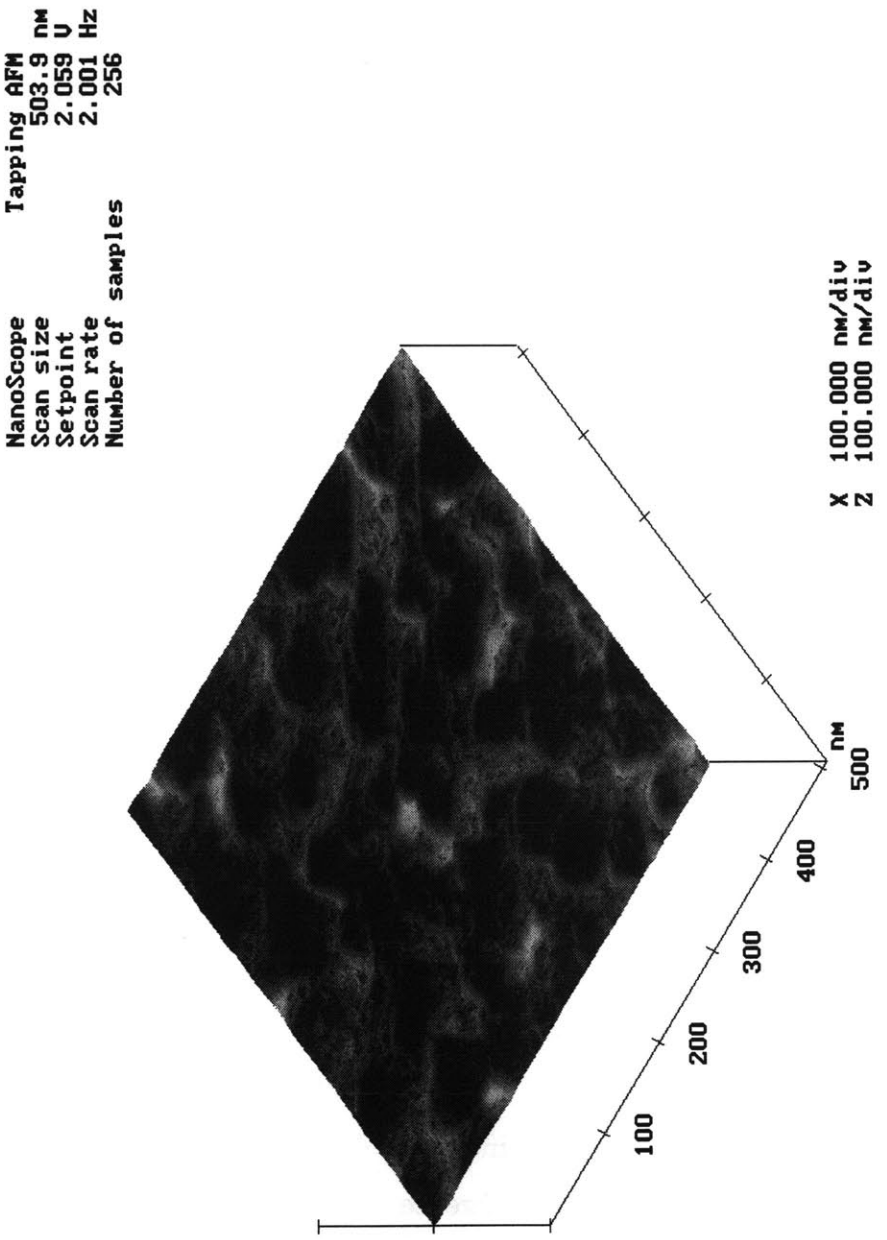

Figure 4.5: Surface of Cu(1000Å)/Si(001) film is imaged by an atomic force microscope.

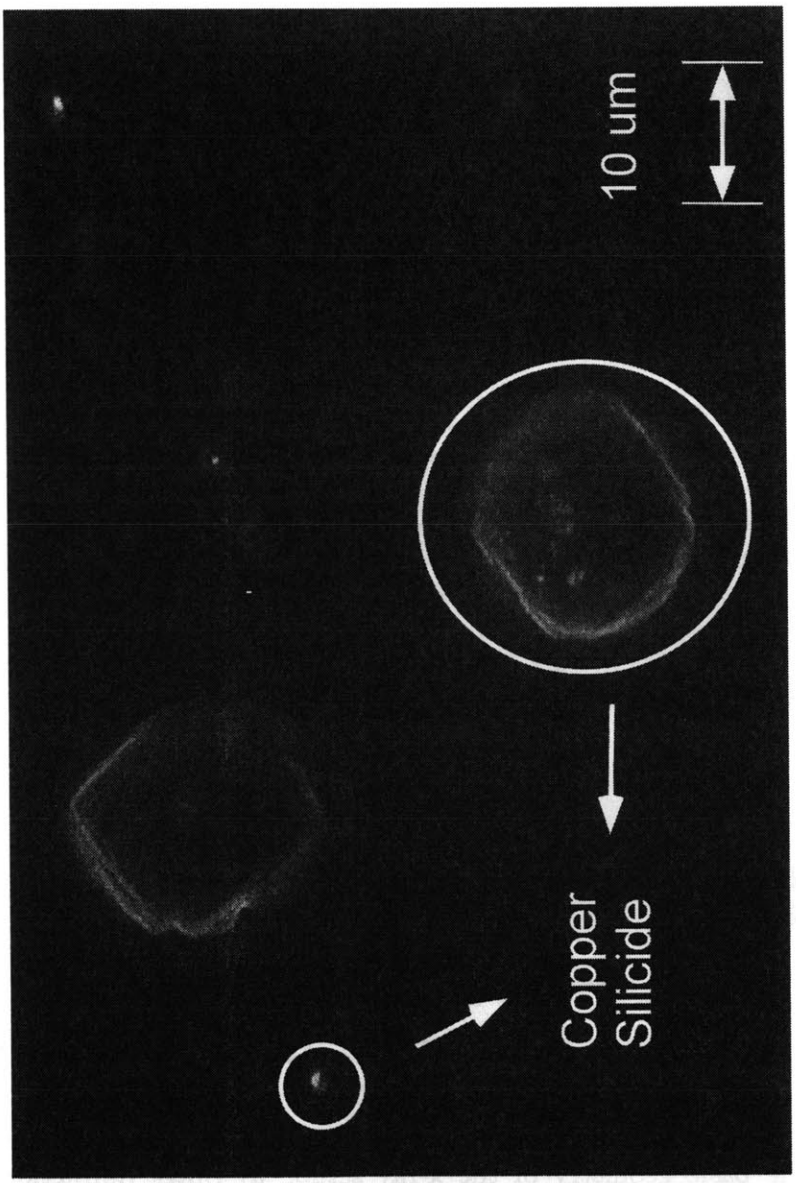

Figure 4.6: SEM image of Cu(2000Å)/Si(001) film annealed at 200° for about one minute. Islands of copper silicide threaded through the copper layer. The islands come in two sizes.

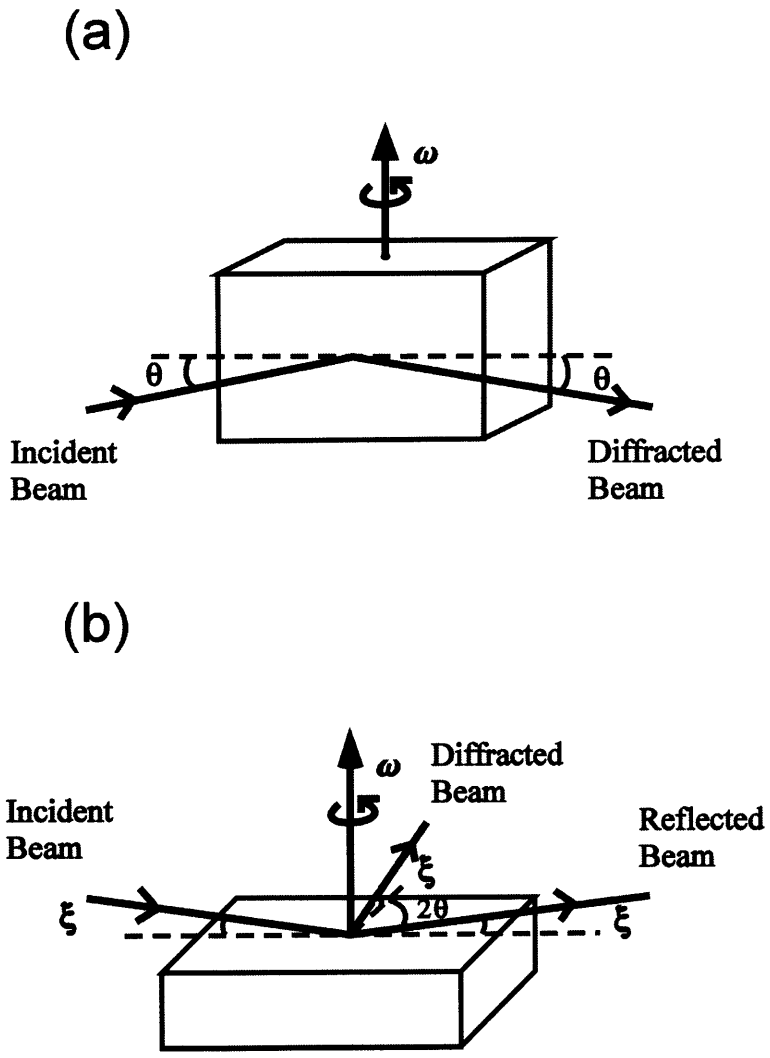

Figure 4.7: The basic geometry of the x-ray setup: a) Bragg diffraction; b) grazing-incidence diffraction (GID).

the lattice of the copper buffer layer is known with respect to the silicon substrate (see chapter 3), the sample was first aligned by eye upon placing it onto the sample holder. The detector was then set at an expected scattering angle 2θ. The sample was rocked about the angle θ with respect to the incident beam (by changing the angle ω) to maximize the intensity at the detector. The condition of maximum intensity is a Bragg condition. The crystal was then aligned by setting $\omega = \theta$; that is to say, the Bragg planes were parallel with the incident beam when θ is at zero degree. This procedure works even if the initial angle θ is slightly off from the true Bragg angle for the copper peak. Once the copper film is aligned, the nickel is also aligned by virtue of its epitaxial growth on the copper. This epitaxial relationship between the nickel and copper will also be confirmed by the diffraction experiments, as it is now discussed.

4.3.1 Symmetric Bragg Diffraction

The out-of-plane lattice constant of the nickel, denoted as $a_{\perp}^{Ni}$, was measured using the symmetric Bragg diffraction method. The intensities from the (002) planes of the copper and nickel are shown in Figure 4.8. Note the logarithmic scale in the y-axis. The copper peak position stays at its bulk value for all the nickel film thicknesses; the nickel peak evolves toward its bulk value with the increasing nickel film thickness. The 500Å and 2000Å nickel films still show considerable vertical contraction, signifying that they are not fully relaxed. There is a peak between that of the copper and nickel, which is particularly pronounced for the thinner films. It is believed to come from the diffraction by the (521) planes of the ϵ-$Cu_{15}Si_4$ cubic phase. The d-spacing calculated from the diffraction peak is 1.756Å; the reported value in the literature is 1.767Å [Mukherjee *et. al.*, 1969]. Other peaks of the $Cu_{15}Si_4$ phase were also detected in the annealed samples using Cu K_α radiation. However, it must be pointed out that other

workers had reported the copper silicide at the Cu/Si interface to be η''-Cu_3Si phase instead [Weber *et. al.*, 1983; Chang, 1990a; Demczyk *et. al.*, 1994; Inglefield, 1995].

For the thinner nickel films (30Å $\leq t_{Ni} \leq$ 150Å), since there is a large difference in the intensity between the copper and nickel peak, the fitting of the nickel peak is very sensitive to the tail of the copper profile. The following procedure was used to extract the nickel diffraction data: the copper peak was first fitted with much weight being placed on its low-θ tail. The fitting was best achieved with a mixture of a gaussian and lorentzian functions. The fitted curve was then used to subtract the copper contribution from the reflectivity data. The remaining intensity was assumed to be that of the nickel and $Cu_{15}Si_4$, each of which was fitted with a gaussian. For the 500Å or 2000Å nickel film, both the nickel and copper cap layer were fitted simultaneously with strictly gaussian functions. The intensity from the copper silicide can be safely neglected for these two nickel film thicknesses. The computed lattice constants (using the Bragg formula) are tabulated in Table 4.1. It must be said that the contribution of the copper cap layer was ignored in the analysis. The assumption is that the cap layer is completely coherent with the nickel and thus does not produce any shift in the nickel peak position. In this respect, the out-of-plane lattice constant tends to be slightly overestimated.

As expected, no (111) diffraction peaks could be detected in the $\theta - 2\theta$ scan. It shows that these films are either highly texture or epitaxial (002) films. However, the grazing-incident diffraction result rules out the former case, as it is now disccused.

4.3.2 Grazing-incident Diffraction

The in-plane lattice constant of the nickel was measured in the grazing-incidence diffraction (GID) geometry (see figure 4.7). In this setup, the incident beam is fixed at a grazing angle ξ relative to the sample surface. The detector is placed in the

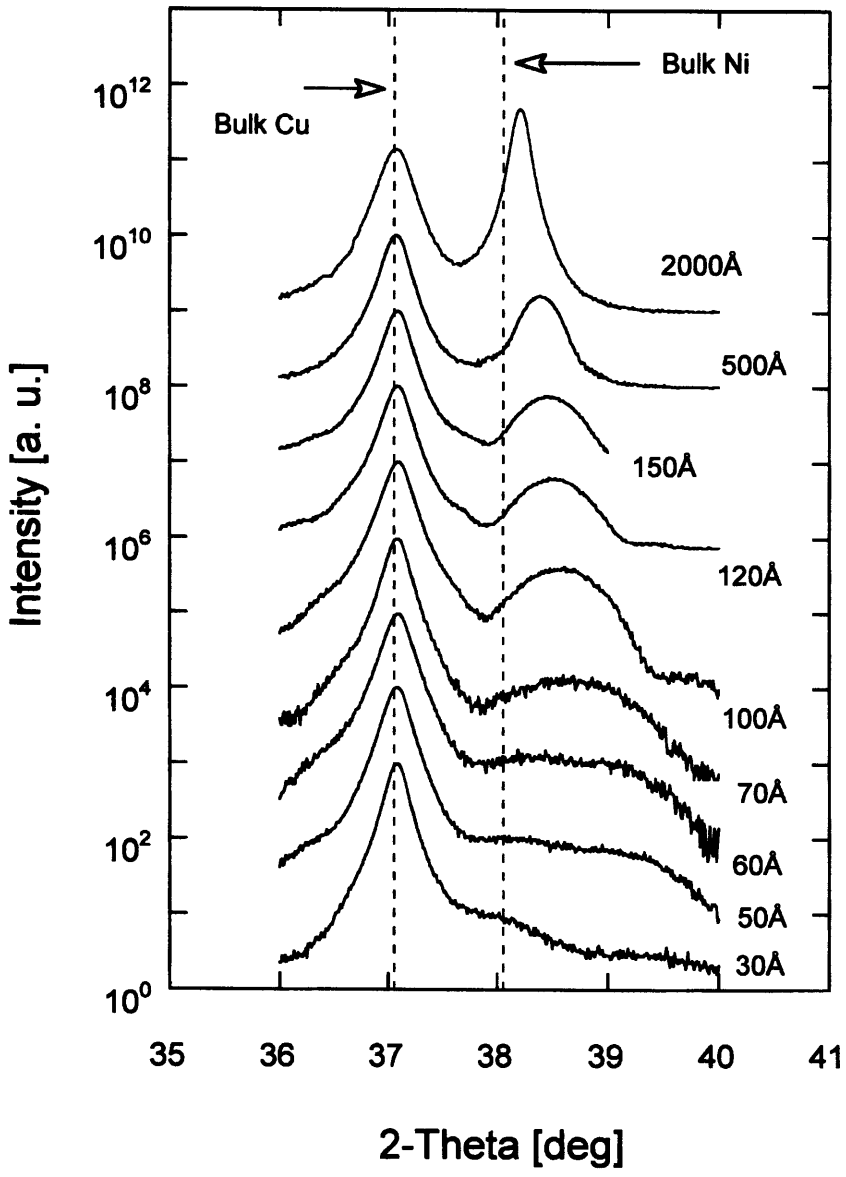

Figure 4.8: X-ray reflectivity from the (002) Bragg planes of the copper and nickel layer in the Cu/Ni/Cu/Si(001) films. The wavelength of the radiation is 1.149Å. All curves are displaced vertically by arbitary amounts.

Table 4.1: In- and out-of-plane nickel lattice constants ($a_{\parallel}$ and $a_{\perp}$) are tabulated for the various nickel film thicknesses using the (200) and (002) diffraction peaks, respectively. Strains are computed by using the formula $(a - a_b)/a_b$ where a_b (=3.5241Å) is the bulk lattice constant of nickel. The in-plane strains are calculated using the $\xi = 0.6°$ data except for the 50Å and 70Å films, the $\xi = 0.3°$ data are used to calculate the strains. The value for $2c_{12}/c_{11}$ is found by taking the ratio of $\epsilon_{\perp}$ and $\epsilon_{\parallel}$.

t_{Ni}[Å]	$a_{\perp}$[Å]	$\epsilon_{\perp}$[%]	$a_{\parallel}$[Å] ($\xi = 0.6°$)	$a_{\parallel}$[Å] ($\xi = 0.3°$)	$\epsilon_{\parallel}$[%]	$-2c_{12}/c_{11}$
30	3.4180	-3.01	3.6038		2.26	1.33
50	3.4433	-2.30	3.5884	3.5908	1.89	1.21
60	3.4514	-2.07	3.5878		1.81	1.14
70	3.4604	-1.82	3.5774	3.5767	1.49	1.21
100	3.4779	-1.31	3.5652		1.17	1.12
120	3.4834	-1.15	3.5626		1.09	1.06
150	3.4873	-1.04	3.5557		0.90	1.16
500	3.4945	-0.84	3.5482		0.68	1.23
2000	3.5107	-0.38	3.5353		0.32	1.20

plane parallel to and slightly above the surface plane of the sample. The diffraction data from Bragg planes that are exactly or nearly perpendicular to the surface of the sample are collected. Figure 4.9 shows the intensity diffracted from the (200) planes with $\xi = 0.6°$. As before, the peak of the the copper buffer layer (if observed) stays at its bulk value for all the nickel films, and the nickel peak evolves toward its bulk value with the increasing nickel film thickness. Note that the (521) $Cu_{15}Si_4$ peak was not observed in this setup, which suggests that the silicide was buried well below the nickel/copper buffer interface.

The penentation depth of the radiation could be varied by changing the grazing angle ξ. Figure 4.10 shows the diffracted intensity of the 50Å and 70Å nickel films with two different values of ξ (0.3° and 0.6°). Very little scattered intensity was observed from the copper buffer layer for $\xi = 0.3°$. These results show, as expected, that the intensity of the beam is very sensitive to the ξ parameter. It must be said that there is a considerable error ($\pm$ 0.1°) in determining the absolute value of ξ. The major source of the error comes from the mounting of the sample which might not be completely flat on the sample holder.

The GID intensities were fitted with gaussian functions. Since the diffracted intensity from the copper buffer layer is comparable to that of the thin nickel film due to the shallowness of the incident angle ξ, both peaks were analyzed at the same time. For the cases with $\xi = 0.3°$, only one gaussian was needed. As before, we assume the copper cap layer is completely coherent with the nickel. Thus, the contribution of the copper cap layer was ignored in the fitting (except for the 2000Å where a slight asymetry of its peak was observed). The computed in-plane lattice constants are tabulated in Table 4.1.

The diffraction from the (220) Bragg planes was also studied by GID on the 30Å and 60Å nickel films. Figure 4.11 shows the diffraction intensity of these samples

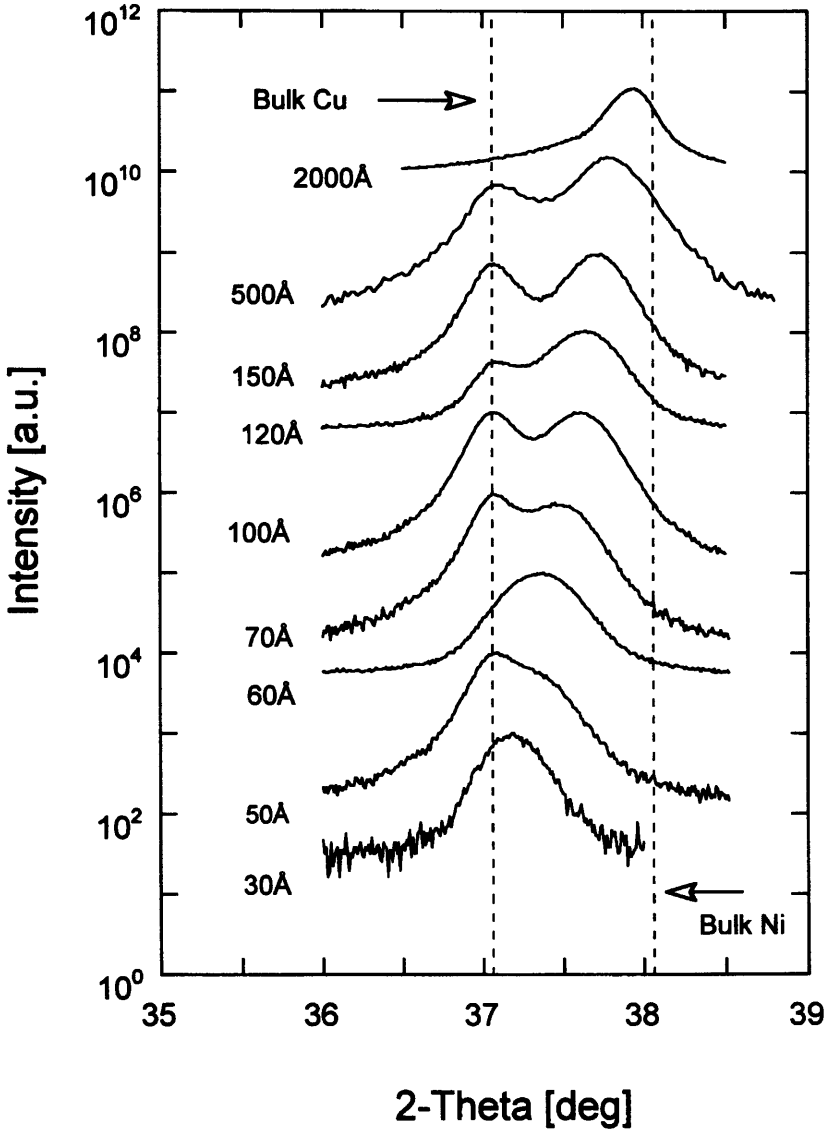

Figure 4.9: Grazing-incidence diffraction (with $\xi = 0.6°$) from the (200) Bragg planes of the copper and nickel layer in the Cu/Ni/Cu/Si(001) films. The wavelength of the radiation is 1.149Å. All curves are displaced vertically by arbitary amounts.

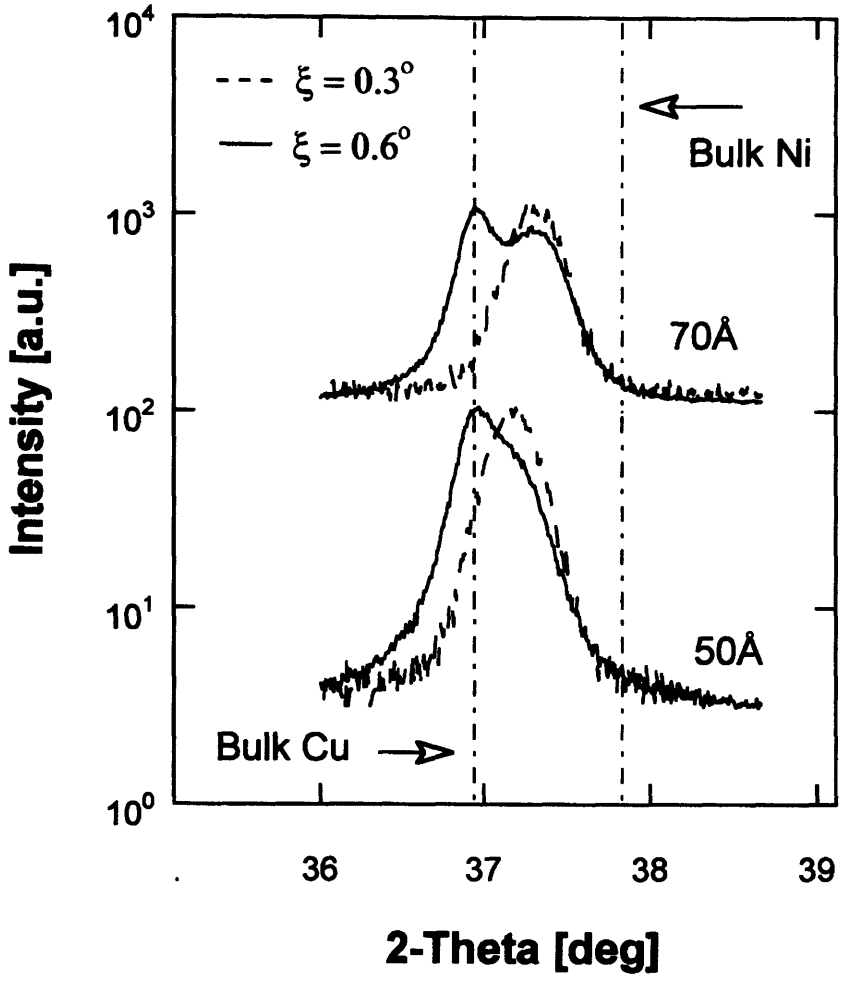

Figure 4.10: Grazing-incidence diffraction from the (220) Bragg planes of the copper and nickel layer in the Cu/Ni/Cu/Si(001) films at two incident angles (0.3° and 0.6°). The wavelength of the radiation is 1.149Å. All curves are displaced vertically by arbitary amounts.

Table 4.2: In-plane lattice constants ($a_{\|}$) were calculated using the (220) diffraction peaks with $\xi = 0.3°$ and 0.6°. The strain is calculated using the formula $(a - a_b)/a_b$ where a_b (=3.5241Å) is the bulk lattice constant of nickel.

t_{Ni}[Å]	ξ	$a_{\|}$	$\epsilon_{\|}$[%]
30	0.3	3.6066	2.34
30	0.6	3.6016	2.20
60	0.3	3.5894	1.85
60	0.6	3.5912	1.90

with $\xi = 0.3°$ and 0.6°. The in-plane lattice constant calculated from these (220) peaks are in good agreement to that which was found from the (200) peaks, and they are tabulated in Table 4.2. One advantage of using the (220) peaks is that they show more separation than do the (200) peaks. For bulk copper and nickel, the separation is 1.5° for the (220) peaks and 1.0° for the (200) peaks. The disadvantage is that the intensity of the former is about half of that of the latter.

To confirm that these films are indeed epitaxial (002) films (as opposed to just highly textured films), the samples were deliberately misaligned with the x-ray beam. Then, the (200) and (220) peak scans were made. As expected, no trace of diffraction could be detected.

4.3.3 Strain in the Nickel Layer

The nickel, upon being deposited onto the copper, is under a biaxial strain due to the lattice mismatch between bulk nickel and copper, and a out-of-plane compressive strain due to the Poisson effect. The misfit strain of the nickel on copper is 2.6% (see Chapter 3). Figure 4.12 shows both the in-plane and out-of-plane average nickel

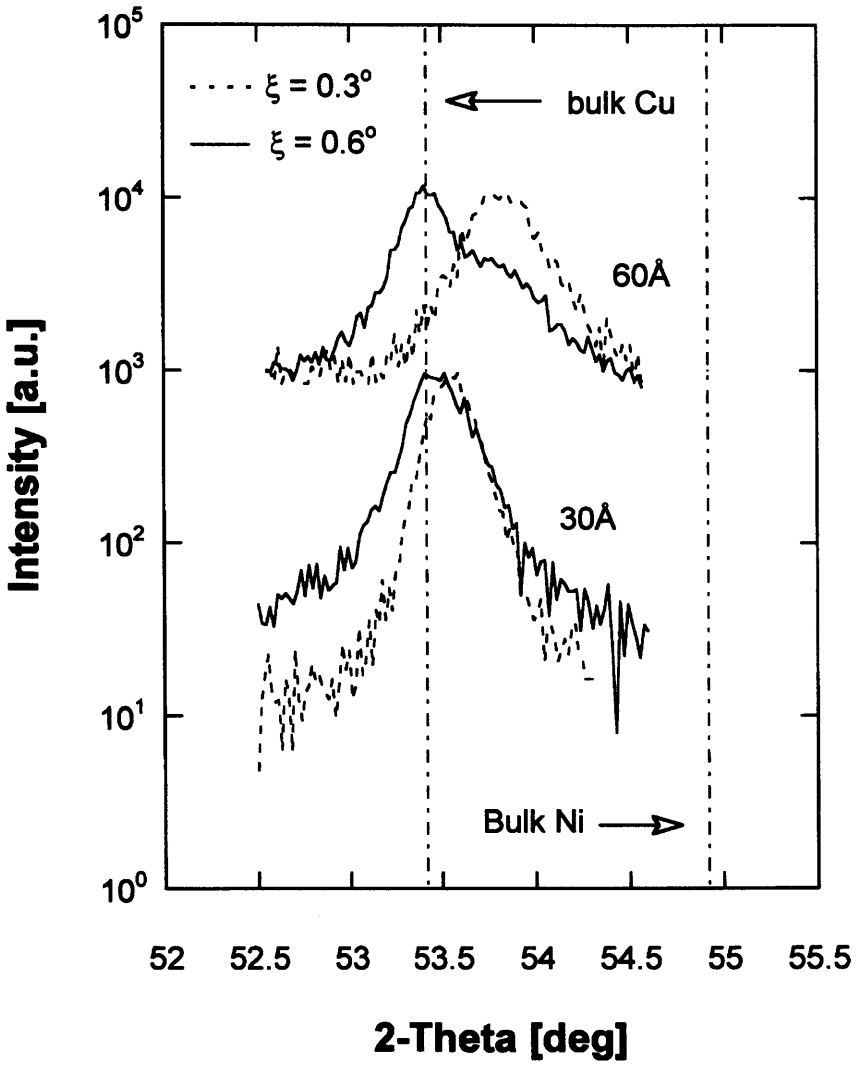

Figure 4.11: Grazing-incidence diffraction from the (220) Bragg planes of the copper and nickel layer in the Cu/Ni/Cu/Si(001) films at two incident angles (0.3° and 0.6°). The wavelength of the radiation is 1.149Å. All curves are displaced vertically by arbitary amounts.

residual strain (denoted as $\epsilon_{\|}$ and $\epsilon_{\perp}$ respectively) as a function of the nickel film thickness. The strains are calculated using the formula $(a - a_b)/a_b$ where a is the measured lattice constant, and a_b (3.5241Å) is the bulk lattice constant of nickel. The values are also given in Table 4.1. The ratio $\epsilon_{\perp}/\epsilon_{\|}$ fluctuates closely around the bulk value $2c_{12}/c_{11} = 1.28$ (see Table 4.1). The Poisson's ratio ν is calculated to be 0.39 using the formula $2c_{12}/c_{11} = 2\nu/(1\text{-}\nu)$.

One simple way of analyzing and predicting the thickness dependence of the strain is to first fit the in-plane strain data (better resolution than out-of-plane) using the equation $\eta(t_c/t_{Ni})^p$ where η (=2.6%) is the misfit strain of the nickel on copper, t_c and p are the fitting parameters. The out-of-plane strain curve is then found by the formula $\epsilon_{\perp} = -(2c_{12}/c_{11})\epsilon_{\|}$, and it is in good agreement with the experimental result. A natural interpretation of the parameter t_c is that it is the critical thickness below which the nickel is coherent with the copper buffer layer. But it must be noted that there is no theorectical basis to think that this is indeed the true critical thickness, and in fact, it is not, as we shall see. With $t_c = 27$Å, and $p = 2/3$, the power law gives a good fit to the data (see Figure 4.12), if it is restricted only to films that are less than 150Å thick. One justification for the restriction is that both the in-plane and out-of-plane are better fitted if the data from the 500Å and 2000Å film are excluded. A better justification comes from the equilibrium model by Basson and Ball which we now discuss.

Figure 4.12 shows the in-plane and out-of-plane strain of the nickel layer as predicted by the BB model (see chapter 3) along with the experimental data. Observe that the theory gives good agreement with the data for $t_{Ni} < 150$Å. However, the thicker films (500Å and 2000Å) show large deviation from the equilibrium strain, which is in agreement with other studies [Gradmann, 1966; Matthews and Crawford, 1970]. The reason for this departure is not well understood. It has been argued

by Matthews and Crawford [1970] that the misfit dislocations could not reach their equilibrium density due to perhaps the tangling of dislocations.

Figure 4.12 also shows the 1/t curve using $t_c = 27$Å for a useful comparison with the $(1/t)^{2/3}$ law. Observe that the strain predicted by the 1/t law drops much faster than that of the experimental values and the BB model. The failure of the 1/t law, as it is applied in this system, is due to two factors in its derivation: i) the influence of the cap layer is ignored; ii) the following assumption is not good even if t_{Ni} is just a few times larger than t_c:

$$\epsilon_{\parallel} = \eta \frac{t_c}{t_{Ni}} \frac{ln(\frac{t_{Ni}}{b/\alpha})}{ln(\frac{t_c}{b/\alpha})} \approx \eta \frac{t_c}{t_{Ni}}. \tag{4.1}$$

The linear dislocation density ρ can be estimated using the following formula:

$$\rho = \frac{\eta - \epsilon_{\parallel}}{b \sin\beta \cos\gamma} \tag{4.2}$$

where b is the magnitude of the Burgers vector. β and γ are defined in figure 3.2. The result for both the equilibrium and measured dislocation densities are plotted in Figure 4.13. Note that for the thicker films ($t_{Ni} > 500$Å), the dislocation density is slightly above a heavily plastically deformed crystal [Kingery *et. al*, 1976, p. 167]. The linear dislocation spacing, $s = 1/\rho$, is also plotted on the same figure.

4.4 Summary

The Cu(50Å)/Ni(t_{Ni})/Cu(2000Å)/Si(001) films (17Å $\leq t_{Ni} \leq$ 2000Å) are atomically smooth as shown by RHEED and AFM. Perpendicular and in-plane strains of the nickel films have been measured independently and accurately using symmetric Bragg and grazing-incidence diffraction respectively. The 2000Å copper buffer layer is unstrained by nickel films up to 2000Å in thickness. The strain in the nickel layer

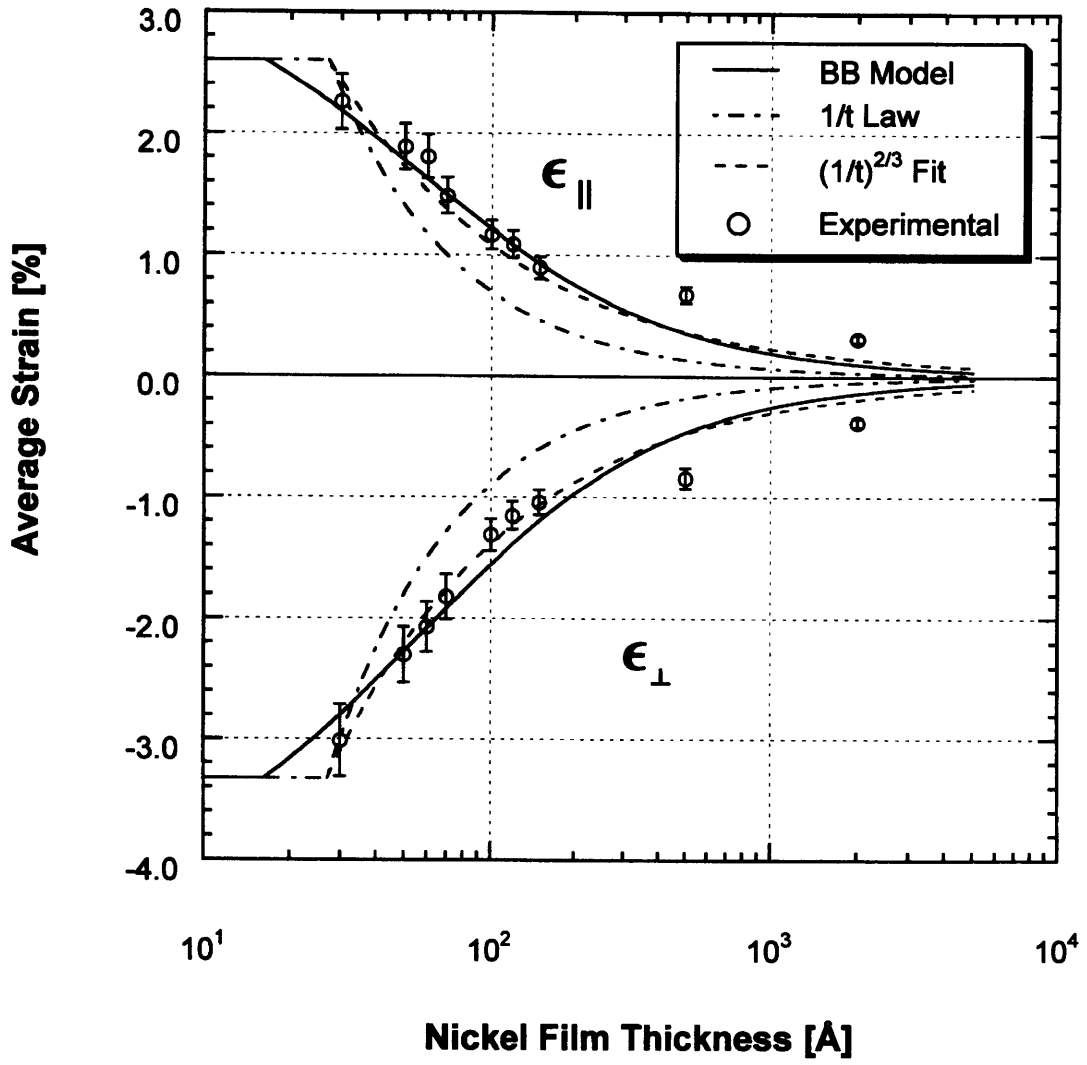

Figure 4.12: In-plane and out-of-plane strain as a function of the nickel film thickness. The data are fitted with three different models: the 1/t law, $(1/t)^{2/3}$, and Basson and Ball model.

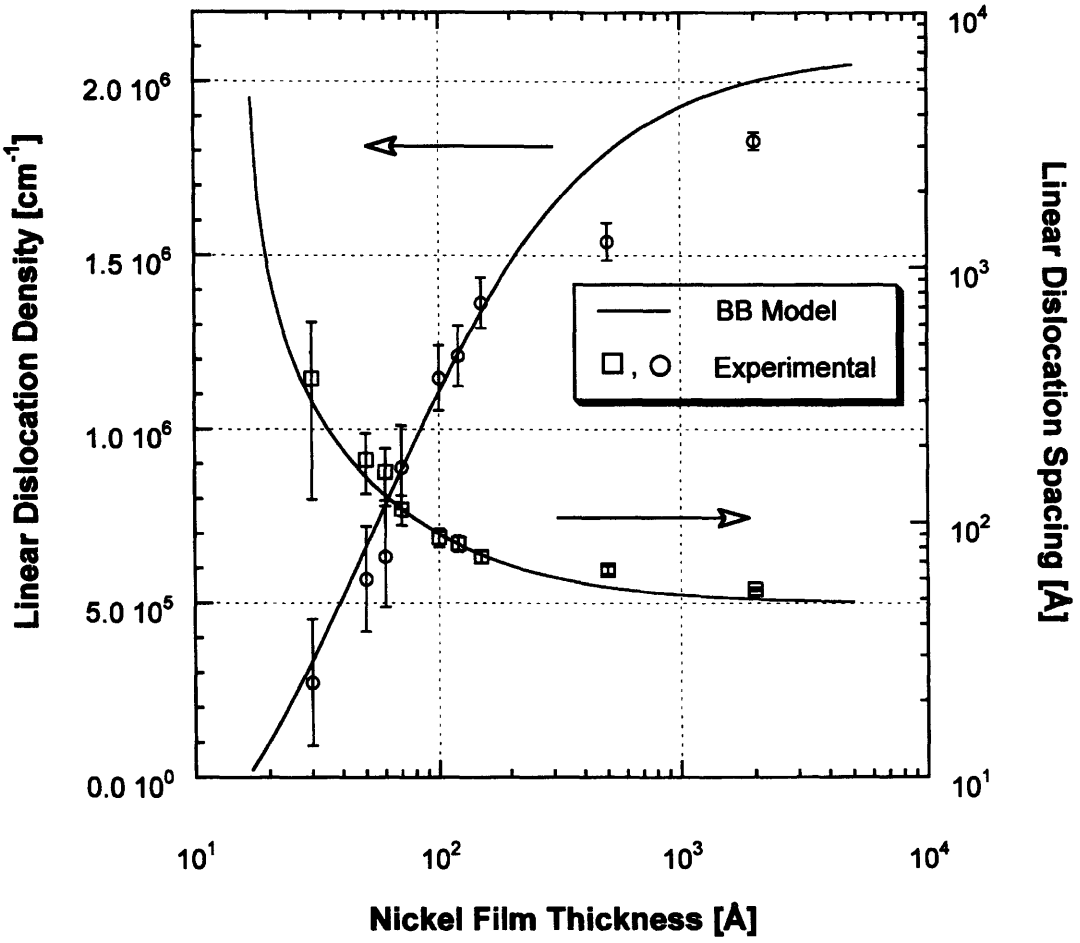

Figure 4.13: The solid line is the equilibrium linear density of dislocation. The dash line is the equilibrium dislocation spacing. These lines are derived from the Basson and Ball model. The discrete points are the data calculated from the diffraction peaks.

decrease approximately as $(1/t)^{2/3}$ rather than the often assumed $1/t$ form. The Basson and Ball model is used to account for the equilibrium strain of the nickel layer. The ratio of out-of-plane and in-plane strain agrees well with the bulk value of $-2c_{12}/c_{11}$. The strains in the thinner films can be accounted for using the BB model. The thicker films (500Å and 2000Å) deviate significantly from the equilibrium strain, which is in agreement with other workers.

Chapter 5

Magnetic Characterizations

Three magnetic characterization techniques are used to study the Cu/Ni/Cu/Si(001) films: vibrating sample magnetometer (VSM), torque magnetometer, and cantilever beam magnetostrictometer (CBM). Each technique gives unique and complementary information about the films. The results from the first two methods are shown here. The CBM results will be presented in chapter 7.

5.1 Vibrating Sample Magnetometer

The vibrating sample magnetometer (VSM) used for the present work is a commercial system designed by Digital Measurement System (which is now a division of AD Technologies). The sample is vibrated by a loudspeaker at about 70 cycles per second with an amplitude of about 0.1 mm near a set of stationary pickup coils (see figure 5.1). The magnetic field of the sample induces a voltage which is linearly proportional to the component of the sample moment in the direction normal to the plane of the detection coils. By measuring the output voltage (which is calibrated with a standard nickel disc), one component of the net moment can be determined. A "magnetization

versus magnetic field" curve (M-H loop) is obtained by varying the external magnetic field provided by the magnetic pole pieces of an electromagnet. Magnetic moment as low as 5×10^{-6} emu can be detected by the VSM.

For a detailed description of the working and design of a VSM, please consult the journal paper by Simon Foner [1959], or the general review article by Flanders and Graham [1993].

5.1.1 Experimental Results

Figure 5.2, 5.3, and 5.4 show the M-H loops of the Cu(50Å)/Ni(t_{Ni})/Cu(2000Å)/Si(001) films. Both the in-plane and out-of-plane loops were measured.[1] The in-plane curves were taken with the field applied in the nickel crystallographic [100] direction. Note that the nickel moments are normalized to unity in all the graphs. The thinner nickel films (17Å, 30Å, 50Å, 70Å, 80Å, and 100Å) exhibit quite square perpendicular hysteresis loops which indicate that their easy axes of magnetization are perpendicular to the film plane. The thicker nickel films (150Å, 500Å, and 2000Å) require much higher field to saturate the moment out-of-plane than in-plane, which suggests that their axes of magnetization lie in the film plane.

The saturation magnetization (M_s) is determined using the law of approach to saturation [McGuire and Flanders, 1969; p. 128; Cullity, 1972, p. 347; Chikazumi, 1997, p. 506]. The dependence of M_s on the nickel film thickness is shown in figure 5.5. The saturation magnetization decreases rapidly below 70Å. The dramatic reduction in M_s has been reported by Hope *et. al.* [1997] in their nickel films that are less than 100Å thick using polarized neutron reflection and alternating gradient magnetometer. They attributed the change in the magnetic moment to the change in strain in the

[1] In-plane M-H curve is taken by applying the external magnetic field in the film plane. Out-of-plane M-H curve is taken by applying the external magnetic field perpendicular to the film plane.

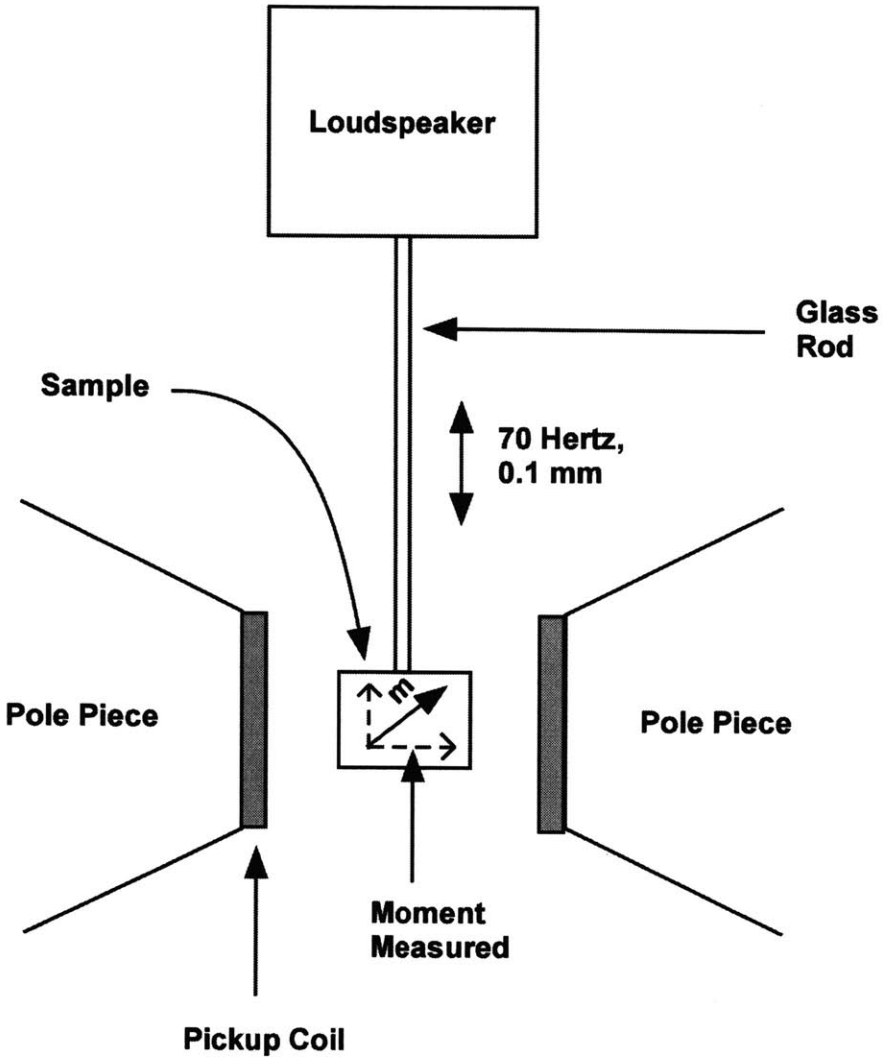

Figure 5.1: A schematic of the sample vibrating magnetometer.

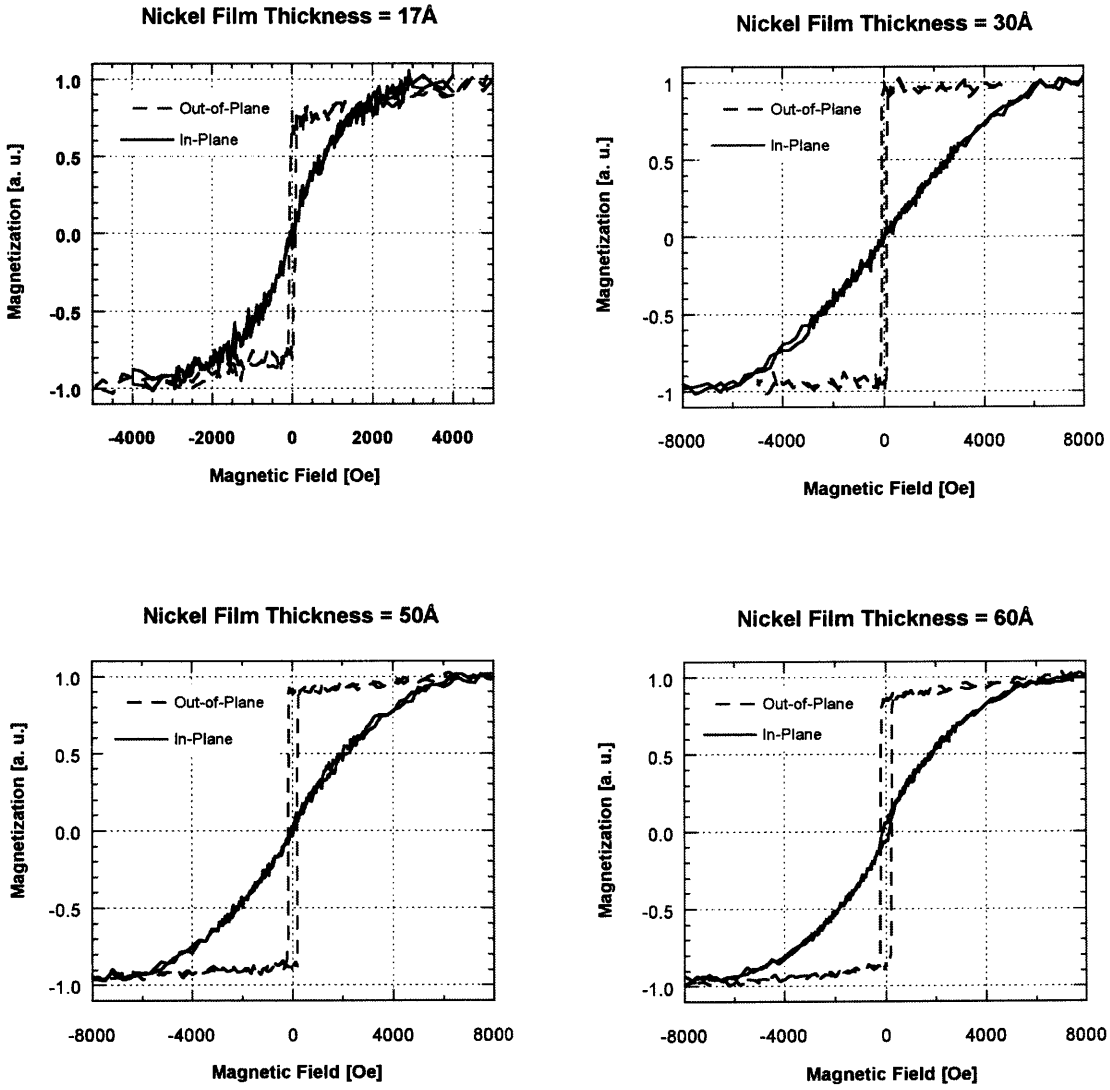

Figure 5.2: In-plane and out-of-plane M-H loops the Cu(50Å)/Ni(t_{Ni})/Cu(2000Å)/Si(001) films (t_{Ni} = 17Å, 30Å, 50Å, and 60Å). The in-plane loops are measured along the [100] crystallographic direction.

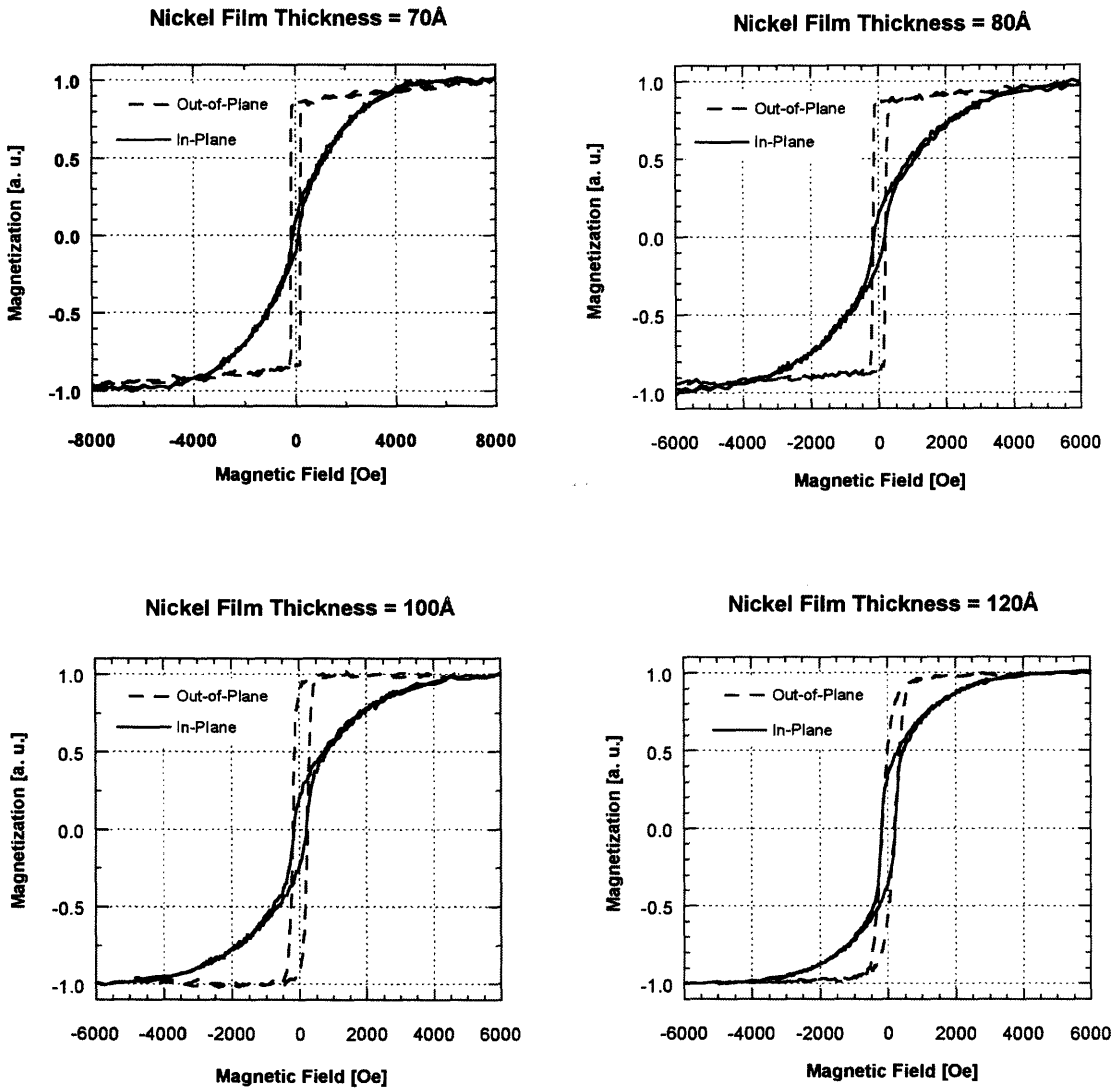

Figure 5.3: In-plane and out-of-plane M-H loops the Cu(50Å)/Ni(t_{Ni})/Cu(2000Å)/Si(001) films (t_{Ni} = 70Å, 80Å, 100Å, and 120Å). The in-plane loops are measured along the [100] crystallographic direction.

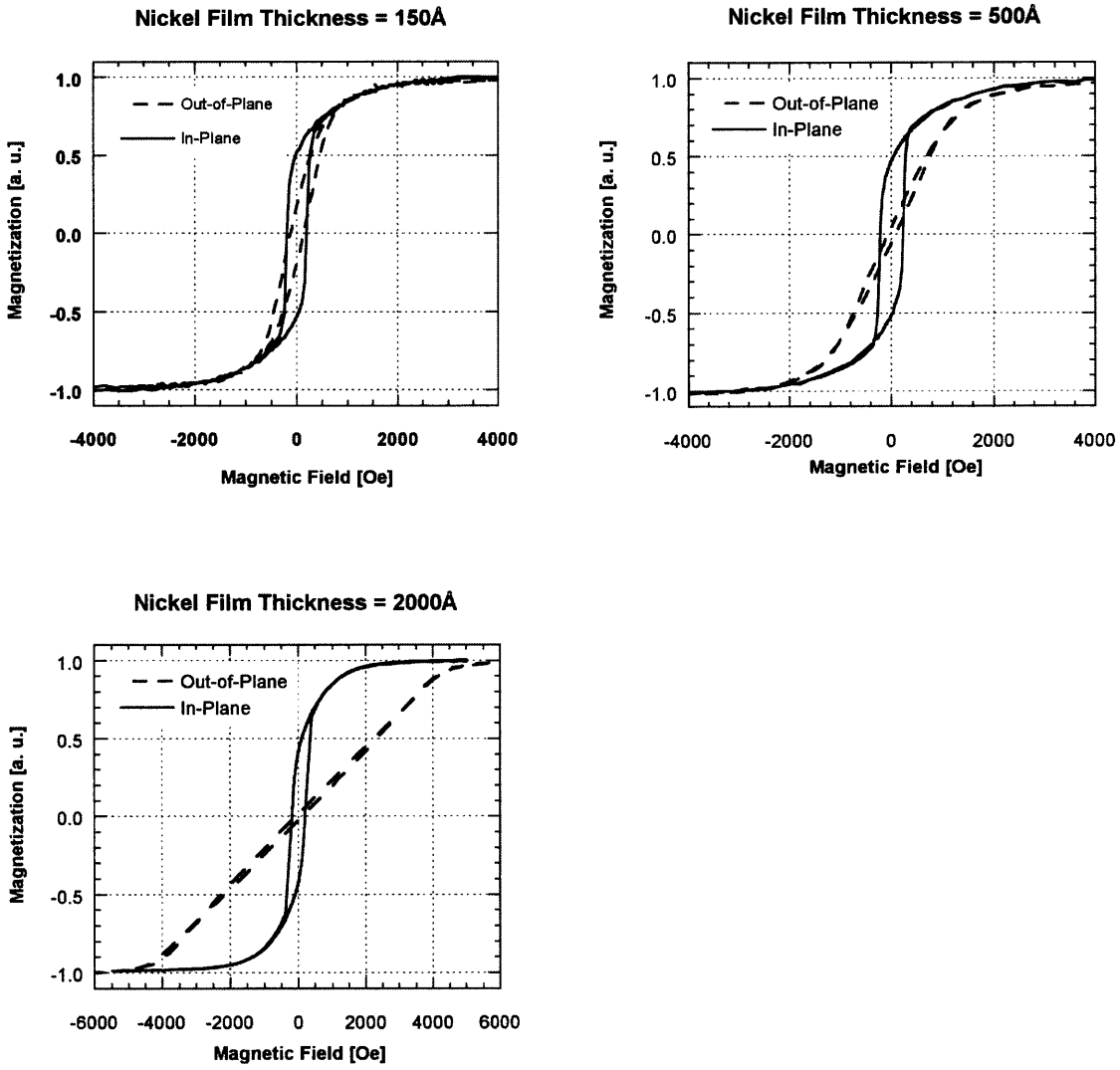

Figure 5.4: In-plane and out-of-plane M-H loops the Cu(Å)/Ni(t_{Ni})/Cu(2000Å)/Si(001) films (t_{Ni} = 150Å, 500Å, and 2000Å). The in-plane loops are measured along the [100] crystallographic direction.

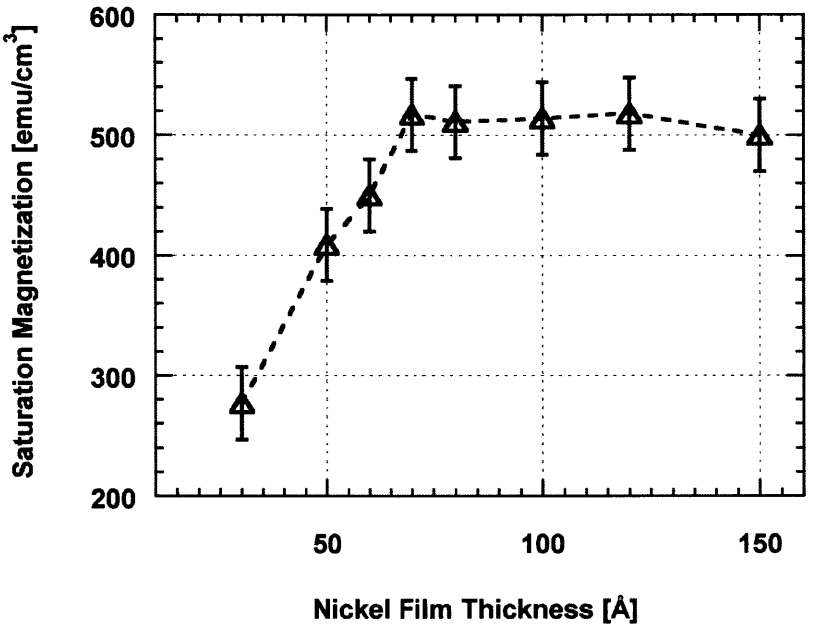

Figure 5.5: Saturation magnetization of the Cu(50Å)/Ni(t_{Ni})/Cu(2000Å)/Si(001) films are plotted as a function of the nickel film thickness. The values were determined from the VSM M-H loops using the law of approach to saturation.

nickel layer.

The squarenesses of both the in-plane and out-of-plane M-H loops (the fraction of the total moment remains in zero field) are plotted in figure 5.6. Their values are also tabulated in table 5.1. Observe that the perpendicular squareness is about 85% for the nickel films whose thicknesses are between 50Å to 100Å; that is, for these nickel films, about 85% of the total moment points out-of-plane. The perpendicular squareness decreases outside this thickness range. The in-plane squareness has a minimum at about 40Å, which seems to suggest that the magnetization is most out-of-plane at that film thickness.

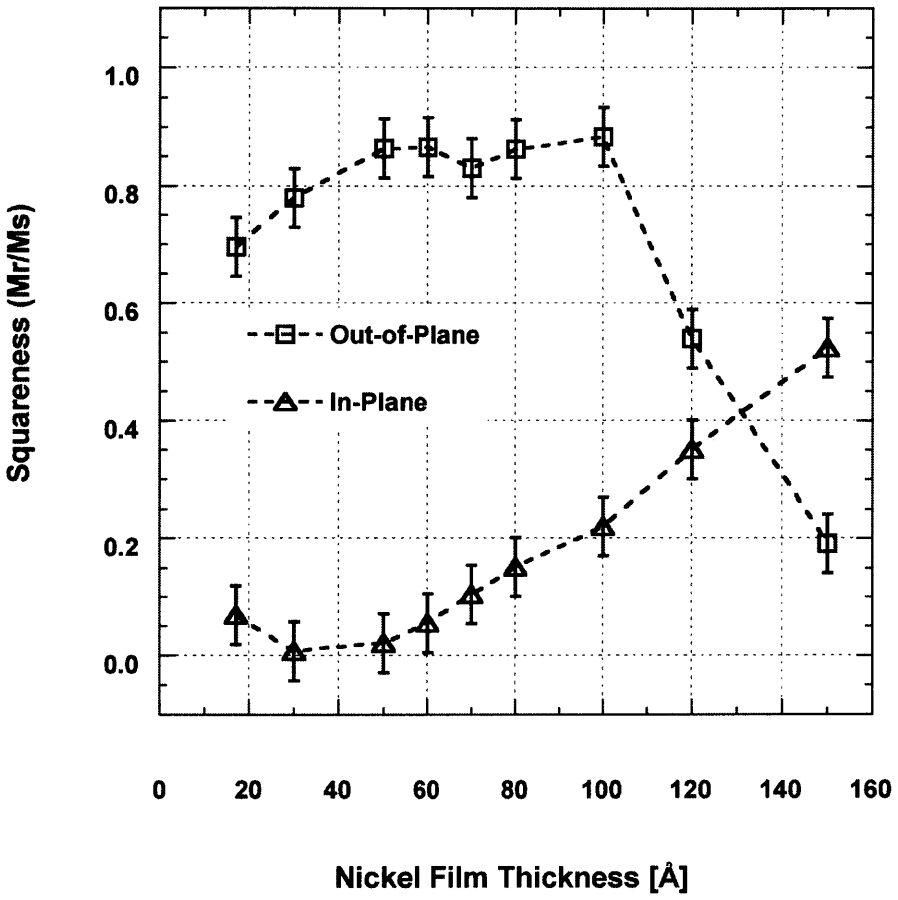

Figure 5.6: In-plane and out-of-plane squarenesses of the Cu(50Å)/Ni(t_{Ni})/Cu(2000Å)/Si(001) films are plotted as a function of the nickel film thickness. The squarenesses are calculated by taking the ratio of remanent and saturation magnetization.

Table 5.1: Squarenesses and coercivities (H_C) of Cu(50Å)/Ni(t_{Ni})/Cu(2000Å)/Si(001) films are tabulated. The values of both in-plane and out-of-plane loops are shown.

t_{Ni} [Å]	In-Plane		Out-of-Plane	
	Squareness [%]	H_C [Oe]	Squareness [%]	H_C [Oe]
17	7	0	70	67
30	1	0	78	115
50	2	0	86	181
60	6	115	87	219
70	10	114	83	191
80	15	153	86	193
100	22	186	88	218
120	35	202	54	182
150	52	200	19	126
500	48	186	5	70
2000	42	190	1	90

Table 5.1 also lists the coercivities (the magnetic field needed to bring the magnetic induction of the sample to zero) for the in-plane and out-of-plane M-H loops. Although the coercivities will not be analyzed in this thesis work, they are included for completeness. The behavior of the coercivity can be studied using a micromagnetic theory (such as that by Bertram and Paul [1997]) to extract information about the Néel interface anisotropy of the system.

5.1.2 Effective Magnetic Anisotropy

Although the squareness captures the trend for perpendicular magnetization, it does not give insight into the driving forces that are responsible for the behavior. A more instructive quantity (the one that is used widely in the literature) is the effective magnetic anisotropy, K^{eff}, which is defined as the difference in the free energy when the system is magnetized in-plane and out-of-plane. More compactly,

$$K^{eff} = F(\text{in-plane}) - F(\text{out-of-plane}) \tag{5.1}$$

where F is the free energy of the system. Note that K^{eff} is defined using the convention that if it is positive, the magnetization prefers to be out-of-plane.

Effective magnetic anisotropy can be found experimentally from the M-H loops [Purcell *et. al.*, 1992; Jungblut *et. al*, 1994; Bochi, 1995, p. 31]. The procedure is the following: Find the anhysteretic (without hysteresis) curve by taking the average of the magnetic field of the forward and backward M-H curves for each value of the magnetization (see figure 5.7a). Integrate the anhysteretic curve with respect to the magnetization to get the work needed to magnetize the sample (see figure 5.7b). Because free energy is equal to the magnetic work provided that other thermodynamics variables (such as temperature and pressure) remain unchanged during the

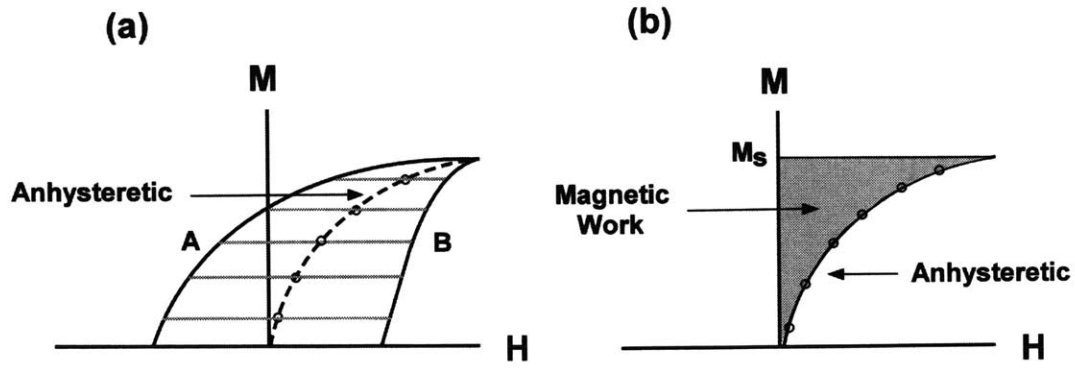

Figure 5.7: (a) illustrates a way of finding an anhysteretic curve: draw a line (AB) that intersect the forward and reverse M-H curves; the midpoint of the line AB is a point on the anhysteretic curve. Repeat the process to find other points on the anhysteretic curve. (b) shows the magnetic work needed to magnetize the sample, which is the area under the anhysteretic curve.

magnetization process [Carr, 1969, p. 53], the difference between the work needed to magnetized the sample in-plane and out-of-plane is a measure of K^{eff}.

Figure 5.8 is a plot the thickness-weighed effective magnetic anisotropy energy ($K^{eff}t$) versus the nickel film thickness. The results from the M-H loop and torque methods are shown. Their values are tabulated in table 5.2. The torque method will be discussed in the next section. The two results agree with each other within the experimental error. The VSM result suggests that the window of perpendicular magnetization spans from 15 to about 140Å. The exact energy terms in the effective anisotropy will be discussed in the next chapter.

There are many disadvantages with the M-H loops method of finding K^{eff}. One is due to the complication of the hysteretic nature of M-H loops. By using the anhysteretic curve, we have ignored the nonequilibrium behavior of the M-H loop with a reversible constitutive relation [Bertotti, 1998, p. 115]. Another disadvantage is that only one data point is obtained for each set (in-plane and out-of-plane) of M-H

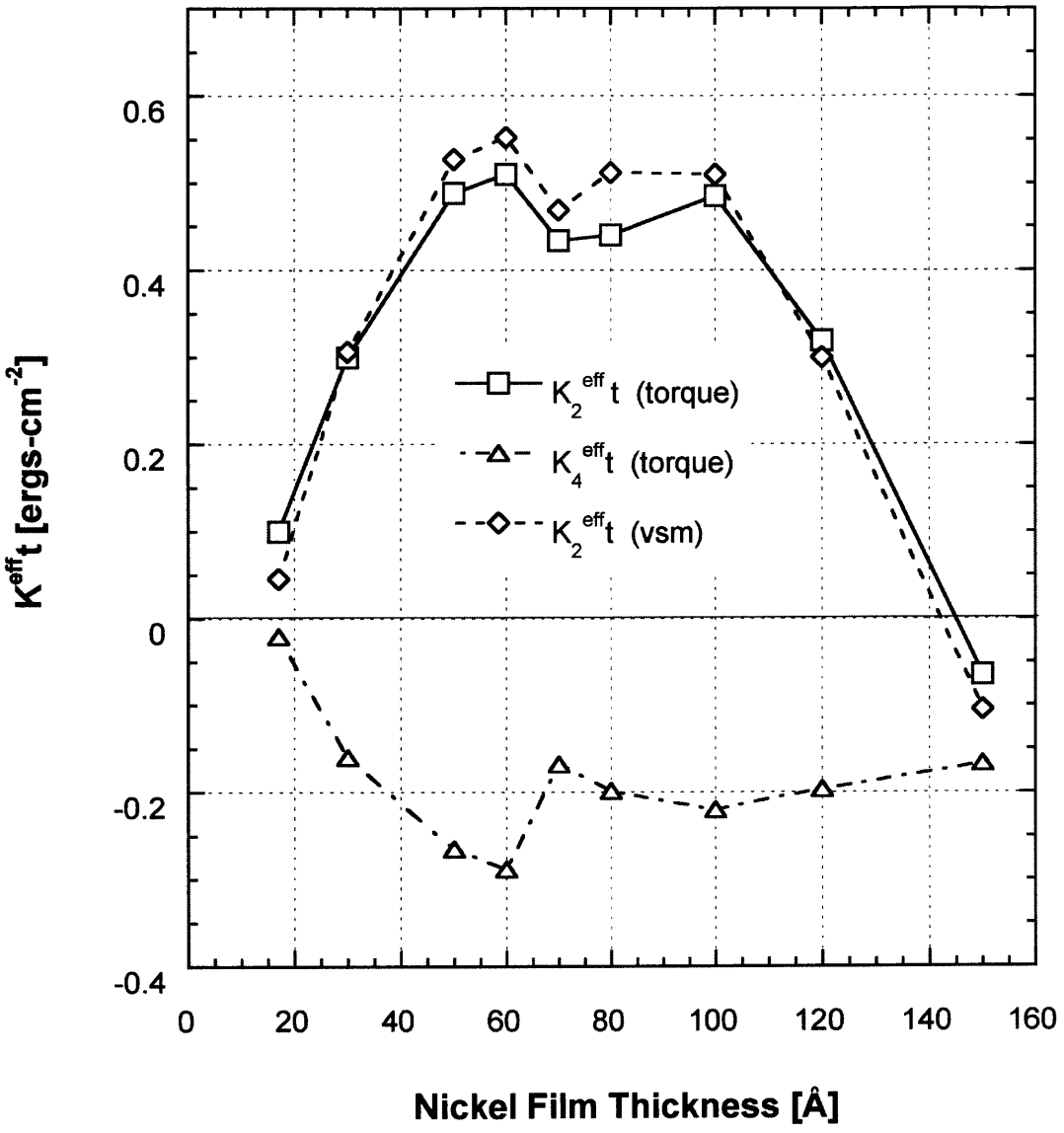

Figure 5.8: Thickness-weighed magnetic anisotropy energy of Cu(50Å)/Ni(t_{Ni})/Cu(2000Å)/Si(001) films is plotted with the nickel film thickness. The second-order angular coefficients is found using the torque method and M-H loops from VSM. The fourth-order angular coefficient is found using the torque method. The experimental error for all the anisotropy data is about $\pm$ 0.05 ergs/cm^2.

Table 5.2: Values of the thickness-weighed effective magnetic anisotropy of Cu(50Å)/Ni(t_{Ni})/Cu(2000Å)/Si(001) films as a function of the nickel film thickness are tabulated. Both the second- and fourth- order angular coefficients are shown. The 2220Å film is the only film that has no copper cap layer.

t_{Ni} [Å]	$K_2^{eff}[10^6 \frac{ergs}{cm^3}]$		$K_4^{eff}[10^6 \frac{ergs}{cm^3}]$	$K_2^{eff}t[\frac{ergs}{cm^2}]$		$K_4^{eff}t[\frac{ergs}{cm^2}]$
	VSM	Torque	Torque	VSM	Torque	Torque
17	0.27	0.586	-0.12	0.046	0.10	-0.02
30	1.02	1.00	-0.53	0.306	0.30	-0.16
50	1.05	0.976	-0.53	0.527	0.49	-0.26
60	0.92	0.850	-0.48	0.552	0.51	-0.29
70	0.67	0.620	-0.24	0.469	0.43	-0.17
80	0.64	0.550	-0.25	0.512	0.44	-0.20
100	0.51	0.485	-0.22	0.510	0.48	-0.22
120	0.25	0.266	-0.16	0.300	0.32	-0.20
150	-0.07	-0.042	-0.11	-0.105	-0.06	-0.17
2220*		-1.090	-0.45		-24.20	-10.03

loops. In contrast, the torque method determines the magnetic anisotropy by taking many data points for each measurement.

5.2 Torque Magnetometer

Torque magnetometer is the most accurate means for measuring magnetic anisotropy [Chikazumi, 1997, p. 256]. The method is based on the following principle: Because it takes energy to rotate the magnetization from an easy axis by an external field, there is a tendency for the sample to rotate in such a way that the easy axis is aligned with the external field. The torque that the sample experiences is a measure of its magnetic anisotropy. A torque magnetometer measures the torque as a function of the angle of rotation from an easy direction.

A DMS (Digital Measurement System) torque magnetometer was used for the present work. A schematic diagram of the system is shown in figure 5.9. The sample was rotated in a uniform magnetic field about the [010] crystallographic direction (see figure 5.9). A 1.3 Tesla field was used to ensure that the sample was fully saturated. The nickel (001) planes were first aligned parallel to the external magnetic field. The torque was measured for the sample in various orientation relative to the field.

The interpretation of the torque data depend on the free energy expression that is used in the analyses. Because the nickel is tetragonally distorted, the following free energy density is used [O'Handley *et. al.*, 1993]:

$$F = -K_2^{eff}\cos^2\theta + K_4^{eff}\sin^2\theta\cos^2\theta \tag{5.2}$$

where θ is the angle between the magnetization and the film normal. K_2^{eff} is the coefficient of the second-order angular term, which includes the Néel interface, magnetostatic, and magnetoelastic (both first- and second- order in strain) anisotropy

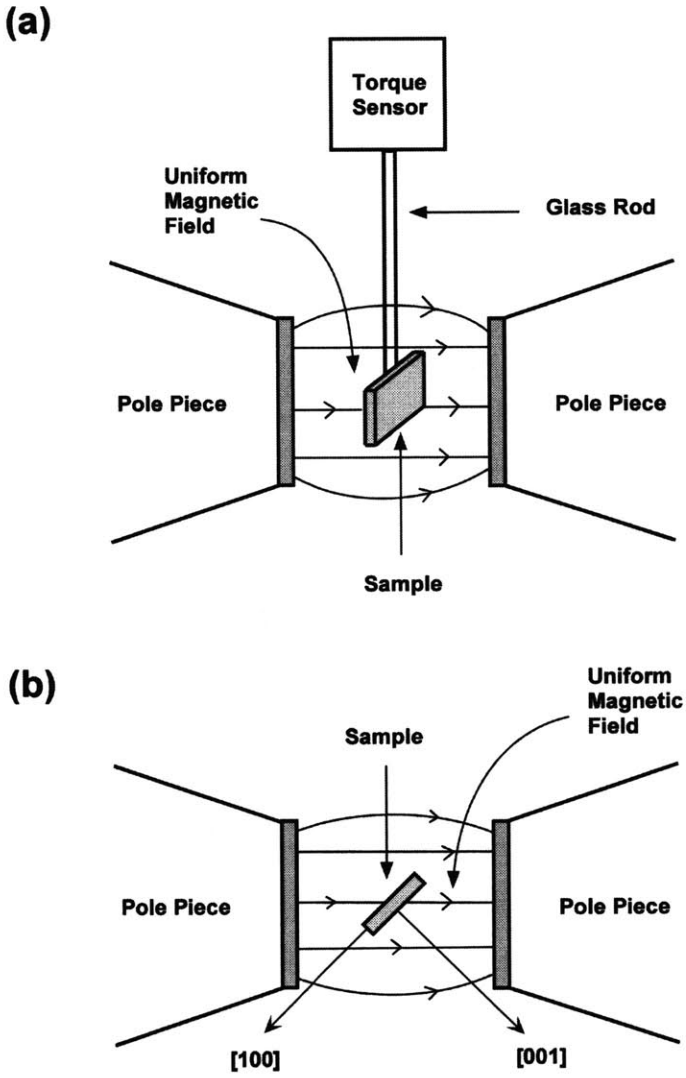

Figure 5.9: A schematic diagram of the torque magnetometer. a) a side view; b) a top view. [001] and [100] are the crystallographic directions of the nickel layer.

energies. K_4^{eff} is the coefficient of the fourth-order angular term of the anisotropy. Note that if K_2^{eff} is positive, the second-order term favors out-of-plane. If K_4^{eff} is negative, the fourth-order term favors magnetization at a 45° from the film plane. In writing Eq. 5.2, we have assumed the magnetic moment has no component in the [010] direction, as it is the case here.

The torque on the sample per unit volume can then be found as follows [Cullity, 1972, p. 216; Chikazumi, 1997, p. 258]:

$$L = -\frac{dF}{d\theta} = -K_2^{eff}\sin 2\theta - \frac{K_4^{eff}}{2}\sin 4\theta. \tag{5.3}$$

Eq. 5.3 will be used to analyze the torque data which are now presented.

5.2.1 Experimental Results

Figure 5.10, 5.11, and 5.12 are the torque curves for the nickel films. The angles at zero torque correspond to the easy or hard axes of magnetization. The peaks in the torque curves correspond to the inflection points in the anisotropy energy. Note that all the torque curves start at $\theta = 90°$. This is a consequence of the fact that the measurements started with the nickel film planes parallel to the external field.

Observe that for the nickel films that are less than 150Å, the torque becomes negative as θ passes 90°, and it decreases with a small increase in θ. This behavior is expected from a film that exhibits perpendicular magnetization; any small deviation from the normal direction would result in a torque that tends to *restore* the alignment of the magnetization to be in the film normal direction. On the other hand, the torque is negative for $\theta = 90°$ in the 2220Å film, and it decreases with a small increase in θ. This behavior is a signature of a sample that favors an in-plane magnetization.

The experimental data are fitted with the following expression:

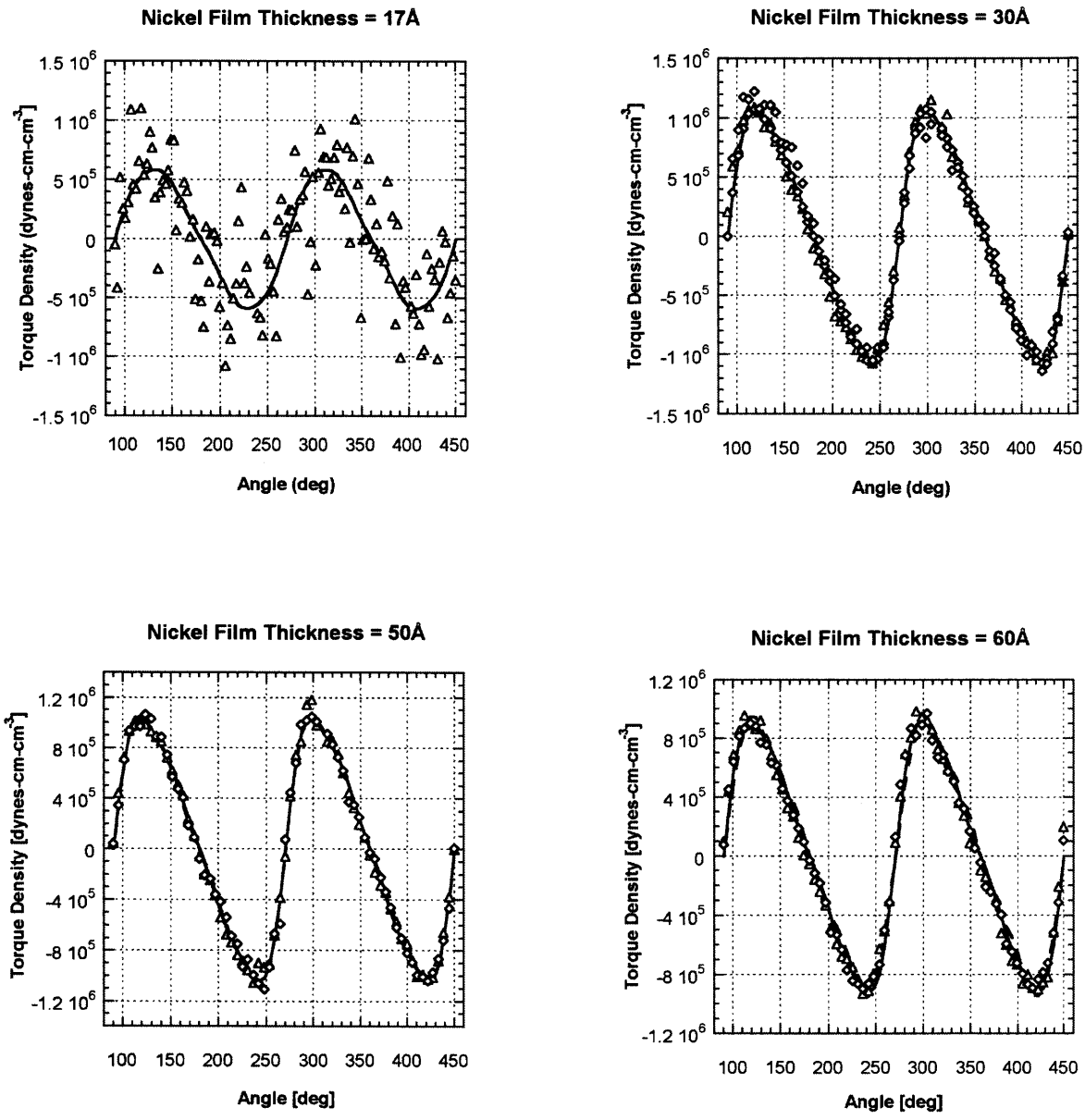

Figure 5.10: Torque density of Cu(50Å)/Ni(t_{Ni})/Cu(2000Å)/Si(001) films (t_{Ni} = 17Å, 30Å, 50Å, and 60Å) are plotted as a function of the angle between the magnetization and the films normal. The triangles and diamonds represent the experimental data points for the clockwise and counter-clockwise rotations, respectively. The solid lines are the fitting curves.

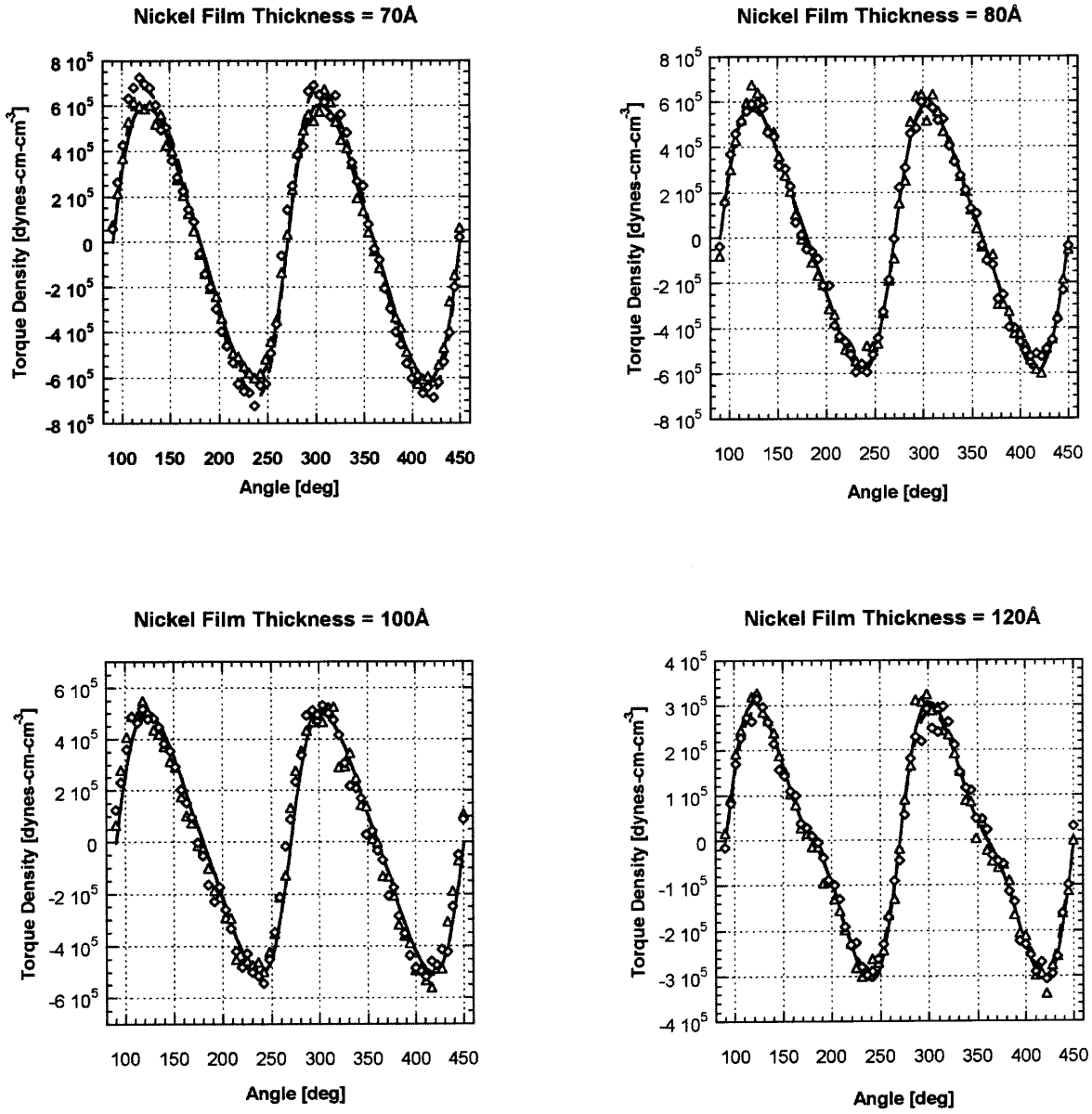

Figure 5.11: Torque density of Cu(50Å)/Ni(t_{Ni})/Cu(2000Å)/Si(001) films (t_{Ni} = 70Å, 80Å, 100Å, and 120Å) are plotted as a function of the angle between the magnetization and the films normal. The triangles and diamonds represent the experimental data points for the clockwise and counter-clockwise rotations, respectively. The solid lines are the fitting curves.

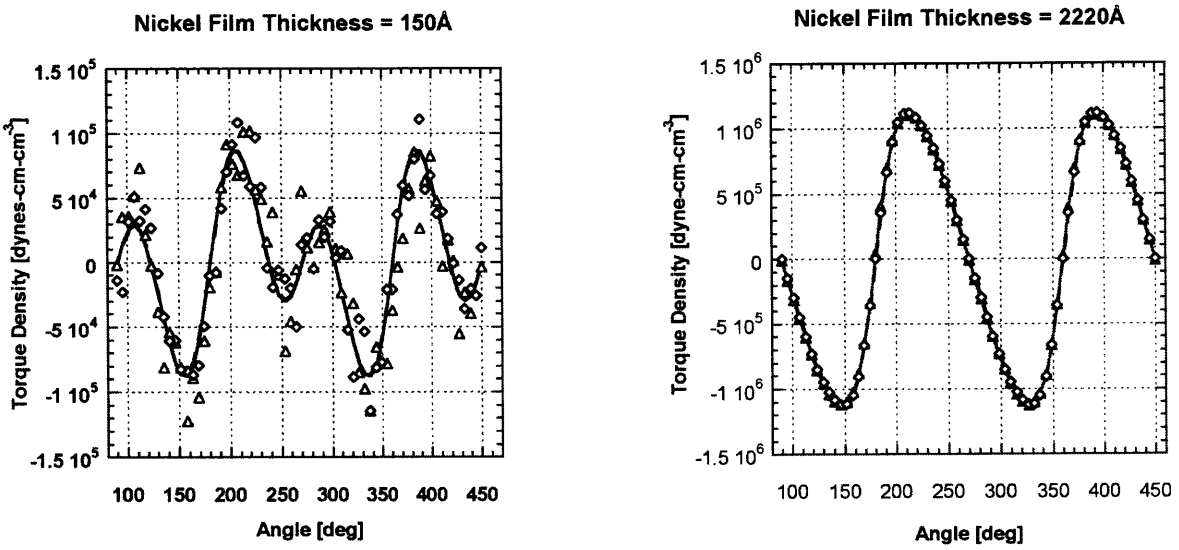

Figure 5.12: Torque density of Cu(50Å)/Ni(150Å)/Cu(2000Å)/Si(001) and Ni(2220Å)/Cu(2000Å)/Si(001) films are plotted as a function of the angle between the magnetization and the films normal. The triangles and diamonds represent the experimental data points for the clockwise and counter-clockwise rotations, respectively. The solid lines are the fitting curves.

$$L = -K_2^{eff}\sin 2\theta - \frac{K_4^{eff}}{2}\sin 4\theta + K_6^{eff}\sin 6\theta + K_8^{eff}\sin 8\theta. \tag{5.4}$$

The higher order terms are included to assess their contributions to the anisotropy. Their coefficients are found to be about one order of magnitude smaller than K_2^{eff} and K_4^{eff} in all of our samples (except the 17Å film in which experimental error could be the factor for the reading).

The results of the fitting are tabulated in table 5.2. The second- and fourth-order thickness-weighed effective anisotropy terms are also plotted in figure 5.13. The results from Bochi *et. al.* [1995] and Jungblut *et. al.* [1994] are also included for comparison.

The three sets of effective anisotropy data describe essentially the same effect:

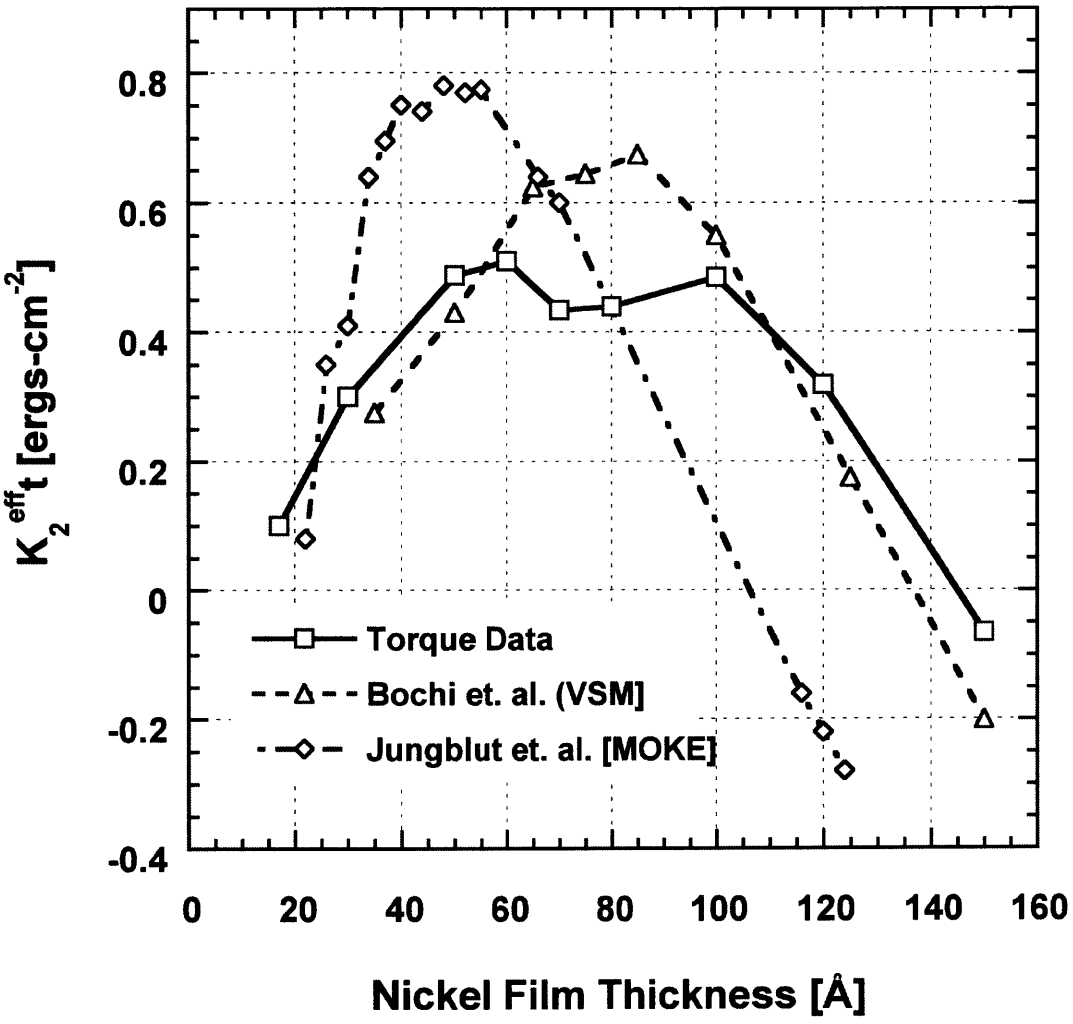

Figure 5.13: Thickness-weighed magnetic anisotropy energy of Cu/Ni/Cu films is plotted with the nickel film thickness. The torque data are experimental data from the torque magnetometer. The diamonds are the data estimated from Jungblut *et. al.* [1994]. The triangles are the data estimated from Bochi's Ph. D. thesis [1995].

the thickness-weighed effective anisotropy, K_2^{eff} is positive over a remarkably broad nickel thickness range. Further, there is a tendency for the magnetization to go back in-plane as the nickel film thickness decreases. However, the width and peak in each anisotropy curve are slightly different among the three sets of data. This may be due to the differences in sample preparations, and thus may result in differences in the strain state in the nickel layers.

5.2.2 Single-Domain Spin Phase Diagram

With only the second-order angular term in the magnetic anisotropy, the magnetization can point either in-plane or out-of-plane in a single-domain system (that is, the magnetization is uniform throughout the sample). The addition of the fourth-order angular term introduces many more possible single-domain equilibrium states, which are determined by the relative magnitudes and signs of the coefficients (K_2^{eff} and K_4^{eff}).

Figure 5.14 shows the single-domain spin phase diagram of a system that has fourth-order magnetic anisotropy. The phase diagram is a graph showing the different magnetic states in the space spanned by K_2^{eff} and K_4^{eff}. The boundaries of the different magnetic "phases" are determined either by the condition that -1 $\leq \cos 2\theta \leq$ 1, or that the second derivative of the free energy with respect to θ must be positive (namely, the extremum is a minimum). The global stability of a critical angle θ (at which the magnetization is at least locally stable) can be determined by graphically as shown in figure 5.15.

The experimental data are also plotted on the phase diagram (figure 5.14). Note that the anisotropies of all the nickel films that are less than 150Å fall in region I. Thus, their equilibrium direction of magnetization is out of the film plane in agreement with the VSM results. The anisotropy of the 150Å nickel film is in region II which

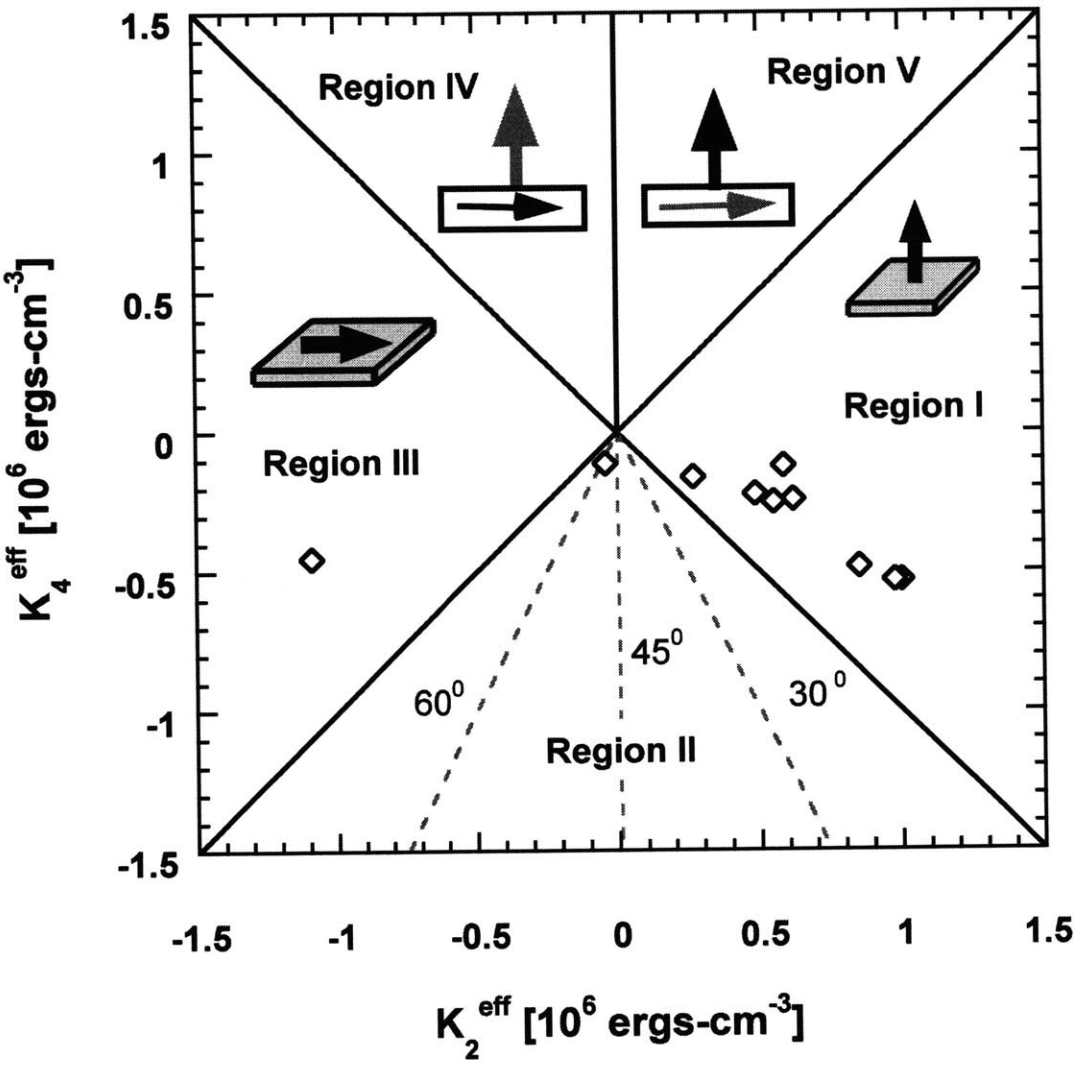

Figure 5.14: Single-domain spin phase diagram of a system that has fourth-order magnetic anisotropy. The magnetic state of each region is illustrated graphically in figure 5.15. The dashed lines in Region II are the contour lines for the different canting angles. The diamonds are the experimental data for the Cu/Ni/Cu/Si(001) films of the present work.

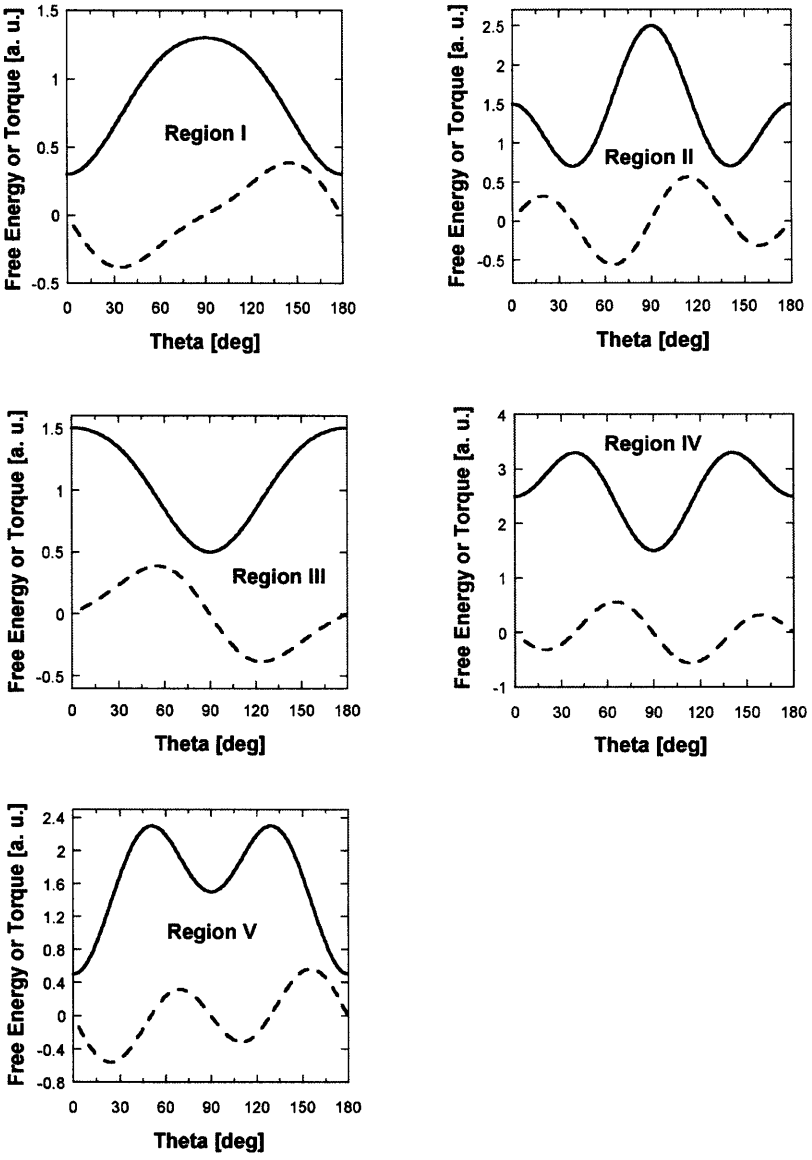

Figure 5.15: Simulations of a free energy (solid lines) and its torque curve (dash lines) for each of the five regions of the single-domain spin phase diagram. The angle θ is measured with respect to the film normal. All the free energy curves are displaced vertically by arbitrary amounts. The torque curves are amplified by an arbitrary factor for visibility reason. Region I: the equilibrium magnetization is out-of-plane. Region II: the equilibrium magnetization is canted at an angle with respect to the film normal. Region III: the equilibrium magnetization is in-plane. Region IV: the equilibrium magnetization can be in-plane or out-of-plane. The out-of-plane state is metastable. Region V: the equilibrium magnetization can be in-plane or out-of-plane. The in-plane state is metastable.

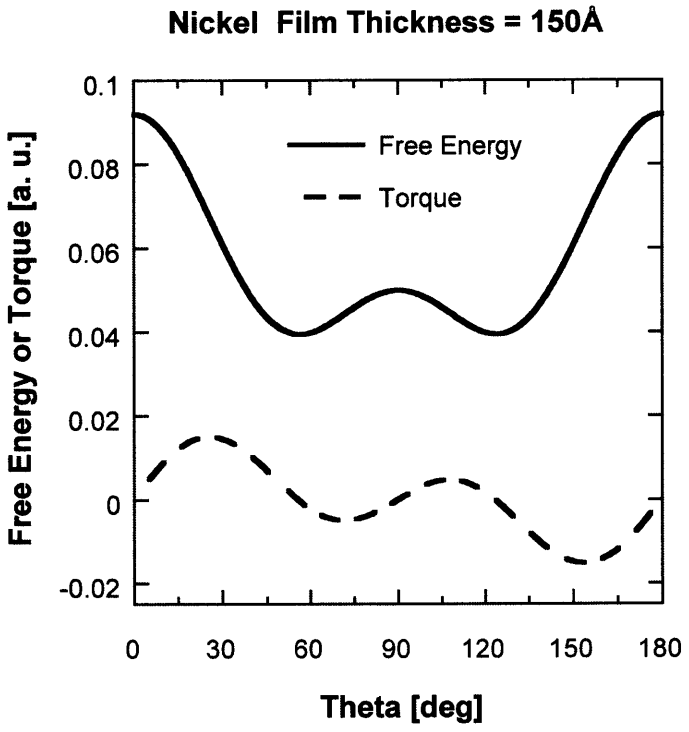

Figure 5.16: The free energy (solid line) and torque curve (dash line) of the Cu(50Å)/Ni(150Å)/Cu(2000Å)/Si(001) film are shown. The free energy curve is shifted by an arbitrary constant. The torque curve is amplified by a factor of ten for visibility reason.

suggests that its direction of the magnetization is canted at an angle with respect to the film normal. The value of the angle (θ_{eq}) is calculated to be 56° from the film normal using the following formula:

$$\cos(2\theta_{eq}) = -\frac{K_2^{eff}}{K_4^{eff}} \tag{5.5}$$

The free energy and torque of the 150Å film are also shown in figure 5.16. The free energy is lowest for $\theta_{eq} = 56°$ in agreement with the calculation.

The evolution of the anisotropy with nickel film thickness is clear from the torque

data. For the thinner nickel film, the direction of magnetization is dominated by the second-order angular term which favors perpendicular magnetization. As the nickel film approaches 150Å thick, the second-order term becomes negligible, and the presence of the-order angular term (which favors a canting magnetization state) is more felt. The anisotropy of the 2220Å film stay well inside region III due to the strongly negative value of K_2^{eff}.

The canting state of the magnetization has been reported by Farle *et. al.* [1997] in a 6.7 monolayer Ni(001)/Cu(001) film using ferromagnetic resonance technique. Stamps *et. al.* [1997] has also reported the existence of canting states in epitaxial Co/Pt multilayers.

5.3 Summary

Both the VSM and torque data show that the easy magnetization axis of the nickel is out of the plane over a wide range of nickel film thickness. The effective fourth order angular anisotropy term (K_4^{eff}) is also determined. The torque analysis suggests that the magnetization of the 150Å nickel film is canted at about 56° away from the film normal.

Chapter 6

Anisotropy Analyses by Spin-Pair Model

In this chapter, the magnetic anisotropy of the Cu/Ni/Cu(001) system is analyzed using the spin-pair model developed in chapter 2. The structural and magnetic information presented in chapter 3, 4, and 5 are used for a quantitative assessment of individual energy contribution to the total magnetic anisotropy. Only the second-order angular effective anisotropy (K_2^{eff}) is examined for this thesis work.

6.1 Effective Magnetic Anisotropy

The effective magnetic anisotropy has been defined by Eq. 5.1 which says that it is the difference in the free energy when the magnetization is in-plane and out-of-plane. The free energy of the system is modeled to consist of the intrinsic magnetic anisotropy energy (Eq. 2.22) and magnetostatic energy. For all practical purposes, we can assume the magnetostatic energy to be zero when the magnetization is in-plane and is $2\pi M_s^2$ when the magnetization is out-of-plane. Thus,

$$K_2^{eff} = E_{film}(\alpha_1 = 1) - E_{film}(\alpha_3 = 1) - 2\pi M_s^2 \tag{6.1}$$

Using Eq. 2.22, the thickness-weighed effective magnetic anisotropy can be written as follows:

$$\begin{aligned} K_2^{eff}t &= -(K_s^{eff} + D_{rs}^{eff} + 2\pi M_s^2)t \\ &= 2(K_N + B_{rs}^I e_0 + A_{rs}^I e_0^2) - (B_{rs}^b + A_{rs}^b e_0)e_0 t - 2\pi M_s^2 t \end{aligned} \tag{6.2}$$

Note that in writing the above equation for the effective anisotropy, we have kept only the residual strain terms. The reason is that the magnetostrictive strains (10^{-5}) are typically orders of magnitude smaller than the residual strains (which can be as large as 2.6%, as discussed in chapter 3).

Eq. 6.2 can be used to analyze the experimental data obtained by M-H loops or torque curves. The study will give quantitative information about the contribution of each energy term to the total anisotropy.

6.2 First-Order Spin-Pair Model

It is instructive to see how much the SP model can explain the magnetic anisotropy of the Cu/Ni/Cu(001) films with only the first-order ME terms. Without the second-order terms, the effective anisotropy (Eq. 6.2) simplifies to

$$K_2^{eff}t = 2(K_N + B_{rs}^I e_0) - B_{rs}^b e_0 t - 2\pi M_s^2 t \tag{6.3}$$

One good thing about the first-order theory is that all the linear ME coefficients (including the nickel/vacuum Néel interface term) can be calculated from the two

Table 6.1: Linear coefficients are calculated using the first-order SP model. The input parameters for the model are: $B_1 = 6.2 \times 10^7$ ergs/cm^3, $B_2 = 8.6 \times 10^7$ ergs/cm^3, a_o = 3.5241Å, and $2c_{12}/c_{11} = 1.28$.

10^7 ergs/cm^3			ergs/cm^2						
$\rho L(\frac{a_o}{\sqrt{2}})$	$\rho\frac{dL(\frac{a_o}{\sqrt{2}})}{dr}\frac{a_o}{\sqrt{2}}$	B^b_{rs}	B^I_{11}	B^I_{12}	B^I_{13}	B^I_{21}	B^I_{22}	B^I_{rs}	K^v_N
2.02	0.250	-14.14	0.36	0.55	0.17	0.36	0.20	-1.22	0.18

known bulk values (B_1 and B_2) using the relations tabulated in table 2.1. The results are summarized in table 6.1.

Figure 6.1 shows a graph of the $K_2^{eff}t$ curve predicted by the first-order magnetoelastic model. Three sets of experimental data are also shown for comparisons. The in-plane residual strain e_0 is approximated by the power law expression

$$e_0 = \eta(27/t)^{2/3} \tag{6.4}$$

as discussed in chapter 4. The Néel interface term is assumed to be close to that of a nickel/vacuum interface; that is, $K_N \approx K_N^v$. The magnetostatic energy is taken to be $1.5 \times 10^6 ergs/cm^3$, which is the bulk value for nickel at room temperature.

It is worth to emphasize that there are no fitting parameters in the first-order model. All the values are calculated using the two well-known bulk magnetoelastic constants of nickel, namely B_1 and B_2.

As expected, the first-order model gives better prediction for the thicker films. There, the nickel layers are less strained. For the thinner films, higher order strain effects become more important. Thus, larger deviation from the experimental curve is expected. The peak in the first-order curve occurs at the critical thickness t_c below which the nickel is coherent with the copper buffered layer.

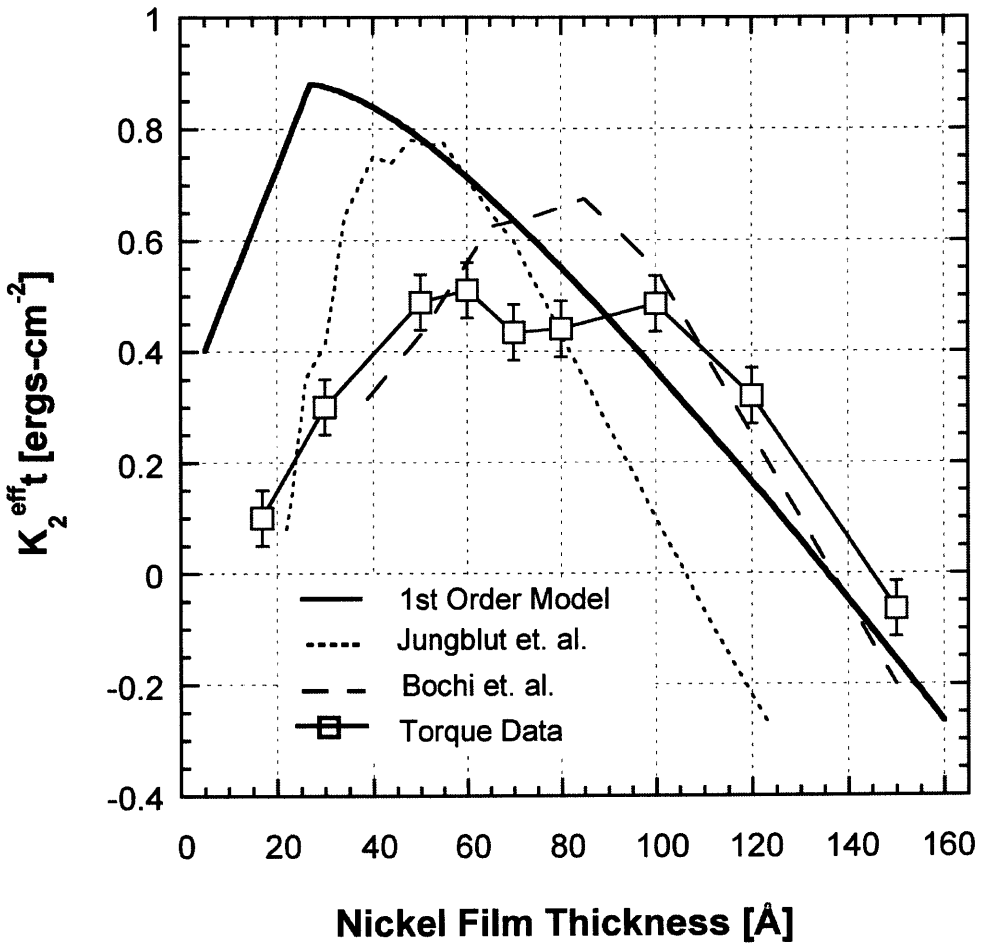

Figure 6.1: Thickness-weighed effective anisotropy of the Cu/Ni/Cu/Si(001) films as predicted by the first-order SP model. Three sets of experimental data are also shown for comparisons.

Figure 6.2 shows the contribution of each energy term in percentage to the total second-order angular magnetic anisotropy. The percentage is calculated by dividing each energy term to the sum of all the individual energy terms in K_2^{eff} at their absolute values. The sign of the contribution is to denote whether the energy term favors in-plane or out-of-plane magnetization (positive for out-of-plane, and negative for in-plane).

Both the Néel interface term and first-order bulk ME term favor perpendicular magnetization. The contribution of the Néel interface term increases with decreasing film thickness due to the increase in the interface-to-volume ratio. Although the first-order bulk ME term increases with decreasing film thickness due to the increase in the strain in the nickel, its contribution decreases in percentage due to the domination of the Néel interface anisotropy.

The first-order interface ME term and magnetostatic energy favor in-plane magnetization. The contribution of the first-order interface ME term increases with decreasing nickel film thickness due to a combination of two factors: the increase in strain in the nickel film and the increase in the interface-to-volume ratio. The contribution from the magnetostatic energy decreases with film thickness because of volume effect.

Although the first-order model has some success in predicting the effective magnetic anisotropy for the thicker nickel films, it has problems in explaining it for the thinner nickel films. In particular, the peak in the predicted $K_2^{eff}t$ curve happens at the critical thickness t_c which is less than 27Å (as discussed in chapter 4), whereas the experimental curve peaks above 60Å.

In the Jungblut's picture, the peak in the K_2^{eff} is forced to correspond to the critical thickness t_c, which would be at around 80Å for the torque data. This conclusion is inconsistent with the x-ray diffraction study discussed in chapter 4. By allowing the second-order ME terms to contribute to the magnetic anisotropy, the

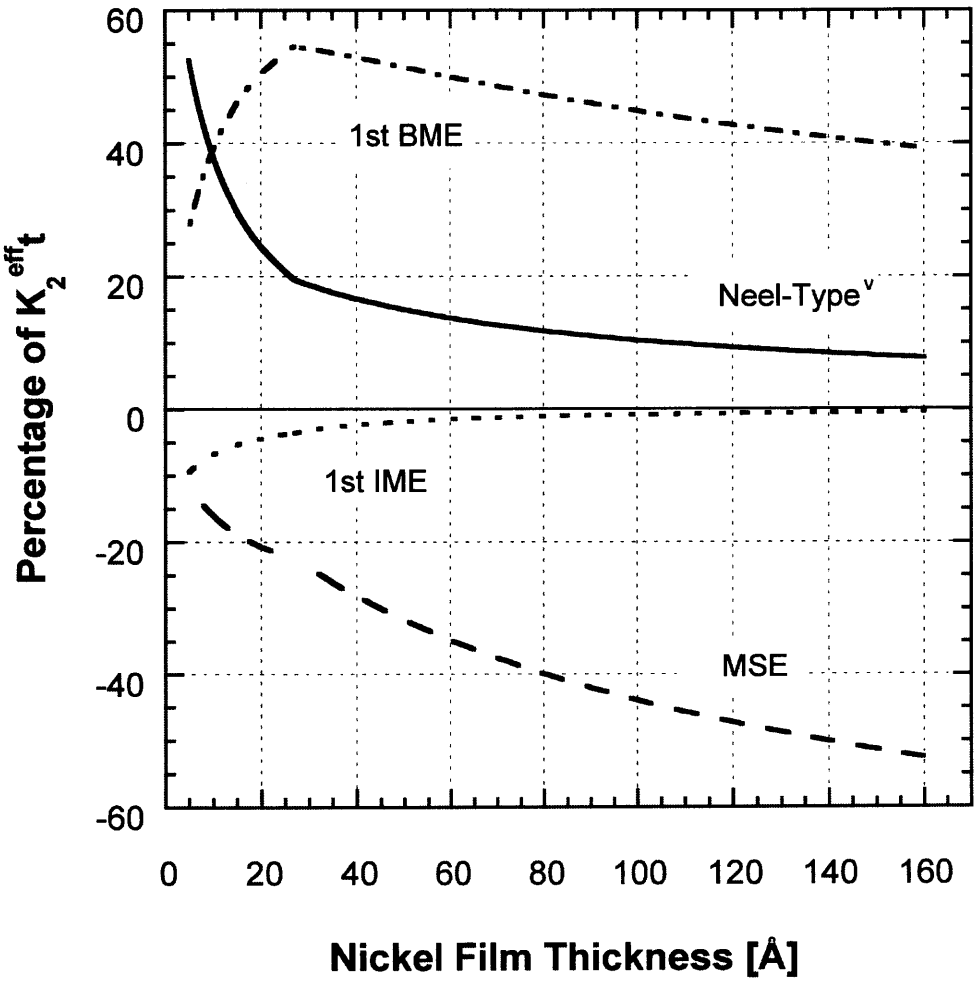

Figure 6.2: Individual energy contribution to the effective magnetic anisotropy in percentage is shown. The percentage is calculated by dividing each energy term to the sum of all the energy terms in their absolute values. 1st BME = first-order bulk magnetoelastic energy; 1st IME = first-order interface magnetoelastic energy; MSE = magnetostatic energy; Neel-Type^{v} = Néel energy for nickel/vacuum interface.

tendency for the magnetization to go in-plane with decreasing nickel film thickness can be explained without the undesirable consequence in the Jungblut's approach.

6.3 Second-Order Spin-Pair Model

The importance of second-order ME term has been reported by Koch *et. al.* [1996] in epitaxial Fe(001) films. It was found that the ME coefficients begin to deviate from their bulk values for the iron films that have intrinsic stress above 0.1 GPa (which corresponds to a strain of about 0.1%). The ME coefficient B_1 of bulk nickel is about two times that of bulk iron. Because the nickel films in the Cu/Ni/Cu(001) films can be strained to about 2.6%, there are good reasons to believe that the second-order ME terms may also become important, particularly as the nickel film thickness decreases.

The effective ME coefficient B_1^{eff} has been measured directly using the cantilever technique as a part of this thesis work. A large deviation from the bulk coefficient B_1 was found for the nickel films that are less than 500Å thick. The experimental setup and results will be presented in chapter 7. In this chapter, the ME coefficients are found using the magnetic anisotropy data with the help of the SP model. The advantage of this approach is that all the MR coupling coefficients (up to second-order strain terms) can be found, some of which would be difficult to measure by the direct method. The results of the two approaches will be compared in chapter 7.

Unlike the first-order model, there are two adjustable parameters (K_N and A_{11}^b) in the second-order SP model. The variation in K_N is an attempt to capture the copper/nickel interaction at the interfaces. The adjustment in A_{11}^b captures the ME non-linear feature in the magnetic anisotropy. It is interesting to note that the change in the K_N parameter affects $K_2^{eff}t$ only uniformly, that is, its changes are the same for all the nickel film thicknesses. The curvature of $K_2^{eff}t$ comes strictly from varying

Table 6.2: Second-order bulk ME coefficients are determined using the second-order SP model. The input parameters for the model are: $B_1 = 6.2 \times 10^7$ ergs/cm^3, $B_2 = 8.6 \times 10^7$ ergs/cm^3, $a_o = 3.5241$Å, and $2c_{12}/c_{11} = 1.28$. The two fitting parameters are A^b_{11} and K_N.

$10^{10} \times$ ergs/cm^3						
$\rho \frac{d^2 L(\frac{a_o}{\sqrt{2}})}{dr^2} \frac{a_o^2}{2}$	A^b_{11}	A^b_{12}	A^b_{13}	A^b_{21}	A^b_{22}	A^b_{rs}
-2.18	-1.09	0.15	-1.24	-4.36	0.61	1.07

the A^b_{11} parameter.

Eq. 6.2 is used to fit the anisotropy data. All the linear terms stay the same as they are in the linear model. The coefficients A^I_{rs} and A^b_{rs} are expressible in term of A^b_{11} using the relations from table 2.1. Again, the power law (Eq. 6.4) is used to model the in-plane residual strain of the nickel layer. Because the saturation magnetization decreases with nickel film thickness (particularly for the nickel films that are less than 50Å, as shown in chapter 5), the magnetostatic energy (which is $2\pi M_s^2$ for thin films) is adjusted by assuming there are two magnetically dead monolayers at each copper/nickel interface. The results of the fitting are tabulated in table 6.2 and 6.3. The fitting curve is shown in figure 6.3 along with the three sets of experimental data.

Figure 6.4 shows the contribution of each energy term in percentage to the total second-order angular anisotropy energy. The percentage is calculated by dividing each energy term to the sum of all the individual terms in K_2^{eff} at their absolute values. The positive or negative sign is to denote whether the energy term favors in-plane or out-of-plane magnetization, respectively.

The new terms in the second-order model are K_N and all the second-order ME terms. All the linear ME terms have the same numerical values as they are in the linear model, but their contributions in percentage to the total anisotropy are weighed

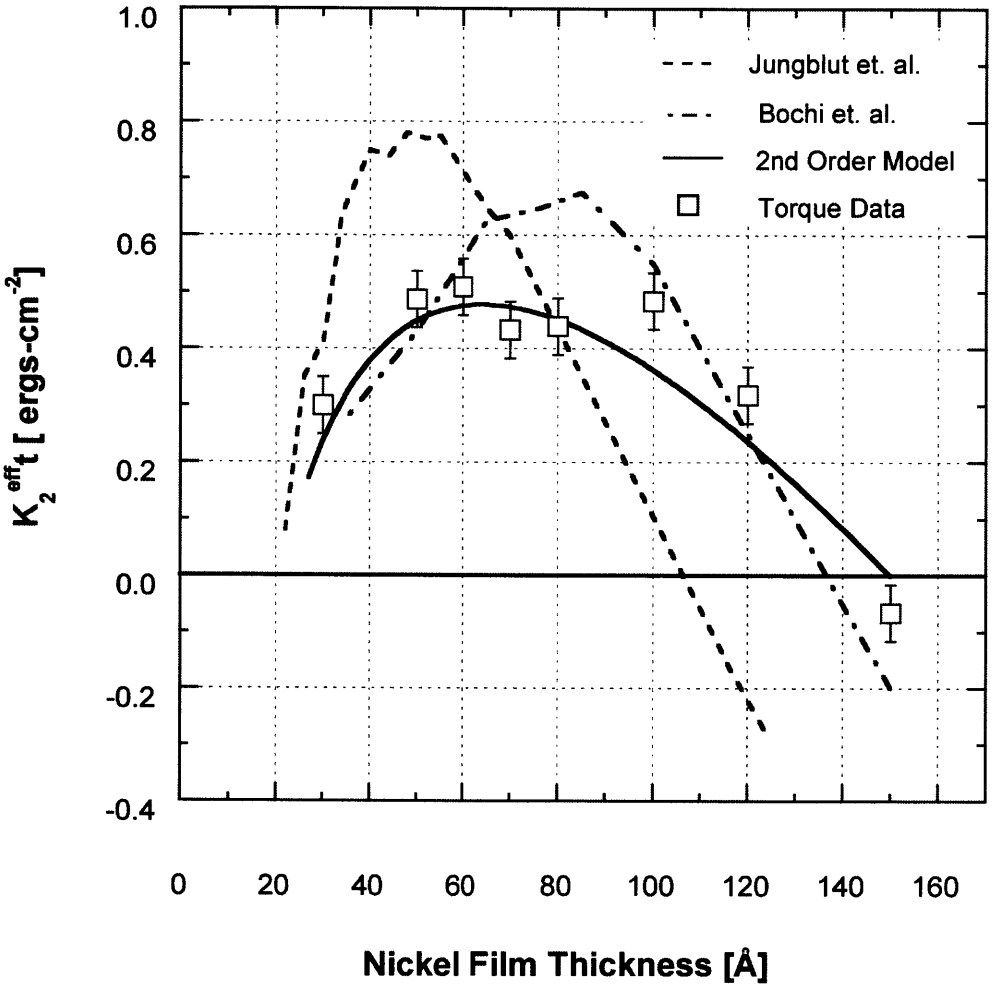

Figure 6.3: Thickness-weighed effective anisotropy of the Cu/Ni/Cu/Si(001) films as fitted by the second-order SP model. Three sets of experimental data are also shown for comparisons.

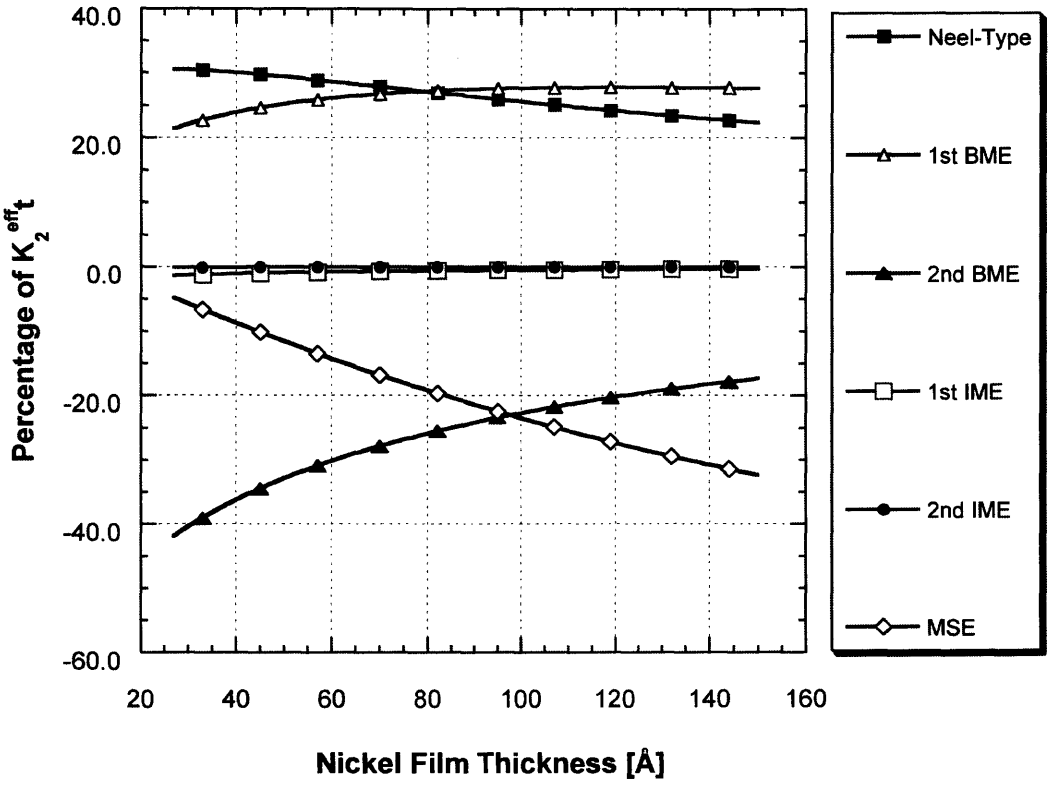

Figure 6.4: Individual energy contribution to the effective magnetic anisotropy in percentage is shown. The percentage is calculated by dividing each energy term to the sum of all the energy terms in their absolute values. 1st BME = first-order bulk magnetoelastic energy; 2nd BME = second-order bulk magnetoelastic energy; 1st IME = first-order interface magnetoelastic energy; 2nd IME = second-order interface magnetoelastic energy; MSE = magnetostatic energy; Neel-Type = Néel energy for copper/nickel interface.

Table 6.3: Néel interface term and second-order interface ME coefficients are determined using the second-order SP model. The input parameters for the model are: $B_1 = 6.2 \times 10^7$ ergs/cm^3, $B_2 = 8.6 \times 10^7$ ergs/cm^3, $a_o = 3.5241$Å, and $2c_{12}/c_{11} = 1.28$. The two fitting parameters are A^b_{11} and K_N.

ergs/cm^2				
K_N	A^I_{12}	A^I_{13}	A^I_{22}	A^I_{rs}
0.71	13.44	-13.44	26.89	-1.88

differently due to the introduction of the new terms in the anisotropy expression.

Note that $K_N \approx 4K^v_N$. This means that the magnetization of the nickel at a Cu/Ni interface is more inclined to point out of plane of the film than that at a vacuum/Ni interface. For the 30Å nickel film, the Néel interface energy makes up about 30% of the total anisotropy energy.

The second-order ME term favors in-plane magnetization. Its contribution is particularly important for the thinner nickel films. There, the nickel layers are most strained. For the 30Å nickel film, the second-order ME energy makes up about 40% of the total anisotropy energy.

Note that the first-order ME anisotropy favors out-of-plane magnetization whereas the second-order ME anisotropy favors in-plane. Both contributions are negligible to the overall anisotropy of the system.

The effective bulk and interface ME coupling coefficients are plotted as functions of in-plane strain as shown in figure 6.5 and 6.6, respectively. Observe that D^b_{22} changes sign at about 0.3% strain. D^b_{11} also changes sign at a strain of about 0.5%. The only interface ME term changes sign is D^I_{13}, which happens at a strain of 1.3%.

It is worth mentioning that the ME coefficients of the nickel films are general

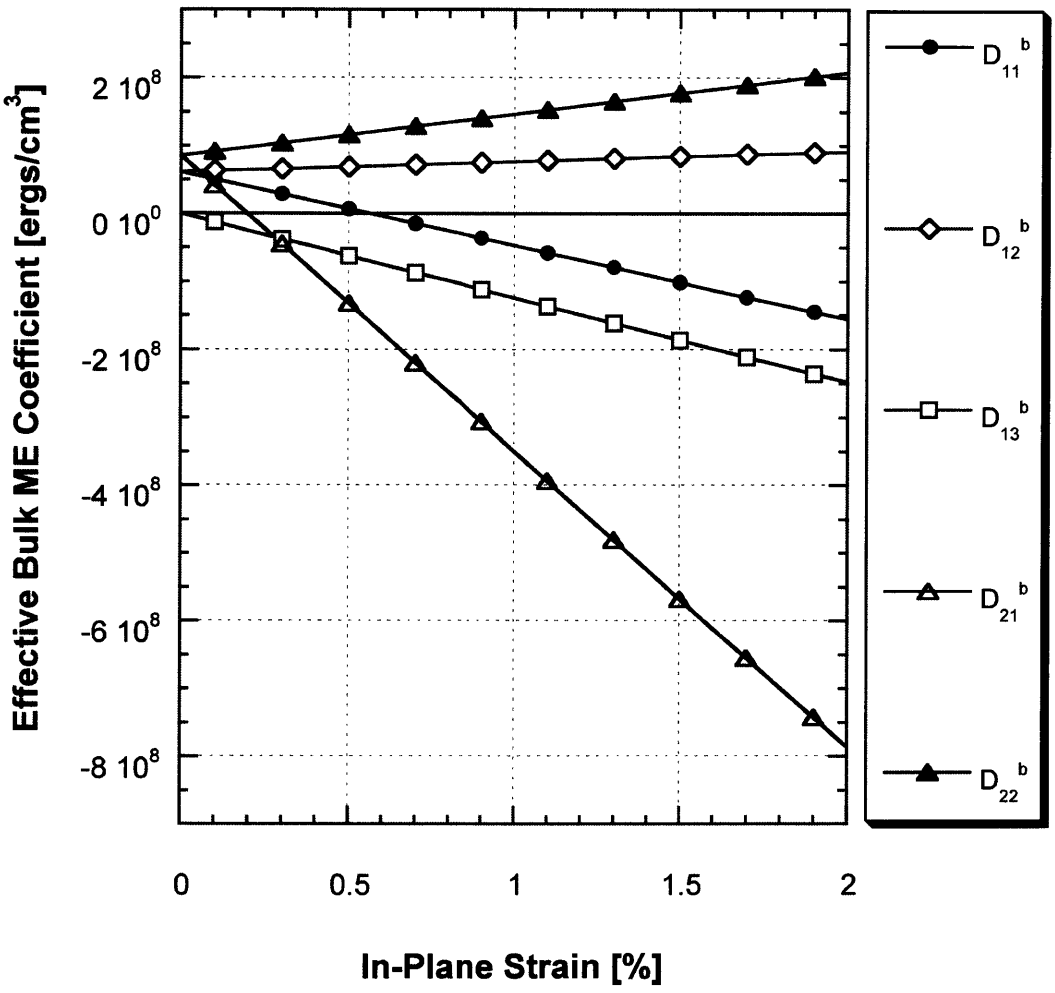

Figure 6.5: Effective bulk ME coupling coefficients of tetragonally distorted (001) nickel are plotted as a function of in-plane strain. They are linear because we are using only second-order ME model.

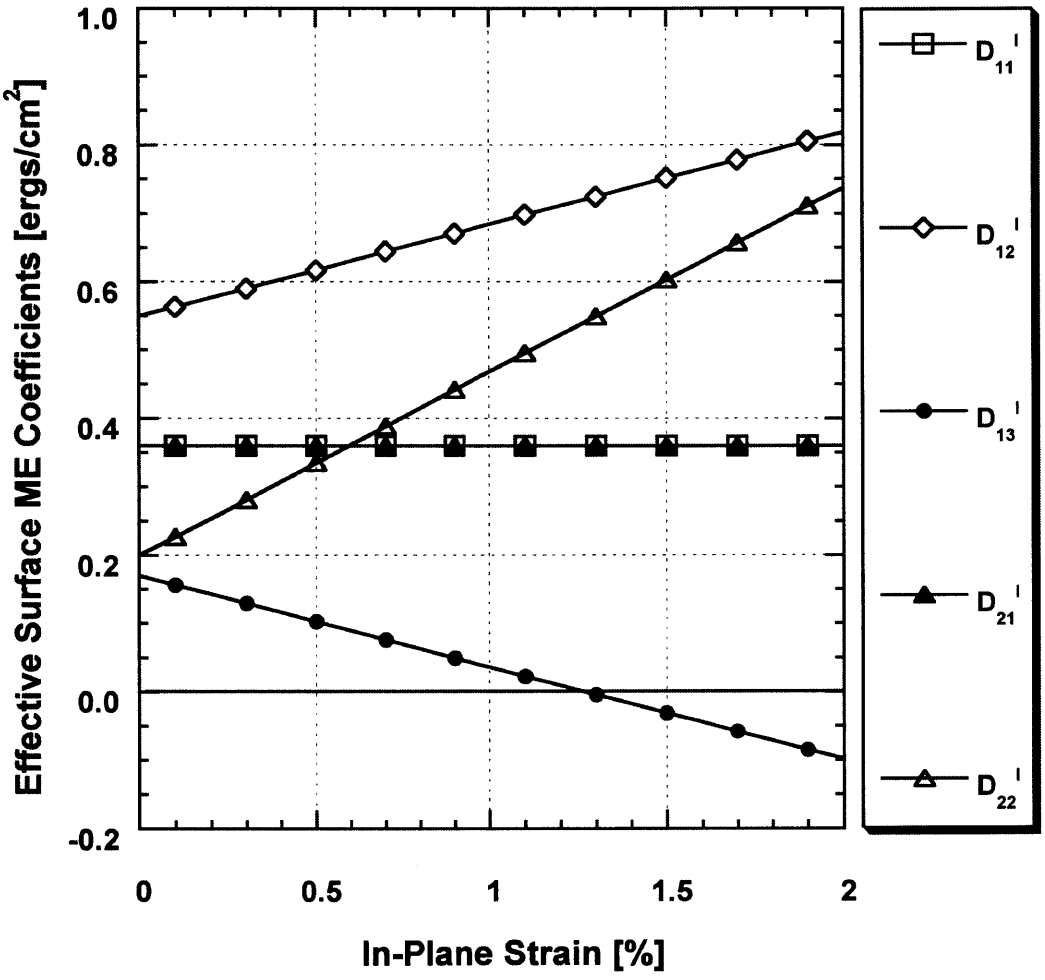

Figure 6.6: Effective interface ME coupling coefficients of tetragonally distorted (001) nickel are plotted as a function of in-plane strain. They are linear because we are using only second-order ME model.

in that their values are valid for nickel films that have different orientations and interfaces. If the strain state of a nickel film is known, all of its ME coefficients can be calculated using the numbers that are tabulated in tables 6.1, 6.2, and 6.3.

6.4 Summary

All the first-order ME coefficients are calculated using the first-order SP model with two well-known input parameters: B_1 and B_2. All the second-order ME coefficients are found by fitting the effective anisotropy data. These ME coefficients are general in that they can be used to any nickel films of different orientation and interfaces. The two major findings from the second-order SP model in its application to the Cu/Ni/Cu(001) films are: i) K_N is positive and thus favors out-of-plane magnetization; ii) the second-order bulk ME term is the major driving force for the in-plane reorientation of the magnetization as the nickel film thickness decreases.

Chapter 7

Direct Evidence

A cantilever beam magnetostrictometer(CBM) has been used to measure one of the effective ME coefficient (B_{11}^{eff}). As far as we know, this is the first direct measurement of the ME coefficient in the Cu/Ni/Cu(001) system. The result provides a direct confirmation on some of the predictions by the SP model discussed in chapter 6. The experimental setup and results are presented in this chapter.

The general idea of the cantilever beam technique is the following: a film is first cut to have the shape of a cantilever. One end of the cantilever is clamped, and the other is free to deflect in the presence of an applied magnetic field. The direction and magnitude of the deflection are related to the magnetostrictive stresses in the film (see figure 7.1). The equation that relates an *uniaxial* stress in the beam direction and beam deflection is

$$\sigma_{\parallel} = \frac{1}{3}\frac{E_s t_s^2}{t_f L^2} D_L \tag{7.1}$$

where $\sigma_{\parallel}$ is the stress along the beam direction, E_s is the Young modulus of the substrate, t_s the substrate thickness, t_f the film thickness, L the distance from the clamped end to the capacitive plates, and D_L is the deflection of the beam at the

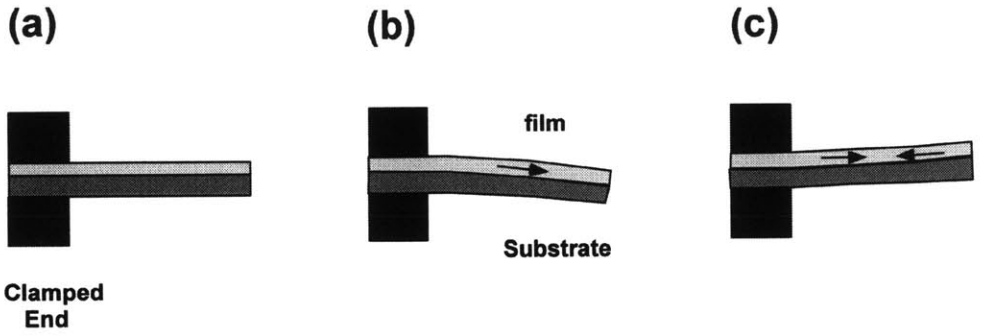

Figure 7.1: An illustration of the relation between a film stress along the beam direction to beam deflection. a) zero stress; b) tensile stress; c) compressive stress.

distance L away from the clamped end. The derivation of Eq. 7.1 has been shown by many authors [Campbell, 1970, p. 12-25; Klokholm, 1976; de Lacheisserie and Puezin, 1994; Marcus, 1997]. Note that if the stress is not uniaxial, a slight modification of the equation is needed, as it will be discussed later.

There are many ways of measuring the deflection of the cantilever. Klokholm [1976] measured it by detecting a shift in the resonance frequency of a RLC circuit. The cantilever beam functioned as one of the two capacitor plates of the circuit. Tam and Schroeder [1989] measured it by detecting a reflected laser beam incident on the sample with a position-sensitive sensor array. The method was made sensitive with the use of a phase-sensitive lock-in amplifier. Koch *et. al.* measured it by a differential capacitance method in combination with a phase-sensitive detection. Their apparatus was UHV-compatible. Rengarajan *et. al.* [1995] used a highly sensitive optical interferometer to measure the beam deflection. The resolution of that setup was reported to be about 0.01Å.

A cantilever beam magnetostrictometer(CBM) similar to the one used by Koch *et. al.* [1990] has been built. One difference between the two designs is the incorporation of a piezoelectric transducer (or piezo for short) in our setup. The piezo is used to

calibrate the beam deflection as opposed to calibrating it by hanging a known weight onto the beam at a fixed position, as was done by Koch *et. al.* [1990]. The advantages of using a piezo will be discussed later in the chapter.

7.1 Experimental Setup

Figure 7.2 shows the components of the CBM. The cantilever (usually of dimension 3cm × 0.5cm) is clamped on one end. The free end is positioned between two capacitor plates whose gap size is 0.12 cm. Each plate is driven by a 3 KHz sinusoidal voltage source that is 180° out of phase from the other (see figure 7.3). The cantilever beam acts like a probe that reads the potential between the two capacitor plates.

The voltage of the cantilever (the output voltage) is detected by a lock-in amplifier (see figure 7.3). To maximize the fraction of the change in the output signal, it is necessary to null the circuit (namely, to minimize the output voltage) before the start of each measurement. The nulling is accomplished by attenuating the amplitude of one of the driving voltages as shown in figure 7.3.

The calibration of the output voltage to the beam deflection is accomplished with the help of a piezo (made by Physik Instrumente) as shown in figure 7.2.[1] Because the two capacitor plates are rigidly attached to the piezo, their displacement would result in an equivalent movement of the beam in the opposite direction. Figure 7.4 shows an example of a calibration curve (which is a plot of the output voltage as a function of the piezo displacement). The piezo is expanded from 0.6 to 1.5 μm. Note that the output voltage varies *linearly* over a remarkably wide range of the beam displacement which is large in comparison to the deflection due to magnetostrictive

[1]The piezo was calibrated in the factory by Physik Instrumente. A strain-gage sensor (which comes with the piezo stack) was used to provide a feedback loop to monitor the linearity in the piezo expansion with an applied ramp voltage.

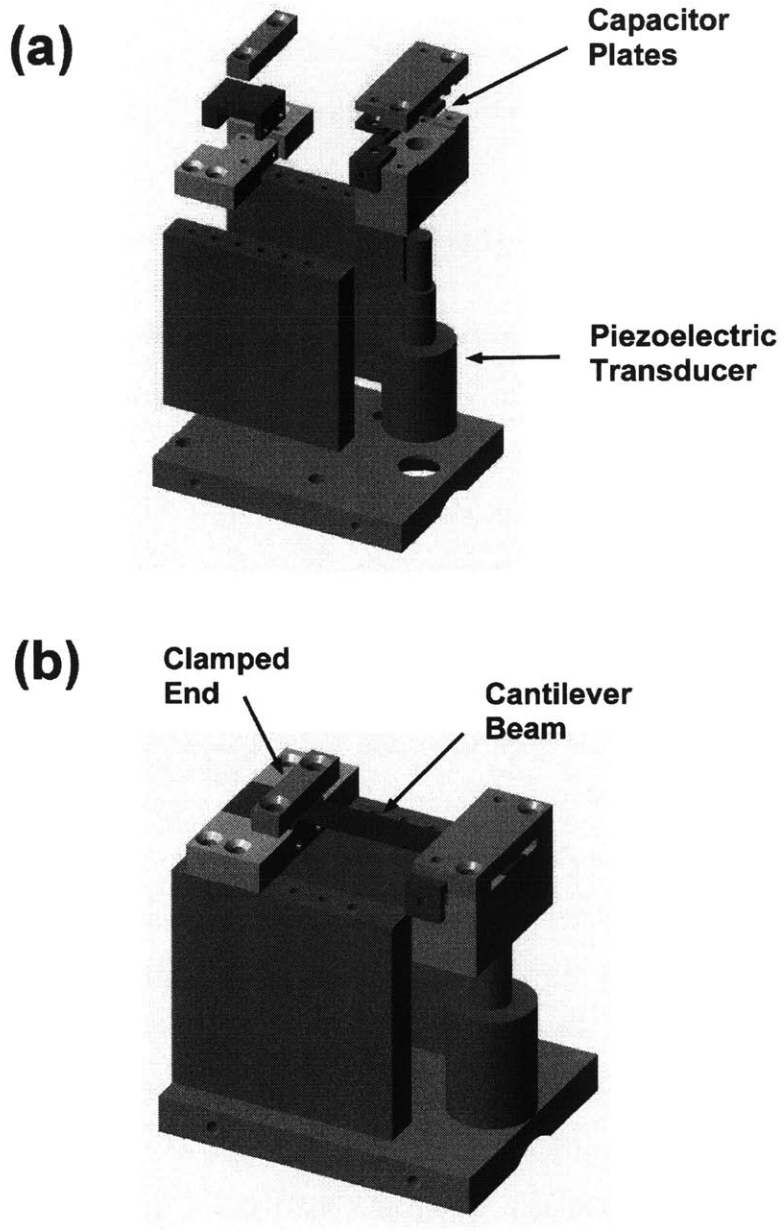

Figure 7.2: Component drawing of the cantilever beam magnetostrictor. a) before the components are assembled; b) after the components are assembled. A cap (made out of aluminum; not drawn) is used to seal the system from the surrounding electronic noise and to keep the temperature of the system stable within the measurement time (The figures are drawn by Andrew Gallant from the MIT Central Machine Shop).

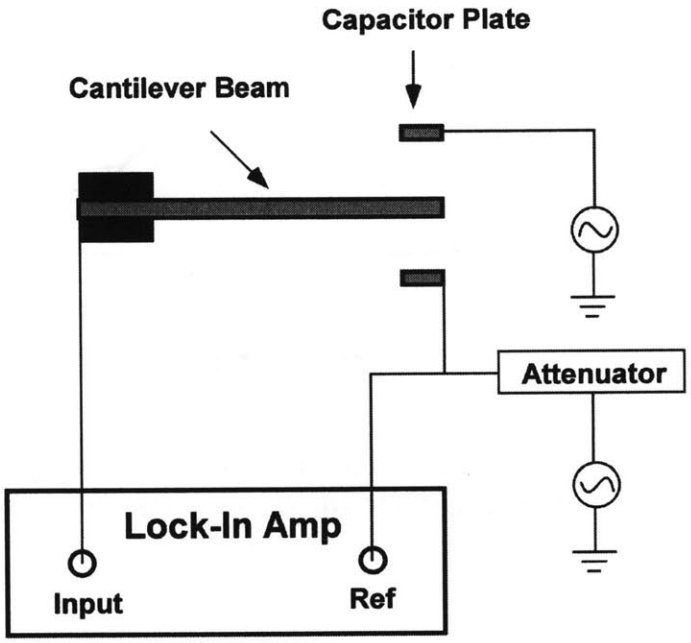

Figure 7.3: A schematic of the electrical circuit for the cantilever beam magnetostrictor.

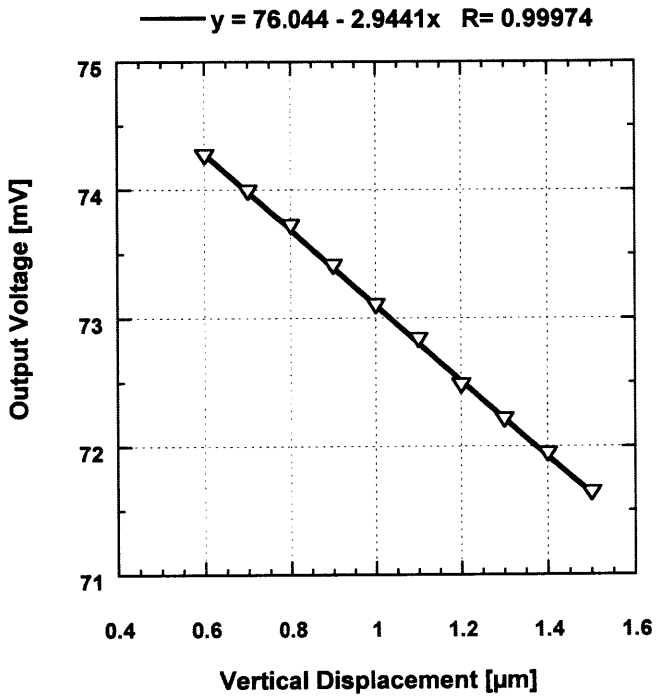

Figure 7.4: The graph of a typical calibration curve obtained before the magnetostrictive stress curve is measured. The triangles are the experimental data. The solid line is a least-square fit.

stress. Thus, linearity in the output voltage as a function of beam deflection due to magnetostrictive stresses can be safely assumed.

A calibration curve is generated for each measurement. This way of calibrating the output voltage has many advantages over that of using a known standard. The uncertainty resulting from the differences in dimensions between the sample and the known standard is eliminated. It also eliminates the error due to the differences in the placement of the sample and the known standard in the CBM. Further, it also has advantages over the calibration method by hanging a known weight onto the

cantilever. For one thing, the piezo gives a finer control over beam displacement.

7.2 Measurement Procedure

Magnetostrictive stress along [β_1, β_2, β_3] direction — denoted as $\sigma(\beta_1, \beta_2, \beta_3)$ — is related to the ME coefficients by the following equation:

$$\begin{aligned}\sigma(\beta_1,\beta_2,\beta_3) &= -\beta_1^2[B_{11}^{eff}(\alpha_1^2-\frac{1}{3})+B_{13}^{eff}(\alpha_2^2-\frac{1}{3})] \\ &\quad -\beta_2^2[B_{11}^{eff}(\alpha_2^2-\frac{1}{3})+B_{13}^{eff}(\alpha_1^2-\frac{1}{3})]-\beta_3^2[B_{12}^{eff}(\alpha_3^2-\frac{1}{3})] \\ &\quad -B_{21}^{eff}[\beta_1\beta_2\alpha_1\alpha_2]-B_{22}^{eff}[\beta_2\beta_3\alpha_2\alpha_3+\beta_3\beta_1\alpha_3\alpha_1] \qquad (7.2)\end{aligned}$$

where α_1, α_2, and α_3 are the direction cosines of the magnetization. The derivation of Eq. 7.2 is shown in appendix E. Note that the stress along any arbitrary direction of the beam is not zero and it changes with the direction of the magnetization. Thus, magnetostrictive stresses are *not* uniaxial. The deflection of the beam can be due to the stress component along the beam direction as well as the stress component normal (but still in-plane) to the beam direction due to the Poisson effect. The out-of-plane stress component does not affect the deflection of the beam because the film is free to expand in the out-of-plane direction.

In the cantilever setup, only the stress along the beam direction is measured. The stress depends on the direction of the magnetization. The cantilever is cut along the nickel [100] crystallographic direction with [001] pointing out of the plane of the film. Thus, the effective stress along the beam direction when the magnetization is in-plane is

$$\sigma_{\parallel} = \sigma_{\parallel}(1,0,0) + \nu_s\sigma_{\parallel}(0,1,0). \qquad (7.3)$$

where ν_s is the Poisson ratio of substrate. The second term in the above equation is the contribution from the stress perpendicular to the beam direction via the Poisson effect. Similarly, when the magnetization is out-of-plane, the stress component along the beam direction is

$$\sigma_\perp = \sigma_\perp(1,0,0) + \nu_s\sigma_\perp(0,1,0). \tag{7.4}$$

Using Eq. 7.2, the difference in the effective stresses along the beam direction becomes

$$\sigma_\parallel - \sigma_\perp = B_{11}^{eff} + \nu_s B_{13}^{eff} \tag{7.5}$$

Eq. 7.1 can then be used to relate the ME coefficients to the beam deflections:

$$B_{11}^{eff} + \nu_s B_{13}^{eff} = \frac{1}{3}\frac{E_s t_s^2}{t_f L^2}(D_\perp - D_\parallel) \tag{7.6}$$

where $D_L^\perp$ and $D_L^\parallel$ are the deflection of the cantilever at a distance L from the clamped end with the magnetization points in the [0,0,1] (namely, out-of-plane) and [1,0,0] (namely, in-plane) directions, respectively.

Since the Poisson ratio of the silicon substrate is small in this particular geometry ($\nu_s = 0.064$ [Brantley, 1973]), the contribution from the B_{13}^{eff} coefficient (namely, the second term in Eq. 7.6) can be neglected. Thus,

$$B_{11}^{eff} \approx \frac{1}{3}\frac{E_s t_s^2}{t_f L^2}(D_\perp - D_\parallel) \tag{7.7}$$

There is a fundamental problem in measuring the deflection when the magnetization is out-of-plane using the cantilever beam method. The attraction of the nickel moment to the external field can result in bending the substrate much more strongly

than that due to the magnetostrictive stresses. However, for films that show perpendicular magnetization (namely, the nickel films that are less than 100Å thick), B_{11}^{eff} can be obtained by simply measuring the change in the beam deflection from the [100] saturation state to a demagnetized state. The reason is the following: because the easy axis of magnetization is out-of-plane, the perpendicular magnetization process is achieved by domain wall motion which does not give rise to magnetostrictive stresses. In these cases,

$$B_{11}^{eff} = \frac{E_s t_s^2}{3 t_f L^2}(D_L^{\text{demag}} - D_L^{\parallel}) \tag{7.8}$$

where D_L^{demag} is the beam deflection at a demagnetized state. We will use this procedure to determine B_{11}^{eff} for all the nickel films. For films that show in-plane magnetization (namely, the nickel films that are thicker than 150Å), the values for B_{11}^{eff} tend to be underestimated because the magnetostrictive stresses due to the rotation of the magnetization to out-of-plane have not been accounted for in the procedure.

7.3 Experimental Results

Figure 7.5 and 7.6 show the magnetostrictive stress curves (plots of magnetostrictive stresses with applied magnetic fields along the cantilever beam direction) of the Cu(50Å)/Ni(t_{Ni})/Cu(2000Å)/Si(001) films. The beam deflections are also shown in the graphs. The magnetostrictive stress is calculated using Eq. 7.1 with $E_s = 1.69 \times 10^{12}$ dynes/cm^2 [Brantley, 1973]. Observe that for all the nickel films that are less than 500Å thick, the magnetostrictive stresses become more tensile with increasing magnetic field. Thus, they are positive magnetostrictive materials. The 2000Å film (which is a relatively thick film) exhibits a negative magnetostrictive behavior which

Table 7.1: A summary of the values of B_{11}^{eff} as a function of the nickel film thickness and its in-plane strain.

t_{Ni}[Å]	Strain [%]	B_{11}^{eff}
30	2.26	-1.2 × 10^9
60	1.81	-5.5 × 10^8
80	1.29	-1.8 × 10^8
120	1.09	-1.2 × 10^8
150	0.90	-4.5 × 10^7
500	0.68	-1.0 × 10^7
2000	0.32	5.2 × 10^7

is consistent with a bulk nickel. The magnetostrictive stress curve for the 150Å film shows some interesting behavior; the stress becomes more compressive beyond 1300 Oe field. The cause of this abnormal data is still under investigation.

B_{11}^{eff} is estimated by taking the difference in the magnetostrictive stresses at zero field and at the saturation field or the highest field that can be achieved with our electromagnetic (which is about 5000 Oe). For the 2000Å film, it is estimated to be 5.2 × 10^7 ergs/cm^2, which is slightly smaller than the bulk value B_1 (which is 6.2 × 10^7 ergs/cm^2).

Figure 7.7 shows B_{11}^{eff} as a function of nickel film thickness. The values are also tabulated in table 7.1. It is clear from the graph that there is a transition from bulk-like negative to positive magnetostriction with decreasing nickel film thickness. The plot shows that the transition occurs near 600Å of nickel.

It is believed that the changes in B_{11}^{eff} are due to the large residual strain in the nickel layer. Thus, it is natural to plot it as a function of the in-plane residual

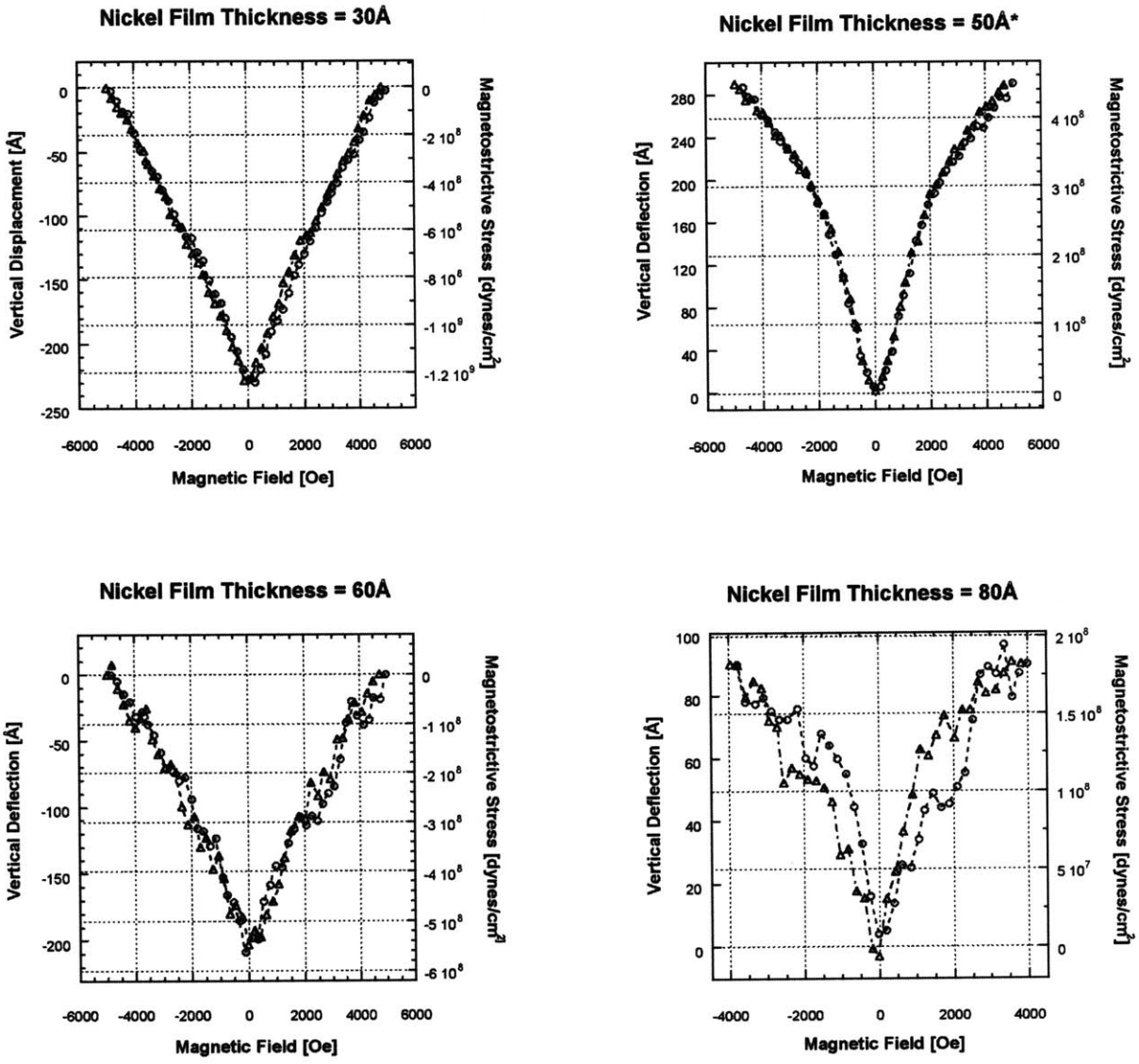

Figure 7.5: Magnetostrictive stresses of Cu(50Å)/Ni(t_{Ni})/Cu(2000Å)/Si(001) films (t_{Ni} = 30Å, 50Å, 60Å, and 100Å) are plotted as functions of applied field along the nickel [100] crystallographic direction. The cantilever beam is cut also in the nickel [100] crystallographic direction. The 50Å nickel film is from a different batch from all the others. It was grown on a flexible Si(001) substrate (whose thickness is about 200μm). All the others are grown on regular Si(001) substrate (whose thickness is about 350μm.

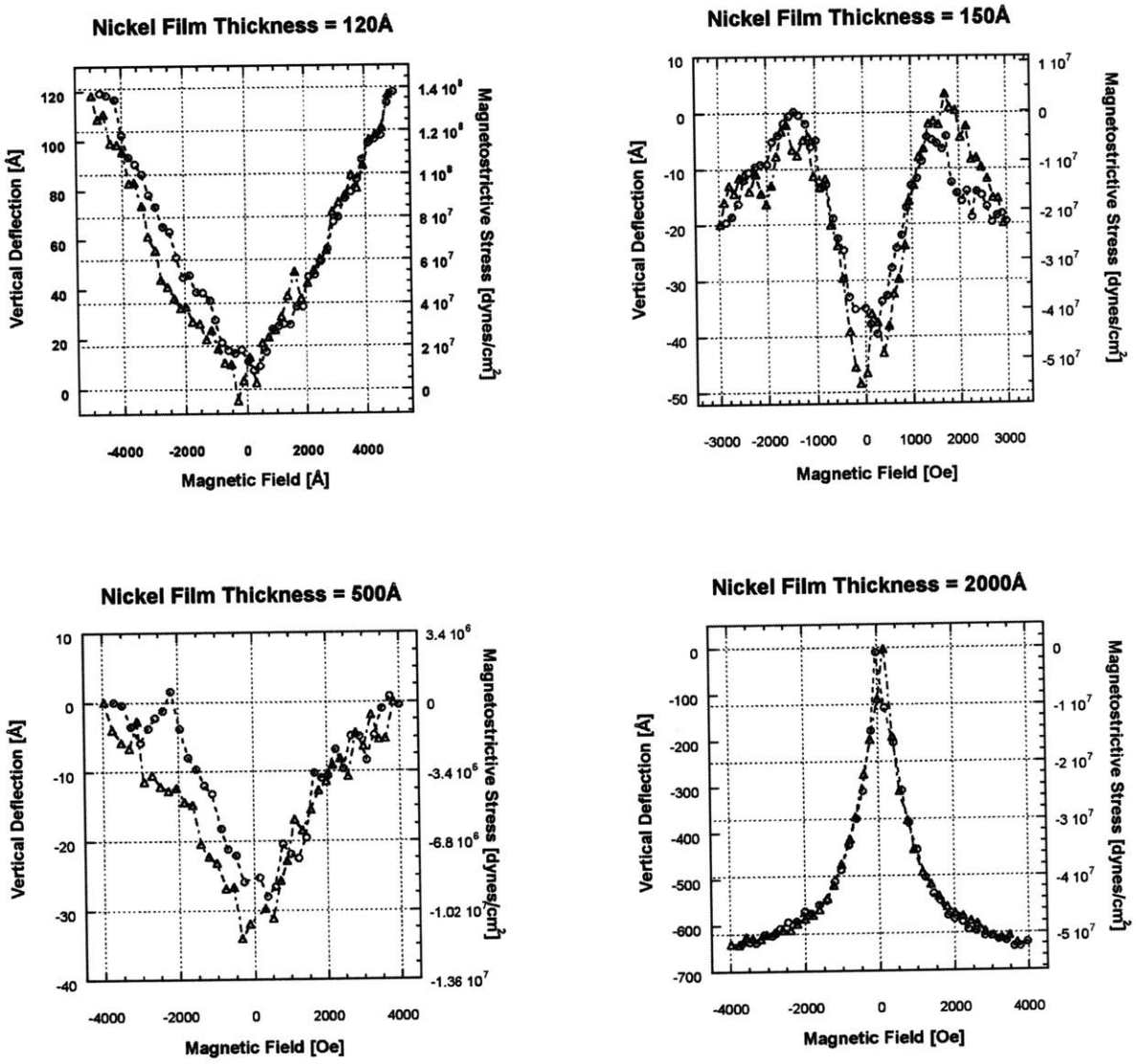

Figure 7.6: Magnetostrictive stresses of Cu(50Å)/Ni(t_{Ni})/Cu(2000Å)/Si(001) films (t_{Ni} = 120Å, 150Å, 500Å, and 2000Å) are plotted as functions of applied field along the nickel [100] crystallographic direction. The cantilever beam is cut also in the nickel [100] crystallographic direction. All the nickel films are grown on regular Si(001) substrates (they are about 350μm thick).

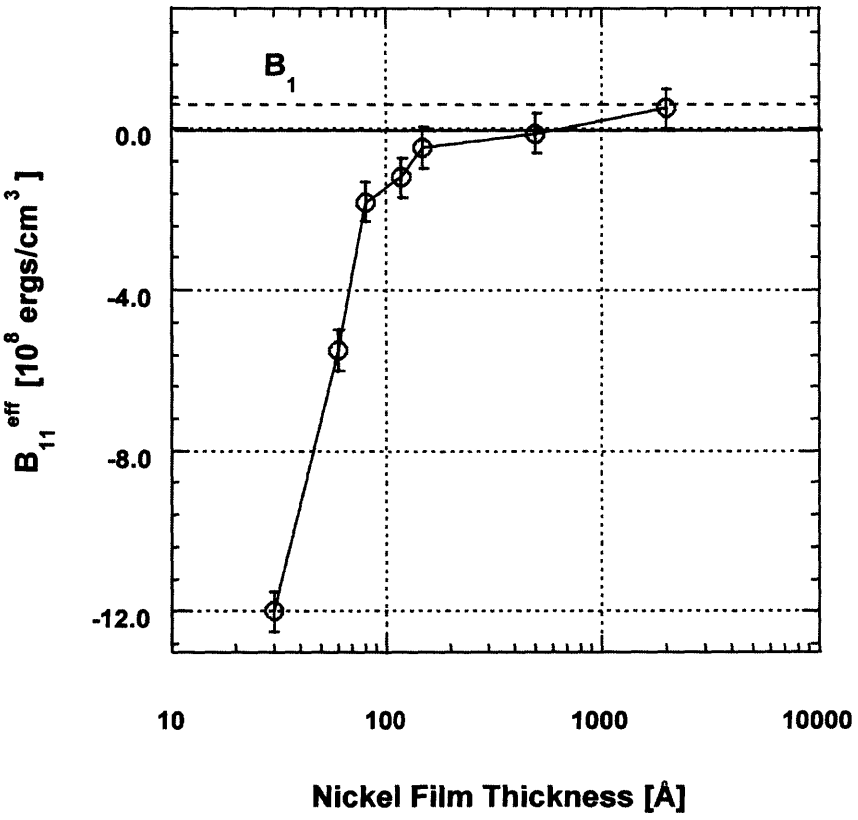

Figure 7.7: B_{11}^{eff} of the Cu(50Å)/Ni(t_{Ni})/Cu(2000Å)/Si(001) films is plotted as a function of the nickel film thickness.

strain, as shown in figure 7.8. Note that the transition from negative to positive magnetostriction occurs at a strain of 0.5%.

Figure 7.8 also shows the B_{11}^{eff} predicted by the second-order SP model. The two results are in good agreement up to a strain of about 1%. A considerable deviation from the second-order SP prediction is observed. The origin of the "nonlinearity" is possibly due to a third-order ME effect.

7.4 Summary

The ME coefficient B_{11}^{eff} of the Cu/Ni/Cu/Si(001) system has been measured. It is found that the coefficient changes significantly with film thickness and in-plane strain of the nickel layer. For nickel films that are less than 500Å thick, B_{11}^{eff} changes sign from their bulk value. At 30Å, it is about -20 times the bulk value. The prediction of the second-order SP model agree well with the measurement if the in-plane strain is less than 1%.

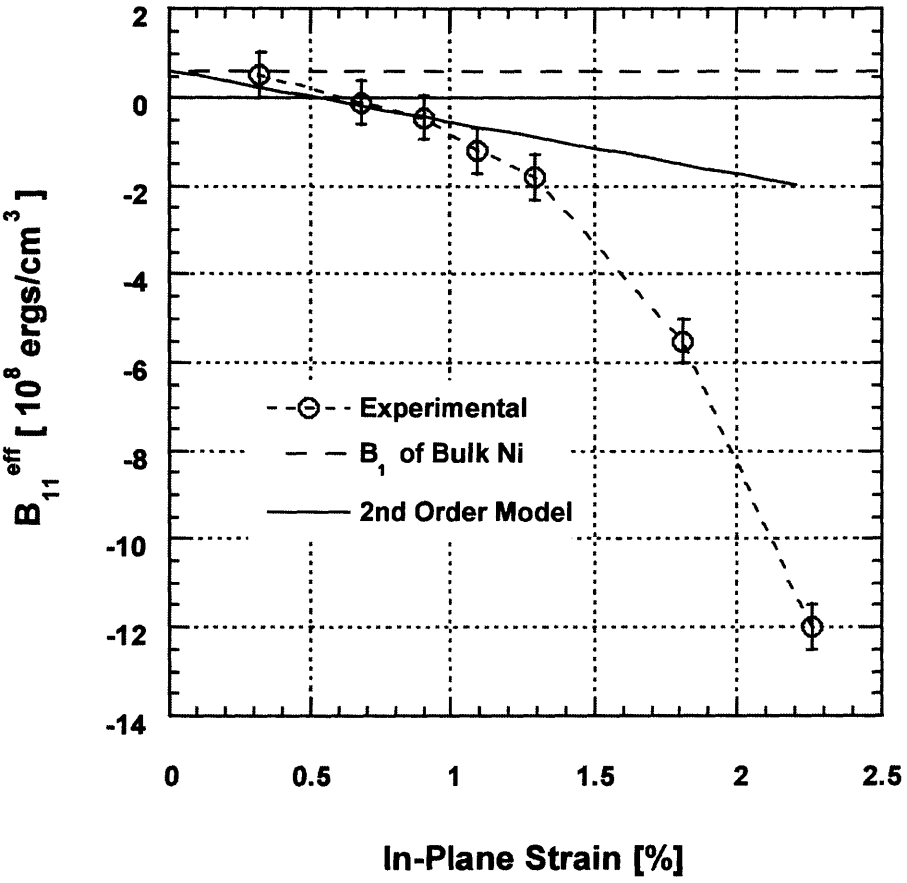

Figure 7.8: B_{11}^{eff} of the Cu(50Å)/Ni(t_{Ni})/Cu(2000Å)/Si(001) films is plotted as a function of in-plane strain. The predicted curve by the second-order SP model is also shown.

Chapter 8

Discussion

The Cu/Ni/Cu/Si(001) system has been a model system for the study of magnetoelastic interactions in thin films. The easy axis of magnetization is significantly influenced by the residual strain in the nickel layer. The wide thickness range over which perpendicular magnetization is observed offers an unique opportunity to investigate the effect of the magnetoelastic couplings in some detail. The misfit strain between the nickel and copper is 2.6%, not too large to prohibit epitaxial growth, but large enough that non-linear ME effect can become important. The analysis of the SP model has led to the conclusion that the bulk ME contribution (the sum of first- and second- order bulk ME terms) is more than 50% of the total anisotropy for film thicknesses between 30Å to 150Å (see figure 6.4).

One major problem in the Jungblut and Bochi models is the neglect of higher order ME terms. Both models explain the out-of-plane easy axis in term of the negative magnetostrictive property of bulk nickel. But our analysis of the magnetic anisotropy and the direct measurement of B_{11}^{eff} show that for nickel films that are less than 500Å thick, the magnetostriction is positive along the nickel crystallographic [100] direction (see figure 7.8). The transition from negative to positive magnetostriction

with decreasing nickel film thickness is due to the increasing importance of the second-order ME term as shown in figure 6.4.

A crucial step in analyzing the magnetic anisotropy is in writing a free energy expression for the system. The equation is used to fit experimental data or data calculated from first principles. The outcome of the analysis depends on what terms are included in the free energy expression. The credibility of the analysis cannot and should not be granted just because the equation fits the data nicely, but because the results are reasonable and are in good agreement with other independent measurements.

In the Jungblut model, the free energy was composed of magnetostatic energy, a first-order bulk ME term, and the Néel interface term. The magnetostatic energy favors in-plane magnetization due to the large aspect ratio between the in-plane and out-of-plane physical dimensions. The first-order ME term favors out-of-plane magnetization due to the in-plane biaxial tensile strain in the nickel layer. Thus, in order to explain the effective magnetic anisotropy that shows an upside-down v-shape behavior (figure 6.3), it is necessary (for the Jungblut model) to attribute the tendency for the in-plane magnetization with decreasing nickel film thickness to an assumed negative Néel interface term. But the model has a highly undesirable consequence: the peak in the anisotropy must correspond to the coherent/incoherent critical thickness t_c in Ni/Cu(001) films. For the Jungblut films, the effective anisotropy peaks at about 45Å. For the Bochi and our films, the peaks occur at around 80Å. But t_c has been determined to be about 15Å for Ni/Cu(001) films by Matthews and Crawford [1970] and by Inglefield *et. al.* [1994] using transmission electron microscopy. Also, our x-ray diffraction study shows that t_c should occur below 30Å. Thus, there is a large discrepancy between the two critical thicknesses which cannot be reconciled within the experimental errors of the measurements. Because this correspondence of the two

critical thicknesses is a necessary condition in the Jungblut model, the model cannot be right.

In the Bochi model, an interface ME term (B_s) is added to the energy expression. This added term avoids the problem in the Jungblut model, namely the irreconcilable difference between the nickel film thickness at which the effective anisotropy peaks and t_c. However, it has its own set of problems. For example, B_s is estimated to be about -52 ergs/cm^2 [Bochi *et. al.*, 1996]. This value of B_s is inconsistent with the SP model result, namely that the contribution from all interface ME terms (both first- and second- order) are negligible for nickel films that are greater than 30Å (see figure 6.4). Lastly, the Bochi model predicts the nickel film should become positive magnetostrictive above 80Å [Bochi *et. al.*, 1996, p. 124]. The cantilever beam measurement shows that the nickel film remains positive magnetostrictive along the crystallographic [100] direction up to at least 500Å (see figure 7.7). Since the change in sign in B_{11}^{eff} from its bulk value cannot due to interfacial effect in a 500Å nickel film, the Bochi model cannot be right either.

Our analysis of the anisotropy also involves writing an energy expression. One major difference is that all the allowable ME terms for a tetragonally distorted system are included in our fitting. No assumption is made *a priori* on some selected ME terms being more important than the others. Of course, the method hinges on the validity of the SP approach which seems to have much success in its applications to transition metals (see the discussion section in chapter 2).

The direct measurement of B_{11}^{eff} (using the cantilever beam technique) gives some credibility to our SP model analysis. The model predicts a change in sign in B_{11}^{eff} at about 0.6% in-plane strain in good agreement with the direct measurement (see figure 7.8). The deviation of the SP model prediction from the direct measurement result above 1% in-plane strain may be due to third-order ME effect.

The two approaches in estimating the strength of the ME coupling coefficients complements each other. The advantage of the SP method is that all the coupling coefficients can be determined as opposed to only a few using the cantilever beam method. The coefficients that couple the magnetization with the out-of-plane strain component or the shear strains cannot be measured directly by the cantilever technique. But the advantage of the direct measurement is that the result is more credible: there is little theory that goes into the measurement except the theoretical framework that is needed to describe the parameters to be determined.

It is useful to write effective ME coefficients in the bulk reference state rather than in the film reference state (see appendix B). Otherwise, the reported ME coefficients would just be those for that particular film and thus have little practical value. The advantage of using the bulk reference state can be seen by comparing two figures in chapter 7. Figure 7.7 expresses the measured B_{11}^{eff} in the film reference state by plotting it as a function of the nickel film thickness. Although the graph shows that the nickel film changes from being negative to positive magnetostrictive along the crystallographic [100] direction with decreasing film thickness, the value for B_{11}^{eff} cannot be applied for another Ni(001) film that is also under a biaxial tension. On the other hand, figure 7.8 expresses B_{11}^{eff} in the bulk reference state by plotting it as a function of the in-plane strain measured from the bulk lattice. If the strain state of another Ni(001) film is known, the corresponding B_{11}^{eff} can be found by graphical means (with the help of figure 7.8) or can be calculated directly from its definition.

Lastly, it is worth discussing the sign of the Néel interface term which has been at the center of the controversy. The Jungblut model says that K_N must be negative and thus favors in-plane magnetization. The Bochi model says that it is positive and thus favors out-of-plane magnetization. Again, the different conclusion reflects the difference in the energy expressions used in writing the anisotropy. Our SP model

analysis shows that K_N is positive. The reason is clear: since both the strain-induced anisotropy and magnetostatic energy favors in-plane magnetization for nickel film that are less than 500Å thick, the only energy term that can be responsible for the out-of-plane magnetization for the thin nickel films (20Å$\leq t_{Ni} \leq$ 120Å) is the Néel interface term. But this is still not a direct evidence of it. Ideas as to how K_N can be determined directly will be discussed in the next chapter.

Chapter 9

Suggestions for Future Work

Much work can still be done to deepen our understanding of the magnetoelastic couplings in Cu/Ni/Cu/Si(001) films or in thin films in general. We would like to end this thesis by offering a few suggestions for future work.

The Sign for K_N

Although the SP model analysis has conclusively established the magnitude and sign of K_N for a Ni/Cu(001) interface, it is always better to have a more direct measurement of it. One way is to take M-H loops of the nickel atoms near Cu/Ni(001) interface using a grazing-incidence magneto-optical technique. The method should work the same way as a magneto-optical Kerr effect (MOKE) system except that the laser beam would intersects the surface of a film at at a small incident angle with respect to the film surface. The penetration depth of the light can be controlled by changing the incident angle. It would be instructive to do the experiment for the Cu(50Å)/Ni(500Å)/Cu(2000Å)/Si(001) film. Our VSM and torque measurements have shown that the magnetization is mostly in-plane. If the magnetization of

the interface atoms is shown to be more out-of-plane, that would constitute a direct evidence of positive K_N, namely it favors out-of-plane magnetization.

Perhaps a more visual way is to image the magnetization of the interface nickel atoms of the Cu(50Å)/Ni(500Å)/Cu(2000Å)/Si(001) film using a SEMPA (secondary electron microscopy with polarization analysis). Again, if the magnetization of the interface atoms cants out of the film plane, that would provide a direct evidence of the positive sign of K_N.

Varying the Cap Layer Thickness

The Bason and Ball equilibrium model (see chapter 3) predicts that the nickel layer would become more tensile as the cap copper layer thickness increases. For example, figure 9.1 shows that the strain in a 30Å nickel layer can increase from 1% to about 2.6% as the cap copper layer thickness increases from zero to 500Å, and the corresponding effective anisotropy changes from 1.0 to -0.1 erg/cm^2 as predicted by the second-order SP model. Certainly, the nickel is not expected to follow the equilibrium behavior due to kinetic reasons, but some change in the strain state of the nickel is expected. The following crucial experiment can be conducted: A series of Cu(t_{cap})/Ni(30Å)/Cu(2000Å)/Si(001) films are grown with different cap copper layer thicknesses ($20 \leq t_{cap} \leq 500$Å). Measure the magnetic anisotropy either by torque or VSM method. If K_2^{eff} increases with t_{cap}, the experiment would support the Jungblut model. If K_2^{eff} decreases with t_{cap}, then the result would support the second-order SP model.

The nice feature about this experiment is that it isolates the effect of strain from the Néel interface term: at all times, the Cu/Ni(001) interface would be kept.

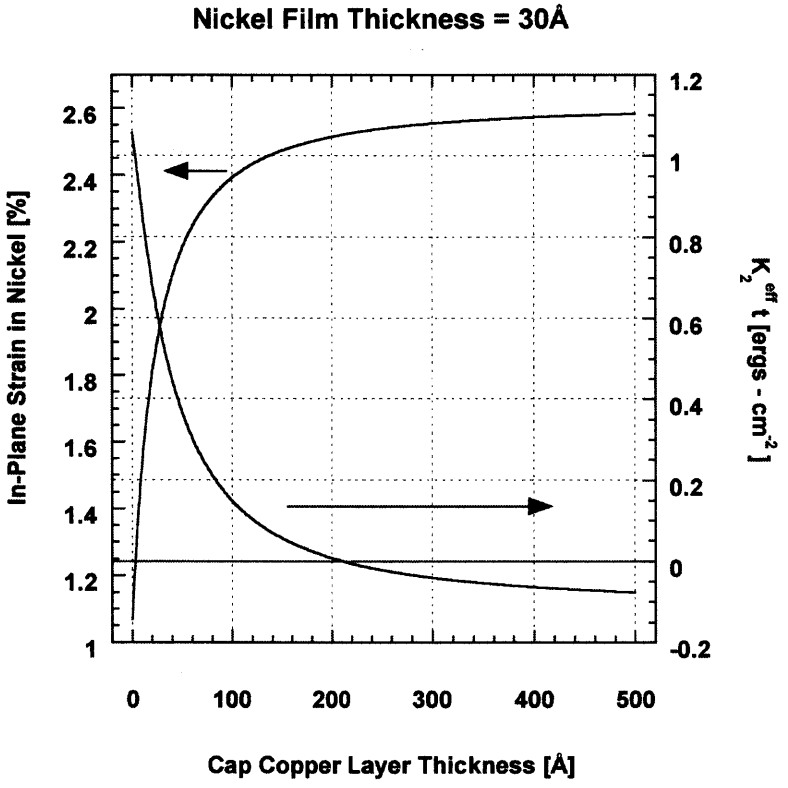

Figure 9.1: The effect of the change in the copper cap layer thickness on the strain of the nickel layer in Cu(t_{cap})/Ni(30Å)/Cu(2000Å)/Si(001) film and the effective magnetic anisotropy. The nickel strain is calculated using the Bason and Ball model (see chapter 3). The effective magnetic anisotropy is calculated using the second-order SP model.

SP Model for a fcc(111) Film

Jungblut *et. al.* had also reported out-of-plane magnetization for Cu/Ni/Cu(111) films. In this thesis, the second-order SP model has been used to describe the intrinsic magnetic anisotropy of a tetragonally distorted fcc(001) film. It would be instructive to apply it to describe a fcc(111) film. The nice thing is that all the ME coefficients can now be known *a priori* since d^2L/dr^2 has been found from the fitting of the anisotropy of the Cu/Ni/Cu/Si(001) films (see table 6.2). Thus, the excercise would

be a good test for the predictability of the second-order SP model.

Third-Order SP Model

The direct measurement of B_{11}^{eff} seems to suggest that the effect of third-order ME terms can be important in the Cu/Ni/Cu/Si(001) films. It would be interesting to develope a third-order SP model to describe the magnetic anisotropy of the nickel film. This excercise would involve carrying the Taylor expansion of the pseudodipolar coefficient — $L(r)$ — to the third order term.

Appendix A

Form of Film Anisotropy

The intrinsic magnetic anisotropy of a thin film can be viewed as composed of that of the bulk minus the missing or different bond energy at the two interfaces of the film. More specifically, suppose the film is a perfect crystal, and N_i is the number of interface atoms. The total intrinsic magnetic energy of the film can be expressed in the following way:

$$U_{film} = U_{bulk} - (N_i)(\epsilon_{interface}) \tag{A.1}$$

where U_{bulk} is the total energy assuming all the atoms are fully coordinated as those inside the film, and $\epsilon_{interface}$ is the broken bond energy per interface atom of the crystal. The energy density of the film can be found by simply dividing Eq. A.1 by the total volume of the film:

$$E_{film} = E_{bulk} - (\frac{N_i}{A})(\frac{\epsilon_{interface}}{t}) \tag{A.2}$$

where A is the area of the film, and t is the film thickness. In fact, Eq. A.2 can be written more compactly as follows:

$$E_{film} = E_{bulk} - \frac{2E_{interface}}{t} \tag{A.3}$$
$$E_{interface} \equiv \frac{N_i \epsilon_{interface}}{A}.$$

We can interpret $E_{interface}$ as the broken bond energy per unit interface area of the crystal. The factor 2 is there to account for our assumption that the film has two identical surfaces.

Thus, in this view, the 1/t dependence of the film anisotropy energy is a consequence of geometry. We can know its form a priori. There is no new physics here.

As expected, as the film thickness increases, E_{film} approaches E_{bulk}, as it should.

Eq. A.3 assumes that the $\epsilon_{interface}$ is independent of the film thickness. This may not be true since interface relaxation can be a function of the film thickness.

Appendix B

Reference State

The idea of strain depends on the reference structure from which the strain is measured. For example, consider a tetragonally distorted film. The film is said to be distorted because we are using the perfect cubic reference state to describe the mechanical state of the film. If the tetragonal state is used as the reference, the film could not be said to be distorted.

Thus, to describe thin film magnetic anisotropy, we also need to think about the reference state that we use to write the anisotropy. There are in principle an infinite number of reference states that can be used to represent a film anisotropy, but two of them seem to stand out: one is the film reference state, the other bulk reference state. In the former representation, the MC energy is the IMAE of the film; the ME energy is the extra energy needed to account for the magnetostrictive deformation. In the latter representation, the MC energy is the IMAE of the bulk structure; the ME energy is then the extra energy needed to deform from the bulk structure. The deformation can be due to intrinsic stress of the film, or the magnetostrictive stress.

The grievance with using the film reference state is that the reference state changes with film thickness. This is rather inconvenient because we would either need to have

a set of MC and ME coupling coefficients for each film thickness, or a mapping that transforms one set coupling coefficients (described in one reference state) to another set (described in a different reference state). On the other hand, in the bulk reference state, the coefficients are independent of film thicknesses. But there is a price to pay for this convenience. If the misfit strains are to be treated as a perturbation, higher order terms would need to be included for large strains ($\geq 0.1\%$).

Appendix C

Bond Direction After Deformation

In this appendix, we would like to find the transformation $\hat{\mathbf{T}}$ that maps a vector from the undeformed state to the deformed state. The deformation can be described by the following tensor:

$$(\epsilon_{ij}) = \begin{pmatrix} \epsilon_{11} & \epsilon_{12} & \epsilon_{13} \\ \epsilon_{21} & \epsilon_{22} & \epsilon_{23} \\ \epsilon_{31} & \epsilon_{32} & \epsilon_{33} \end{pmatrix} \tag{C.1}$$

Our approach to finding the transformation comes directly from the physical interpretation of the components of the strain tensor. We know that $\hat{\mathbf{T}}$ must map each of the unit vector that points along the crystal axes in the following way:

$$\hat{\mathbf{T}}\begin{pmatrix} 1 \\ 0 \\ 0 \end{pmatrix} = \begin{pmatrix} 1+\epsilon_{11} \\ \epsilon_{12} \\ \epsilon_{13} \end{pmatrix}; \quad \hat{\mathbf{T}}\begin{pmatrix} 0 \\ 1 \\ 0 \end{pmatrix} = \begin{pmatrix} \epsilon_{21} \\ 1+\epsilon_{22} \\ \epsilon_{23} \end{pmatrix}; \quad \hat{\mathbf{T}}\begin{pmatrix} 0 \\ 0 \\ 1 \end{pmatrix} = \begin{pmatrix} \epsilon_{31} \\ \epsilon_{32} \\ 1+\epsilon_{33} \end{pmatrix}$$

Thus, in this crystal axes basis set,

$$\hat{\mathbf{T}} = \begin{pmatrix} 1+\epsilon_{11} & \epsilon_{21} & \epsilon_{31} \\ \epsilon_{12} & 1+\epsilon_{22} & \epsilon_{32} \\ \epsilon_{13} & \epsilon_{23} & 1+\epsilon_{33} \end{pmatrix} \tag{C.2}$$

Thus, given any vector that is expressed in terms of the three original crystal axes, we can find where the new vector points after the deformation by a simple matrix multiplication.

Appendix D

Review of Dislocation Theory

Dislocations are defects in a crystal because they interrupt the lattice of the crystal. Unlike a point defect that distorts the lattice about a point, the distortion due to a dislocation occurs mostly about a line in the crystal. Hence, dislocations are known as line defects.

In this appendix, a review of the theory of dislocations is presented. A more in-depth treatment of the subject can be found in the textbooks by Reed-Hill and Abbaschian [1992], Hirth and Lothe [1982], and Hull and Bacon [1984]. The approach of Hull and Bacon will be followed closely. We will limit our discussion to cubic materials only. But the idea can be easily generalized to other crystal lattices.

D.1 Geometry of Dislocations

The two basic types of dislocations are edge and screw dislocations. An edge dislocation can be simulated by inserting an extra half plane — labeled ABCD in figure D.1 — in an otherwise perfect crystal. This extra plane distorts the lattice, particularly in the vicinity of the line DC. The line DC is a positive edge dislocation, denoted

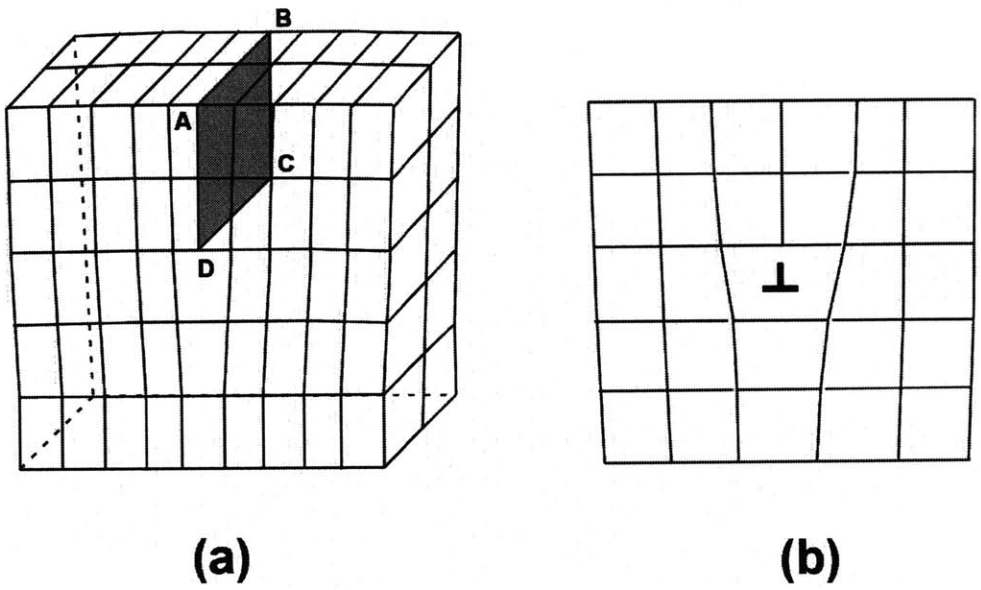

Figure D.1: Model of an edge dislocation in a simple cubic crystal; a) a simulation of an edge dislocation by inserting an extra half plane (ABCD) into the lattice; b) a cross-section of the lattice viewed in the DC direction.

by the symbol $\perp$. The word *positive* is to convey that the extra half plane is in the upper part of the lattice. Needless to say, if the extra half plane was inserted into the bottom half of the lattice, it would be a negative edge dislocation, denoted by the symbol $\top$.

A screw dislocation can be simulated by displacing the upper atoms in one side of the lattice plane ABCD relative to those in the other in the AB direction, as shown in figure D.2a. Note that the atoms below the plane ABCD are not displaced in the maneuver. Figure D.2b displays the arrangement of atoms above and below the plane ABCD. A close look shows that the atoms form a spiral network around the line DC (see figure D.2c), and hence the name *screw* is used in describing this type of dislocation. Further, this is a left-handed screw. The reason is that as the helix

advances one atomic distance once a counter-clockwise circuit is made around it.

In general, most dislocations are a mixture of edge and screw. An example of a mixed dislocation is shown in figure D.3. The dislocation changes from an edge to a screw along the line DF.

D.2 Evidence for Dislocations

From a thermodynamics viewpoint, point defects must exist in a bulk crystal above 0°K because of the necessary balance between the internal energy and entropy of the system. Since dislocations costs much more energy in comparison with the increase in entropy they produce, their presence in bulk crystal must necessarily a non-equilibrium phenomenon. However, in epitaxial films, dislocations are necessary in order for the film to relieve the strain energy due to the lattice mismatch between the film and its substrate, as discussed in chapter 3.

The existence of dislocations in bulk crystal was first postulated in 1934 independently by Orowan, Polyani, and Taylor in an effort to explain the low-yield shear stress than that was predicted by the elastic theory. In the absence of dislocations, an applied shear stress can distort the crystal by having *all* atoms in each atomic planes slide over those in its neighboring lattice planes as shown in figure D.4. This would require a large critical shear stress to plastically (i.e., irreversibly) distort the crystal. The calculated shear stress is orders of magnitude larger than what was observed experimentally.

With dislocations, the crystal can respond to shear stress by simply moving a small number of atoms at a time. Figure D.5 shows how an edge dislocations can glide in response to an applied shear stress.

With transmission electron microscope, dislocation lines can now be observed more

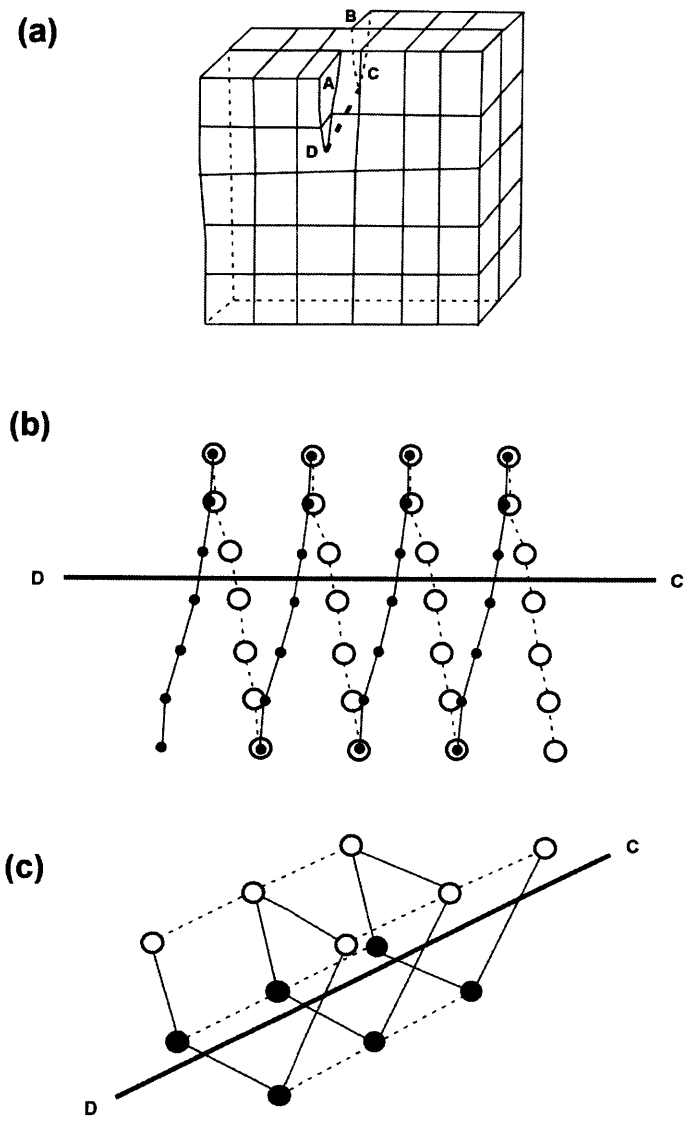

Figure D.2: Model of a screw dislocation in simple cubic crystal; a) A simulation of a screw dislocation by displacing the upper atoms in one side of the ABCD plane relative to those in the other side along the AB direction; b) A 3-dimensional view of the arrangement of atoms above and below the lattice plane ABCD; filled circles are atoms above the plane; open circles are atoms below. b) A close view of the spiral arrangements of atoms about the DC axis (after Hull and Bacon, 1984, p. 18 and p. 52).

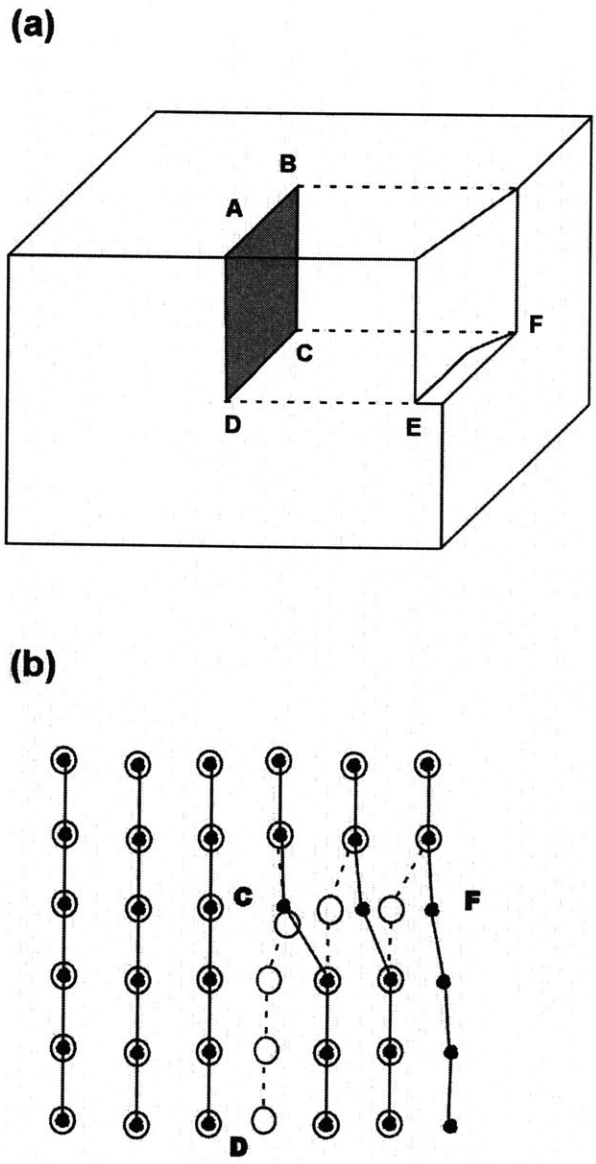

Figure D.3: Model of a mixed dislocation in simple cubic crystals; a) A simulation of a mixed dislocation; DC is an edge dislocation; CF is a screw dislocation; the two dislocation meets at the corner C; the line DF is a mixture of an edge and a screw; b) A top view of the mixed dislocation (after Reed-Hill and Abbaschian, 1992, pp. 98-99).

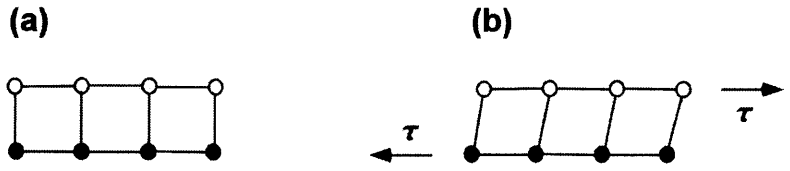

Figure D.4: Shear stress in the absence of dislocations; a) without the applied shear stress; b) with the applied shear stress.

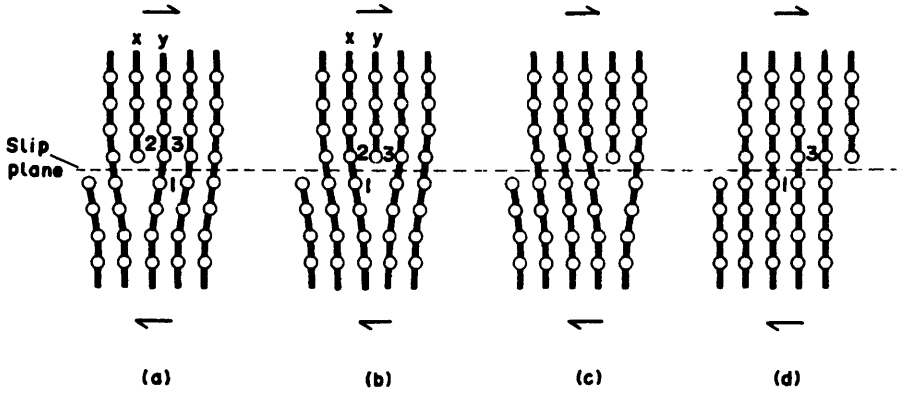

Figure D.5: Illustration of the gliding process: the arrows indicate the applied shear stress (after Hull and Bacon, 1984,p. 50).

directly. The image contrast is possible because the localized atomic displacement and elastic strain field are very large in the vicinity of a dislocation. For readers who are interested in this technology, a good reference book on the subject is by Williams and Carter [1996].

However, the original source of dislocations in bulk crystals is still not clearly established [Kingergy *et. al.* , 1992, p. 166]. Dislocations may be introduced during the growth process by thermal stresses, mechanical stresses, precipitation of vacancies during cooling, and growth over second-phase particles. In thin epitaxial films, the source can also be due to the difference in the lattice constants between the film and the substrate on which the film is grown.

D.3 Slip Planes

Slip planes are planes that dislocations can glide. They are usually the ones that have the most number of bonds in the planes. This is expected because dislocations can glide on these planes with the least amount of shear stress field. In simple cubic crystal, the slip planes are {100}. In face-center cubic (fcc) crystal, they are the {111} set of planes.

In fact, the concepts of dislocations and slip planes are linked in a fundamental way. A dislocation can be defined as a line that forms a boundary on a slip plane between a region that has slipped and one that has not [Reed-Hill and Abbaschian, 1992, p. 94]. In figure D.1 and D.2, the dislocation lines are DC. In figure D.3, it is DF.

D.4 Burgers Vector

Burgers vector is an important characterization of a dislocation. It conveys the information about the magnitude and direction of the slip. The Burgers vector is defined in reference to the Burgers circuit. A Burgers circuit is any atom-to-atom closed path taken in a crystal that enclosed a dislocation. The procedure that can be used to find the Burgers vector of any dislocation is the following:

i) Choose a unit vector $\hat{\zeta}$ that points along the dislocation line.

ii) Make a right-hand Burgers circuit that contains the dislocation; that is, the thumb of the right hand points in the direction of $\hat{\zeta}$.

iii) The same circuit (namely the same atom-to-atom sequence) is made in a dislocation free crystal. The vector that is needed to complete the circuit in the perfect crystal is the Burgers vector of the enclosed dislocation, denoted as $\vec{b}$.

Figure D.6 and D.7 show the Burgers circuits and vectors of an edge and screw dislocations. Note that the Burgers vector $\vec{b}$ of the edge dislocation is perpendicular to the dislocation line; it is parallel to the dislocation line for the screw dislocation.

D.5 Dislocation Density

The concentration of dislocations is measured by the number of dislocation lines that intersect a unit area. A careful prepared crystal may contain 10^2 dislocation lines per square centimeter. A heavily plastically deformed crystal may contain up to 10^{10} to 10^{11} dislocation lines per square centimeter [Kingery, 1976, p. 167].

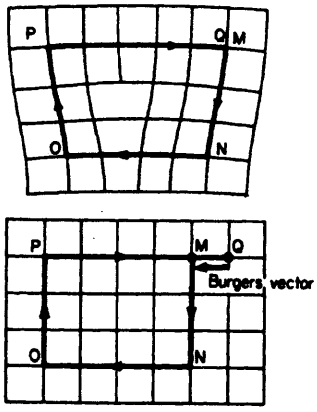

Figure D.6: Burgers vector in an edge dislocation (after Hull and Bacon, 1984, p. 19).

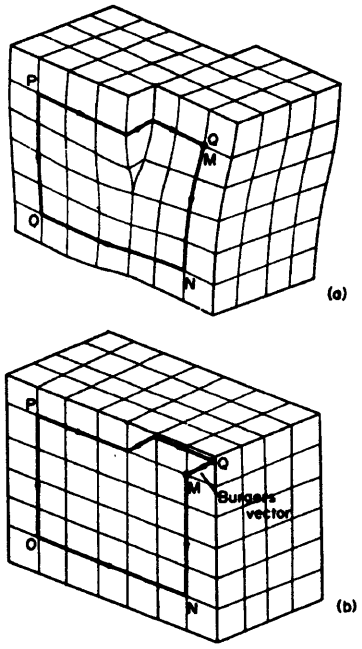

Figure D.7: Burgers vector in a screw dislocation (after Hull and Bacon, 1984, p. 20).

D.6 Stress Field of a Dislocation

Using a continuum model, the stress field of a dislocation can be obtained. In the appendix, we will just cite the results. The derivations can be found in the book by Hirth and Lothe [1992].

Consider a screwed dislocation shown in figure D.8. In the cylindrical coordinate system, the shear component of the stress field is

$$\sigma_{\theta z} = \sigma_{z\theta} = \frac{Gb}{2\pi r} \tag{D.1}$$

where b = the magnitude of the Burgers vector, and G is the shear modulus of the material. All the other components (both the shear and normal stress field) are zero.

Observe that the stress field is symmetric about the dislocation, as expected. Further, the shear component σ_{thetaz} varies inversely with the distance from the dislocation. Note that the stress goes to infinity at the dislocation. This singularity is unrealistic in a solid; thus, a hole of radius r_o is drawn in figure D.8 to exclude it from the material. The diameter of the hole is usually taken to be about the length of the Burgers vector b. The hole is generally referred to the core of the dislocation.

The strain field of the edge dislocation can be found by simply using the stress-strain relation:

$$e_{\theta z} = e_{z\theta} = \frac{b}{4\pi r} \tag{D.2}$$

For an edge dislocation, the stress field is more complicated due to the asymmetry of the problem. Figure D.9 shows an edge dislocation and a representation of it using an isotropic cylinder. Linear elasticity theory can then be used to find the stress field:

$$\sigma_{xx} = -Dy\frac{3x^2 + y^2}{(x^2 + y^2)^2},$$

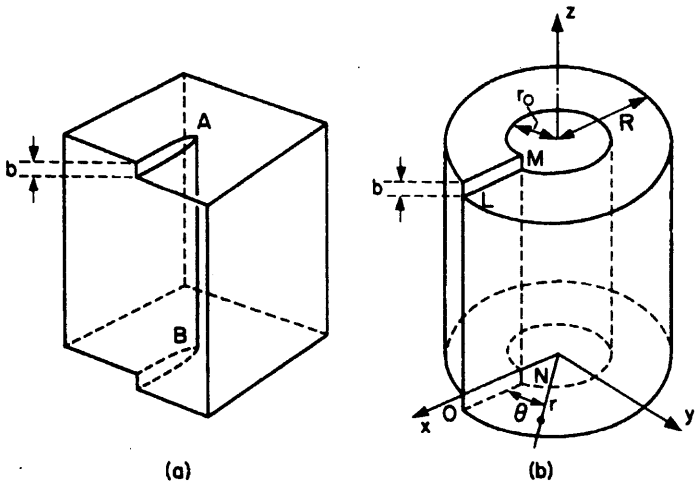

Figure D.8: (a) screw dislocation; (b) Cylindrical representation of the screw dislocation. (after Hull and Bacon, 1984, p. 75).

$$\begin{aligned} \sigma_{yy} &= Dy\frac{x^2-y^2}{(x^2+y^2)^2}, \\ \sigma_{xy} &= \sigma_{yx} = Dx\frac{x^2-y^2}{(x^2+y^2)^2}, \\ \sigma_{zz} &= \nu(\sigma_{xx}+\sigma_{yy}), \\ \sigma_{xz} &= \sigma_{zx} = \sigma_{yz} = \sigma_{zy} = 0, \\ \text{where} \quad D &= \frac{Gb}{2\pi(1-\nu)}. \end{aligned} \tag{D.3}$$

Here, ν is the Poisson's ratio of the material. Note that the stress field goes to infinity at the dislocation. Thus, a hole is drawn in figure D.9 to exclude to singularity.

The strain field can be found using the stress-strain relation.

The stress field of a mixed dislocation can be obtained by superpositioning the appropriate edge and screw component of the dislocation. This method is possible because of the linearity of the theory.

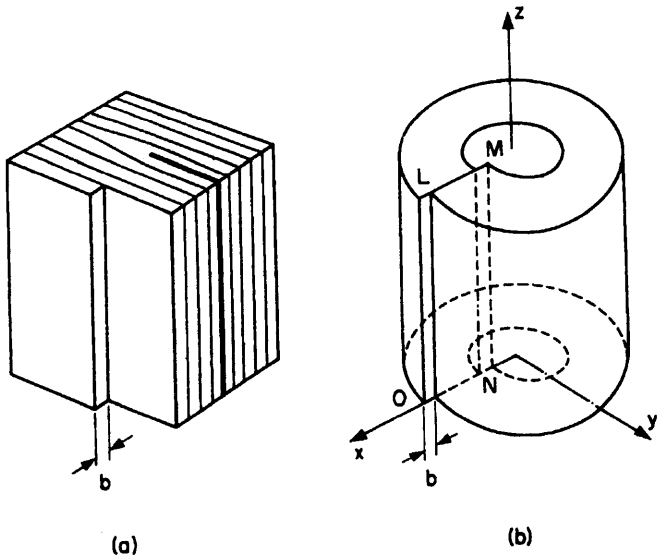

Figure D.9: (a) Edge dislocation; (b) Cylindrical representation of the edge dislocation. (after Hull and Bacon, 1984, p. 77).

D.7 Dislocation Energy

The energy E_d of a dislocation can be decomposed of two parts:

$$E_d = E_{core} + E_{el} \tag{D.4}$$

where E_{core} is the excess energy needed to create the core from a perfect crystal, and E_{el} is the elastic energy due to the distortion introduced by the dislocation outside the core area. The energy of the core can be found using the following equation:

$$E_{el} = \int (\sum \sigma_{ij} e_{ij}) dV \tag{D.5}$$

From the previous section, we have the stress and strain field of an edge and a screw dislocation. Thus, their elastic energies per unit length of dislocation are:

$$E_{el} = \frac{Gb^2}{4\pi} \mathrm{Log}_e \left(\frac{r}{r_o} \right) \qquad \text{(screw)} \tag{D.6}$$

$$E_{el} = \frac{Gb^2}{4\pi(1-\nu)} \mathrm{Log}_e \left(\frac{r}{r_o} \right) \qquad \text{(edge)} \tag{D.7}$$

where r is the distance from the dislocation, and r_o (as mentioned before) is the core of the dislocation.

Note that for both the edge and screw dislocation, their elastic energies are proportional to b^2. Thus, dislocations that have the shortest Burgers vector generally prevail.

It is common to incorporate the core energy mathematically into the elastic term by introducing an α parameter:

$$E_d = \frac{Gb^2}{4\pi} \mathrm{Log}_e \left(\frac{\alpha r}{r_o} \right) \qquad \text{(screw)} \tag{D.8}$$

$$E_d = \frac{Gb^2}{4\pi(1-\nu)} \mathrm{Log}_e\left(\frac{\alpha r}{r_\circ}\right) \qquad \text{(edge)} \qquad \text{(D.9)}$$

The value for α is different for different material. For a diamond cubic crystal, α is about 4; for a metal, it can range from 0.5 to 2 [Hirth and Lothe, 1992, p. 231].

The dislocation energy of a mixed dislocation can be found by summing the energy due to the screw and edge component of the dislocation:

$$E_d = \frac{Gb^2(1-\nu\cos^2\beta)}{4\pi(1-\nu)} \mathrm{Log}_e\left(\frac{\alpha r}{r_\circ}\right) \qquad \text{(mixed)} \qquad \text{(D.10)}$$

where β is the angle between the Burgers vector and the dislocation line.

Appendix E

Magnetostrictive Stresses in Films

It is more natural to discuss magnetostrictive stresses than strains in a thin film for several reasons: i) magnetostrictive stresses are generally more directly measurable in a thin film (e.g., by the cantilever beam method); ii) even if magnetostrictive strains are measured directly, they are not the true magnetostrictions because of the constraint imposed by the substrate on which the film is grown; iii) magnetostrictive stresses are more intrinsic properties of the film in that unlike magnetostrictive strains, they do not depend on the mechanical properties of the substrate (such as Young modulus) and and its thickness. A brief discussion of magnetostriction with and without constraints is presented in appendix F.

In this appendix, the magnetostrictive stress tensor of a thin film is derived. The strategy is the following: The free energy (magnetoelastic plus strain energy) is first minimized with respect to strain. A set of equilibrium magnetostrictive strains is obtained. These are free magnetostrictive strains (namely, they are calculated in the absence of the constraint imposed by the substrate). The strain-stress constitutive relation is then used to find the corresponding stresses.

For concreteness, the magnetostrictive stresses of a tetragonally distorted cubic

(001) film is derived. The free energy of the film (including the strain energy) is

$$\begin{aligned} F_{film} &= K_s^{eff}\alpha_3^2 + B_{11}^{eff}[\epsilon_{11}(\alpha_1^2 - \frac{1}{3}) + \epsilon_{22}(\alpha_2 - \frac{1}{3})] + B_{12}^{eff}[\epsilon_{33}(\alpha_3^2 - \frac{1}{3})] \\ &+B_{13}^{eff}[\epsilon_{11}(\alpha_2^2 - \frac{1}{3}) + \epsilon_{22}(\alpha_1^2 - \frac{1}{3})] + B_{21}^{eff}[\alpha_1\alpha_2\epsilon_{12}] \\ &+B_{22}^{eff}[\alpha_1\alpha_3\epsilon_{13} + \alpha_2\alpha_3\epsilon_{23}] + D_{rs}^{eff}[e_0(\alpha_3^2 - \frac{1}{3})] + \frac{c_{11}}{2}[\epsilon_{11}^2 + \epsilon_{22}^2 + \epsilon_{33}^2] \\ &+c_{12}[\epsilon_{11}\epsilon_{22} + \epsilon_{22}\epsilon_{33} + \epsilon_{33}\epsilon_{11}] + \frac{c_{44}}{2}[\epsilon_{23}^2 + \epsilon_{13}^2 + \epsilon_{12}^2] \end{aligned} \tag{E.1}$$

where Eq. 2.22 is used to express the magnetic free energy. The strain energy density is assumed to be that of a cubic material. The magnetostrictive strains of a thin film can be found by minimizing the free energy with respect to the ϵ_{ij}:

$$\begin{aligned} \epsilon_{11} &= \frac{[c_{12}B_{13}^{eff} - B_{11}^{eff}(c_{11}+c_{12})][\alpha_1^2 - \frac{1}{3}]}{(c_{11}-c_{12})(c_{11}+2c_{12})} \\ &+\frac{[c_{12}B_{11}^{eff} - B_{13}^{eff}(c_{11}+c_{12})][\alpha_2^2 - \frac{1}{3}] + c_{12}B_{12}^{eff}[\alpha_3^2 - \frac{1}{3}]}{(c_{11}-c_{12})(c_{11}+2c_{12})} \\ \epsilon_{22} &= \frac{[c_{12}B_{11}^{eff} - B_{13}^{eff}(c_{11}+c_{12})][\alpha_1^2 - \frac{1}{3}]}{(c_{11}-c_{12})(c_{11}+2c_{12})} \\ &+\frac{[c_{12}B_{13}^{eff} - B_{11}^{eff}(c_{11}+c_{12})][\alpha_2^2 - \frac{1}{3}] + c_{12}B_{12}^{eff}[\alpha_3^2 - \frac{1}{3}]}{(c_{11}-c_{12})(c_{11}+2c_{12})} \\ \epsilon_{33} &= -\frac{c_{12}B_{11}^{eff} + B_{12}^{eff}(c_{11}+c_{12}) + c_{12}B_{13}^{eff}}{(c_{11}-c_{12})(c_{11}+2c_{12})}[\alpha_3^2 - \frac{1}{3}] \\ \epsilon_{12} &= -\frac{B_{21}^{eff}}{c_{44}}\alpha_1\alpha_2 \\ \epsilon_{13} &= -\frac{B_{22}^{eff}}{c_{44}}\alpha_1\alpha_3 \\ \epsilon_{23} &= -\frac{B_{22}^{eff}}{c_{44}}\alpha_2\alpha_3 \end{aligned} \tag{E.2}$$

Using the following stress-strain constitutive relation,

$$\begin{pmatrix} \sigma_{11} \\ \sigma_{22} \\ \sigma_{33} \\ \sigma_{12} \\ \sigma_{13} \\ \sigma_{23} \end{pmatrix} = \begin{pmatrix} c_{11} & c_{12} & c_{12} & & & \\ c_{12} & c_{11} & c_{12} & & & \\ c_{12} & c_{12} & c_{11} & & & \\ & & & c_{44} & & \\ & & & & c_{44} & \\ & & & & & c_{44} \end{pmatrix} \begin{pmatrix} \epsilon_{11} \\ \epsilon_{22} \\ \epsilon_{33} \\ \epsilon_{12} \\ \epsilon_{13} \\ \epsilon_{23} \end{pmatrix} \tag{E.3}$$

the corresponding magnetostrictive stress tensor is obtained:

$$(\sigma_{ij}) = -\begin{pmatrix} B_{11}^{eff}(\alpha_1^2 - \frac{1}{3}) + B_{13}^{eff}(\alpha_2^2 - \frac{1}{3}) & B_{21}^{eff}\alpha_1\alpha_2 & B_{22}^{eff}\alpha_3\alpha_1 \\ B_{21}^{eff}\alpha_1\alpha_2 & B_{11}^{eff}(\alpha_2^2 - \frac{1}{3}) + B_{13}^{eff}(\alpha_1^2 - \frac{1}{3}) & B_{22}^{eff}\alpha_2\alpha_3 \\ B_{22}^{eff}\alpha_3\alpha_1 & B_{22}^{eff}\alpha_2\alpha_3 & B_{12}^{eff}(\alpha_3^2 - \frac{1}{3}). \end{pmatrix}$$

The traction force measured along the $[\beta_1, \beta_2, \beta_3]$ direction is then

$$\begin{aligned} \sigma(\beta_1, \beta_2, \beta_3) \;=\; & -\beta_1^2[B_{11}^{eff}(\alpha_1^2 - \frac{1}{3}) + B_{13}^{eff}(\alpha_2^2 - \frac{1}{3})] \\ & -\beta_2^2[B_{11}^{eff}(\alpha_2^2 - \frac{1}{3}) + B_{13}^{eff}(\alpha_1^2 - \frac{1}{3})] - \beta_3^2[B_{12}^{eff}(\alpha_3^2 - \frac{1}{3})] \\ & -B_{21}^{eff}[\beta_1\beta_2\alpha_1\alpha_2] - B_{22}^{eff}[\beta_2\beta_3\alpha_2\alpha_3 + \beta_3\beta_1\alpha_3\alpha_1]. \end{aligned} \tag{E.4}$$

Appendix F

Magnetostriction With/Without Constraints

In this appendix, magnetostrictive strains (or magnetostrictions) of a cubic material are derived with and without constraints. Although magnetostriction is not discussed in this thesis, the discussion is included for completeness.

F.1 Magnetostriction Without Constraints

The free magnetostrictive strains can be obtained by minimizing the free energy of the system with respect to ϵ_{ij}. The relevant contribution to the free energy is the volume magnetic anisotropy energy plus the elastic energy. For a bulk unconstrained cubic material (Chikazumi, 1996, p. 351),

$$\begin{aligned} F_{bulk} &= K_0 + K_1[\alpha_1^2\alpha_2^2 + \alpha_2^2\alpha_3^2 + \alpha_3^2\alpha_1^2] \\ &\quad + B_1[\epsilon_{11}(\alpha_1^2 - \frac{1}{3}) + \epsilon_{22}(\alpha_2^2 - \frac{1}{3}) + \epsilon_{33}(\alpha_3^2 - \frac{1}{3})] \end{aligned} \tag{F.1}$$

$$+B_2[\epsilon_{12}\alpha_1\alpha_2 + \epsilon_{23}\alpha_2\alpha_3 + \epsilon_{31}\alpha_3\alpha_1] + \frac{1}{2}c_{11}[\epsilon_{11}^2 + \epsilon_{22}^2 + \epsilon_{33}^2]$$
$$+c_{12}[\epsilon_{11}\epsilon_{22} + \epsilon_{22}\epsilon_{33} + \epsilon_{33}\epsilon_{11}] + \frac{1}{2}c_{44}[\epsilon_{12}^2 + \epsilon_{13}^2 + \epsilon_{23}^2]$$

The equations that relate the components of the magnetostrictive strains to the direction cosines of the magnetization (namely, α_i) can be found by setting $\partial F_{bulk}/\partial\epsilon_{ij} = 0$:

$$\begin{aligned}
\frac{\partial F_{bulk}}{\partial \epsilon_{11}} &= B_1(\alpha_1^2 - \frac{1}{3}) + c_{11}\epsilon_{11} + c_{12}(\epsilon_{22} + \epsilon_{33}) = 0, \\
\frac{\partial F_{bulk}}{\partial \epsilon_{22}} &= B_1(\alpha_2^2 - \frac{1}{3}) + c_{11}\epsilon_{22} + c_{12}(\epsilon_{11} + \epsilon_{33}) = 0, \\
\frac{\partial F_{bulk}}{\partial \epsilon_{33}} &= B_1(\alpha_3^2 - \frac{1}{3}) + c_{11}\epsilon_{33} + c_{12}(\epsilon_{11} + \epsilon_{22}) = 0, \\
\frac{\partial F_{bulk}}{\partial \epsilon_{12}} &= B_2\alpha_1\alpha_2 + c_{44}\epsilon_{12} = 0, \\
\frac{\partial F_{bulk}}{\partial \epsilon_{23}} &= B_2\alpha_2\alpha_3 + c_{44}\epsilon_{23} = 0, \\
\frac{\partial F_{bulk}}{\partial \epsilon_{13}} &= B_2\alpha_3\alpha_1 + c_{44}\epsilon_{13} = 0.
\end{aligned} \tag{F.2}$$

Solving these equations, we get the equilibrium strain tensor:

$$(\epsilon_{ij}) = \begin{pmatrix} \frac{-B_1}{c_{11}-c_{12}}(\alpha_1^2 - \frac{1}{3}) & \frac{-B_2}{c_{44}}\alpha_1\alpha_2 & \frac{-B_2}{c_{44}}\alpha_3\alpha_1 \\ \frac{-B_2}{c_{44}}\alpha_1\alpha_2 & \frac{-B_1}{c_{11}-c_{12}}(\alpha_2^2 - \frac{1}{3}) & \frac{-B_2}{c_{44}}\alpha_2\alpha_3 \\ \frac{-B_2}{c_{44}}\alpha_3\alpha_1 & \frac{-B_2}{c_{44}}\alpha_2\alpha_3 & \frac{-B_1}{c_{11}-c_{12}}(\alpha_3^2 - \frac{1}{3}) \end{pmatrix} \tag{F.3}$$

Because the trace of $(\epsilon_{ij}) = 0$, the volumetric magnetostriction is zero.

The strain measured in the direction $[\beta_1, \beta_2, \beta_3]$ can be expressed as follows:

$$\lambda(\beta_1, \beta_2, \beta_3) = \epsilon_{11}\beta_1^2 + \epsilon_{22}\beta_2^2 + \epsilon_{33}\beta_3^2 + \epsilon_{12}\beta_1\beta_2 + \epsilon_{23}\beta_2\beta_3 + \epsilon_{13}\beta_1\beta_3$$

$$= \frac{-B_1}{c_{11}-c_{12}}(\alpha_1^2\beta_1^2+\alpha_2^2\beta_2^2+\alpha_3^2\beta_3^2-\frac{1}{3}) + \frac{-B_2}{c_{44}}(\alpha_1\alpha_2\beta_1\beta_2+\alpha_2\alpha_3\beta_2\beta_3+\alpha_3\alpha_1\beta_3\beta_1) \quad \text{(F.4)}$$

Note that if the crystal is magnetized along [100], the strain observed in the same direction is calculated to be

$$\lambda_{100}(1,0,0) = -\frac{2}{3}\frac{B_1}{c_{11}-c_{12}} \equiv \lambda_{100} \quad \text{(F.5)}$$

Similarly, if the magnetization is along [111], then the strain observed along the same direction is

$$\lambda_{111}(\frac{1}{\sqrt{3}},\frac{1}{\sqrt{3}},\frac{1}{\sqrt{3}}) = -\frac{1}{3}\frac{B_2}{c_{44}} \equiv \lambda_{111} \quad \text{(F.6)}$$

Thus, Eq. (F.4) can be rewritten in terms of λ_{100} and λ_{111} as follows:

$$\lambda(\beta_1,\beta_2,\beta_3) = \frac{3}{2}\lambda_{100}(\alpha_1^2\beta_1^2+\alpha_2^2\beta_2^2+\alpha_3^2\beta_3^2-\frac{1}{3}) + 3\lambda_{111}(\alpha_1\alpha_2\beta_1\beta_2+\alpha_2\alpha_3\beta_2\beta_3+\alpha_3\alpha_1\beta_3\beta_1) \quad \text{(F.7)}$$

Eq. (F.7) is known as the "two-constant" equation for bulk cubic magnetostriction. This is because any magnetostrictive strain in a cubic material, according to the theory, can be expressed as a linear combination of just λ_{100} and λ_{111}. The two constants reflect the consequence of our picking of only two coefficients B_1 and B_2 to characterize the coupling. Of course, we could have included higher-order terms in our description. The next approximation in fact involves five constants, but the model is rarely used in the literature (Cullity, 1972, p. 253).

F.1.1 Measurement Procedures

In writing the free energy density, we have used the cubic reference state, and any magnetostrictive strain is measured with respect to this reference state. But the undistorted cubic state, a state in which there are no magnetic interactions to deform the cubic crystal, is not experimentally realizable in a ferromagnet below its Curie temperature. This poses a serious problem: how can a strain be measured without knowing what it is that it is strained from?

There are two solutions to this problem. One is to find another state which can be obtained experimentally and has the same shape and volume as the undeformed state. This condition can be realized only if the material is cut into a perfect sphere in which all possible domains have equal volumes — complete demagnetization. Oftentimes, only partial demagnetization is obtained due to the biasing by magnetostatic field.

The other solution is to make two independent strain measurements and then take their difference to — so to speak — subtract out the common reference point. This is the usual method used in the literature to measure the magnetostrictive strains. Here is the procedure for measuring λ_{100}: We first magnetize the crystal say along the [100] and measure the strain in the same direction. Then we magnetize the crystal in say the [010] but still measure the strain in the [100]. The difference in the two strain measurements from Eq. (F.4) gives

$$\lambda_{100}(100) - \lambda_{010}(100) = \frac{3}{2}\lambda_{100} \tag{F.8}$$

Similarly, to measure λ_{111}, we first magnetize the sample along the [111] and measure the strain in the same direction. Then we magnetize the crystal in say $[\bar{1}11]$ and measure the strain again in the [111]. The difference in the two strain measurements gives

$$\lambda_{111}(111) - \lambda_{\bar{1}11}(111) = \frac{4}{3}\lambda_{111} \tag{F.9}$$

To give some numbers, for bulk bcc iron, λ_{100} = 20.7 $\times 10^{-6}$, and λ_{111} = -21.2 $\times 10^{-6}$; for bulk fcc nickel, λ_{100} = -45.9 $\times 10^{-6}$, and λ_{111} = -24.3 $\times 10^{-6}$ [Chikazumi, 1997, p. 361].

F.2 Magnetostriction With Constraints

So far, we have described the magnetostriction of a cubic material which is free of any physical constraints imposed by its surroundings. In some cases, the effects of the surroundings cannot be neglected. A good example is the magnetostriction of a thin film that is grown on a substrate. Obviously, the presence of the substrate would prevent the film from being fully strained under an external magnetic field.

There are many kinds of constraints that can be imposed on a material. Here, we will consider only one type to illustrate the concept: the crystal is not allowed to strain in the [100] direction but is free to move along the [010] and [001]. The question is, "How then does the system deform with respect to various magnetization directions?"

Certainly, the free energy density (Eq. F.1) for the unconstrained case is still valid here because the walls do not change the underlying physics of the problem. What is different, though, is that the crystal is no longer free to deform however it chooses to minimize the free energy: it must seek the minimum energy configuration under the condition that $\epsilon_{11} = \epsilon_{12} = \epsilon_{13} = 0$. Thus, the equations of equilibrium are

$$\frac{\partial F_{bulk}}{\partial \epsilon_{22}} = B_1(\alpha_2^2 - \frac{1}{3}) + c_{11}\epsilon_{22} + c_{12}\epsilon_{33} = 0,$$

$$\begin{aligned}\frac{\partial F_{bulk}}{\partial \epsilon_{33}} &= B_1(\alpha_3^2 - \frac{1}{3}) + c_{11}\epsilon_{33} + c_{12}\epsilon_{22} = 0, \\ \frac{\partial F_{bulk}}{\partial \epsilon_{23}} &= B_2\alpha_2\alpha_3 + c_{44}\epsilon_{23} = 0.\end{aligned} \tag{F.10}$$

Solving these equations, we get the equilibrium strain tensor:

$$(\epsilon_{ij}) = \begin{pmatrix} 0 & 0 & 0 \\ 0 & -B_1\frac{c_{11}(\alpha_2^2-\frac{1}{3})-c_{12}(\alpha_3^2-\frac{1}{3})}{(c_{11}-c_{12})(c_{11}+c_{12})} & -\frac{B_2}{c_{44}}\alpha_2\alpha_3 \\ 0 & -\frac{B_2}{c_{44}}\alpha_2\alpha_3 & -B_1\frac{c_{12}(\alpha_2^2-\frac{1}{3})-c_{11}(\alpha_3^2-\frac{1}{3})}{(c_{11}-c_{12})(c_{11}+c_{12})} \end{pmatrix} \tag{F.11}$$

Note that the trace of (ϵ_{ij}) is no longer zero; the presence of the walls introduces volumetric strain which, as we shall see, is a consequence of the superposition of magnetostrictive and mechanical strains.

As before, the strain in the direction of $(\beta_1, \beta_2, \beta_3)$ can be written as follows:

$$\begin{aligned}\lambda(\beta_1,\beta_2,\beta_3) &= \epsilon_{11}\beta_1^2 + \epsilon_{22}\beta_2^2 + \epsilon_{33}\beta_3^2 + \epsilon_{12}\beta_1\beta_2 + \epsilon_{23}\beta_2\beta_3 + \epsilon_{31}\beta_3\beta_1 \\ &= \frac{-B_1}{(c_{11}+c_{12})(c_{11}-c_{12})}(c_{11}(\alpha_2^2-\frac{1}{3}) - c_{12}(\alpha_3^2-\frac{1}{3}))\beta_2^2 \\ &\quad + \frac{-B_1}{(c_{11}+c_{12})(c_{11}-c_{12})}(c_{12}(\alpha_2^2-\frac{1}{3}) - c_{11}(\alpha_3^2-\frac{1}{3}))\beta_3^2 \\ &\quad + \frac{-B_2}{c_{44}}\alpha_2\alpha_3\beta_2\beta_3\end{aligned} \tag{F.12}$$

A few key observations are worth mentioning:

a) $\lambda(1,0,0) = 0$. Thus, as expected, the strain along the [1,0,0] direction is zero by assumption regardless of the direction in which where the magnetization vector points.

b) If the crystal is magnetized along the [010] direction, the strain observed in the same direction is calculated to be

$$\lambda_{010}(010) = -\frac{1}{3}\frac{B_1}{(c_{11}+c_{12})(c_{11}-c_{12})}(2c_{11}+c_{12}) \tag{F.13}$$

Comparing this to the magnetostriction in the [100] without the constraint, we have

$$0.5 < \frac{\lambda_{010}(010)}{\lambda_{010}(010)} = \frac{1}{2}\frac{2c_{11}+c_{12}}{c_{11}+c_{12}} < 1. \tag{F.14}$$

Note that the ratio of $\lambda_{010}(010)$ and $\lambda_{100}(010)$ is always a positive number since the elastic moduli are always positive for transition metals and their alloys. Furthermore, this ratio is bounded between 0.5 to 1. Thus, it is harder for the crystal to strain magnetostrictively if one of its crystallographic axes is fixed. How much harder? For fcc nickel, the ratio is

$$\frac{\lambda_{010}(010)}{\lambda_{100}(010)} = \frac{1}{2}\frac{(2)(2.5)+1.6}{2.5+1.6} = 0.8. \tag{F.15}$$

c) If the constrained crystal is magnetized in the [100] direction, the strain observed in the [010] direction is given by

$$\lambda_{010}(100) = \frac{1}{3}\frac{B_1}{(c_{11}+c_{12})} \tag{F.16}$$

Again, comparing it with the magnetostriction in the [010] without the constraint, we have

$$0 < \frac{\lambda_{010}(100)}{\lambda_{010}(100)} = \frac{c_{11}-c_{12}}{c_{11}+c_{12}} < 1. \tag{F.17}$$

Because the elastic moduli are positive and $c_{11} > c_{12}$ for transition metals and their alloys [1], the ratio of $\lambda_{010}(100)$ and $\lambda_{010}(100)$ is always a positive number. Furthermore, since it is bounded between 0 and 1, the material cannot be fully strained because one of its crystallographic direction is held fixed. For nickel, the ratio is

[1]For stability reason, $c_{11} > \|c_{12}\|$ (see Nye, 1990, p. 142 for an explanation.)

$$\frac{\lambda_{010}(100)}{\lambda_{010}(100)} = \frac{2.5 - 1.6}{2.5 + 1.6} = 0.22. \tag{F.18}$$

The constraint problem can be solved in a different way. Here is the idea: We know that the net effect of a constraint is to apply an external force(s) to the freely strained system. Because this is a linear theory, the magnetostrictive and mechanical strains can be solved independently. The concept is illustrated by doing an example. More specifically, we will redo the problem mentioned in observation c) from the previous page by this alternative method.

Since the crystal is magnetized in the [100] direction, the magnetostrictive strain tensor of the *unconstrained* sample is given by

$$(\epsilon_{ij}) = \begin{pmatrix} \frac{2}{3}\frac{B_1}{c_{11}-c_{12}} & 0 & 0 \\ 0 & \frac{1}{3}\frac{B_1}{c_{11}-c_{12}} & 0 \\ 0 & 0 & \frac{1}{3}\frac{B_1}{c_{11}-c_{12}} \end{pmatrix} \tag{F.19}$$

Since the assumed constraints prevent the crystal from being strained in the [100] direction, they must effectively apply a force to the crystal to undo some of the magnetostrictive strains. The needed stresses can be found by converting the magnetostrictive strains to stresses via the stress-strain constitutive relation. For a cubic material, the constitutive relation is

$$\begin{aligned} \sigma_{11} &= c_{11}\epsilon_{11} + c_{12}(\epsilon_{22} + \epsilon_{33}) \\ \sigma_{22} &= c_{11}\epsilon_{22} + c_{12}(\epsilon_{11} + \epsilon_{33}) \\ \sigma_{33} &= c_{11}\epsilon_{33} + c_{12}(\epsilon_{11} + \epsilon_{22}) \end{aligned} \tag{F.20}$$

We know that $\epsilon_{22} = \epsilon_{33}$ because of the symmetry of the constraint. Furthermore, σ_{22} and σ_{33} are also equal to zero because there are no applied forces in the [010] and

[001] directions. Thus, with three equations and three unknowns (namely, ϵ_{22}, ϵ_{33}, and σ_{11}), we can solve for the unknowns:

$$\epsilon_{33} = -\frac{2}{3} B_1 \frac{c_{12}}{(c_{11} - c_{12})(c_{11} + c_{12})} \tag{F.21}$$

Adding the mechanical and the magnetostrictive strain, we get

$$\lambda_{010}(100) = \frac{1}{3}\frac{B_1}{c_{11} - c_{12}} - \frac{2}{3} B_1 \frac{c_{12}}{(c_{11} - c_{12})(c_{11} + c_{12})} = \frac{1}{3}\frac{B_1}{c_{11} + c_{12}} \tag{F.22}$$

This solution is exactly the same as the one we got by minimizing the free energy subject to the constraint (Eq. F.16).

References

P. Bai, G. Yang, L. You, T. Lu, and D. B. Knorr, *J. Mater. Res.* **5** 989 (1990).

M. N. Baibich, J. M. Broto, A. Fert, F. Nguyen Van Dau, F. Petroff, P. Etienne, G. Greuzet, A. Friederich, and J. Chazelas, *Phys. Rev. Lett.* **61**, 2472 (1988).

H. Baker (editor), *Alloy Phase Diagrams*, Vol. 3, ASM Handbook, ASM International, 1992.

L. Baril, B. Gurney, D. Wilhoit, and V. Speriosu, submitted to *J. Appl. Phys.* **85** 5139 (1999).

J. H. Basson and C. A. B. Ball, *Phys. stat. Sol. a* **46**, 707 (1978).

J. Belleson and Ed. Grochowski, *IBM Website* (www.IBM.com), Feb. 1999.

A. J. Bennett and B. R. Cooper, *Phys. Rev. B* **3**, 1642 (1971).

G. Bertotti, *Hysteresis in Magnetism for Physicists, Materials Scientists, and Engineers*, Academic Press, Inc., 1998.

H. Neal Bertram and D. I. Paul, *J. Appl. Phys.* **82**, 2439 (1997).

J.A.C. Bland and B. Heinrich, *Ultrathin Magnetic Structure I*, eds. B. Heinrich and J.A.C. Bland, Springer-Verlag Berlin Heidelberg, 1 (1994).

W. A. Brantley, *J. Appl. Phys.* **44**, 534 (1973).

Gabriel Bochi, O. Song, and R. C. O'Handley, *Phys. Rev. B 50*, 2043 (1994).

Gabriel Bochi, *Ph. D. Thesis*, Department of Materials Science and Engineering, Massachusetts Institute of Technology, June, 1995.

Gabriel Bochi, C. A. Ballentine, H. E. Inglefield, C. V. Thompson, and R. C. O'Handley, *Phys. Rev. B* **53**, R1729 (1996).

R. M. Bozorth, *Ferromagnetism*, IEEE Press, 1978.

P. Bruno, *J. Phys. F: Met. Phys.* **18** 1291 (1988).

D. S. Campbell, *Handbook of Thin Film Technology*, Edited by Leon I. Maissel and Reinhard Glang, McGraw-Hill, Inc., 1970.

W. J. Carr, Jr., *Magnetism and Metallurgy*, Vol. 1, editors: A. E. Berkowitz and E. Kneller. p. 45.

C-A Chang, *Appl. Phys. Lett.* **57**, 2239 (1990a).

C-A Chang, *J. Appl. Phys.* **68** 4873 (1990b).

C. Chappert and P. Bruno, *J. Appl. Phys.* **64**, 5736 (1988).

Y. Chen, S. T. Tong, J. S. Kim, M. H. Mohamed, and L. L. Kesmodel, *Phys. Rev. B* **43**, 6788 (1991).

S. Chikazumi; *Physics of Ferromangetism*, Oxford Science Publications, Second Edition, 1997.

D. S. Chuang, C. A. Ballentine, and R. C. O'Handley, *Phys. Rev. B* **49**, 15084 (1994).

B. D. Cullity, *Introduction to Magnetic Materials*, Addison-Wesley Publishing Company, 1972.

B. G. Demczyk, R. Naik, G. Auner, C. Kota, and U. Rao, *J. Appl. Phys.* **75**, 1956 (1994).

F. J. A. den Broeder, W. Hoving, and P. J. H. Bloemen, *J. Magn. Magn. Mater.* **93**, 562 (1991).

B. Engel, C. D. England, R. A. Van Leeuwen, M. H. Wiedmann, and C. M. Falco, *Phys. Rev. Lett.* **67**, 1910 (1991).

L. M. Falicov, D. T. Pierce, S. D. Bader, R. Gronsky, K. B. Hathaway, H. J. Hopster, D. N. Lambeth, S. S. S. Parkin, G. Prinz, M. Salamon, I. K. Schuller, and R. H. Victora, *J. Mater. Res.* **5**, 1299 (1990).

M. Farle, B. Mirwald-Schulz, A. N. Anisimov, W. Platow, and K. Barberschke, *Phys. Rev. B* **55**, 3708 (1997).

P. J. Flanders and C. D. Graham Jr., *Rep. Prog. Phys.* **56**, 431 (1993).

Simon Foner, *Rev. Sci. Instr.* **30**, 548 (1959).

J. Gay and R. Ritchter, *Phys. Rev. Lett.* **56**, 2728 (1986).

U. Gradmann, *Ann Physik* **7**, 161 (1966).

U. Gradmann, *J. Magn. Magn. Mater.* **54-57**, 733 (1986).

U. Gradmann, *Handbook of Magnetic Mateirals*, Vol. 7, ed. K. H. J. buschow (Amsterdam: Elsevier), 27 (1993).

De-Hua Han, Jian-Gang Zhu, Jack H. Judy, and John M. Sivertsen, *Appl. Phys. Lett.* **70**, 664 (1997).

B. Heinrich, J. F. Cochran, A. S. Arrott, S. T. Purcell, K. B. Urquhart, J. R. Dutcher, and W. F. Egelhoff, Jr., *Appl. Phys. A* **49**, 473 (1989).

M. A. Herman and H. Sitter, *Molecular Beam Epitaxy, Fundamentals and Current Status*, Springer-Verlag, Second Ed., 1996.

J. P. Hirth and J. Lothe, *Theory of Dislocations*, Krieger Publishing Company, Reprint Edition, 1992.

D. W. Hoffman and J. A. Thornton, *J. Vac. Sci. Tech.* **20**, 355 (1982).

S. Hope, J. Lee, P. Rosenbusch, G. Lauhoff, J. A. C. Bland, and A. Ercole, *Phys. Rev. B* **55**, 11422 (1997).

F. Huang, M. T. Kief, G. J. Mankey, and R. F. Willis, *Phys. Rev. B* **49**, 3962 (1994).

D. Hull and D. J. Bacon, *Introduction to Dislocations*, Pergamon Press, Reprint Edition, 1992.

H. E. Inglefield, C. A. Ballentine, G. Bochi, S. Bogomolov, R. C. O'Handley, and C. V. Thompson, *Proceedings of the MRS Spring 1993 Meetings*, San Franscisco, CA.

H. E. Inglefield, *Ph. D. Thesis*, Department of Materials Science and Engineering, Massachusetts Institute of Technology, June 1995.

W. A. Jesser and J. W. Matthews, *Phil. Mag.* **15**, 1097 (1967).

M. Johnson, *IEEE Spectrum*, 47 (May 1994).

M. T. Johnson, P. J. H. Bloemen, F. J. A. den Broeder, and J. J. de Vries, *Rep. Prog. Phys.* **59**, 1409 (1996).

J. P. Joule, *Phil. Mag.* **3**, 30, 76; 225, 1847.

R. Jungblut, M. T. Johnson, J. an de Stegge, A. Reinders, and F. J. A. den Broeder, *J. Appl. Phys.* **75**, 6424 (1994).

E. Klokholm, *IEEE Trans. Magn.* **12**, 819 (1976).

R. Koch, H. Leonhard, G. Thurner, and R. Abermann, *Rev. Sci. Instrum.* **61**, 3859 (1990).

R. Koch, *J. Phys.: Condens. Matter* **6**, 9519 (1994).

R. Koch, M. Weber, K. Thürmer, and K. H. Rieder, *J. Magn. Magn. Mater.* **159**, L11 (1996).

Etienne du Trémolet de Lacheisserie, *Magnetostriction, theory and applications of magnetoelasticity*, CRC Press, Inc., 1993.

E. du Trémolet de Lacheisserie and J. C. Peuzin, *J. Magn. Magn. Mater.* **136**, 189 (1994).

E. du Trémolet de Lacheisserie, *Phys. Rev. B* **51**, 15929 (1995).

E. W. Lee, *Rep. Prog. Phys.* **18**, 184 (1955).

C. H. Lee, Hui Fe, F. J. Lamelas, W. Varva, C. Uher, and Roy Clarke, *Phys. Rev. B* **42**, 1066 (1990).

J. Li, J. W. Mayer, L. J. Matienzo, and F. Emmi, *Materials Chemistry and Physics* **32**, 390 (1992).

S. S. Lyer, M. Arienzo, and E. de Frésart, *Appl. Phys. Lett.* **57**, 893 (1990).

P. M. Marcus, *J. Magn. Magn. Mater.* **168**, 18 (1997).

J. W. Matthews and J. L. Crawford, *Thin solid films* **5** 187 (1970).

T. R. McGuire and P. J. Flanders, *Magnetism and Metallurgy*, Vol. 1, editors: A. E. Berkowitz and E. Kneller. p. 123.

K. P. Mukherjee, J. Bandyopadhyaya, and K. P. Gupta, *Trans. Am. Inst. Min. Eng.* **245**, 2335 (1969).

S. Müller, B. Schulz, G. Kostka, M. Farle, K. Heinz, and K. Baberschke, *Surface Science* **364**, 235 (1996).

R. Naik, C. Kota, J. S. Payson, and G. L. Dunifer, *Phys. Rev. B* **48**, 1008 (1993).

L. Néel, *J. Phys. Radium* **15**, 225 (1954).

L. F. Nye, *Physical Properties of Crystals*, Oxford Science Publications, Reprint, 1990.

R. C. O'Handley and S. W. Sun, *J. Magn. Magn. Mater. 104-107*, 1717 (1992).

R. C. O'Handley, O. Song, and C. A. Ballentine, *J. Appl. Phys.* **74**, 6302 (1993).

M. Ohring, *The Materials Science of Thin Films*, Academic Press, Inc., 1992.

E. Orowan, *Z. Phys.* **89**, 634 (1934).

Polanyi, *Z. Phys.* **89**, 660 (1934).

G. Prinz and K. Hathaway, *Physics Today*, 24 (April 1995).

G. Prinz, *Science* **282**, 1660 (1998).

S. T. Purcell, M. T. Johnson, N. W. E. McGee, W. B. Zeper, and W. Hoving, *J. Magn. Magn. Mater. 113*, 257 (1992).

R. E. Reed-Hill and R. Abbaschian, *Physical Metallurgy Principles*, Third Edition, PWS-KENT Publishing Company, 1992.

S. Rengarajan, B. H. Lee, G. Choe, and R. M Walser, *IEE Trans. Magn.* **31**, 3391 (1995).

D. Sander, R. Skomski, A. Enders, C. Schmidthals, D. Reuter, and J. Kirschner, *J. Phys. D: Appl. Phys.* **31**, 663 (1998).

B. Schulz and K. Baberschke, *Phys. Rev. B* **50**, 13467 (1994).

J. Shen, J. Giergiel, and J. Kirshner, *Phys. Rev. B* **52**, 8454 (1995).

D. Smith, *Thin-Film Deposition, Principles and Practice*, McGraw-Hill, Inc. 1995.

O. Song, C. A. Ballentine, and R. C. O'Handley, *Appl. Phys. Lett.* **64**, 2593 (1994).

M. Stampanoni, A. Vaterlaus, M. Aeschlimann, and F. Meier, *Phys. Rev. Lett.* **59**, 2483 (1987).

R. L. Stamps, L. Louail, M. Hehn, M. Gester, and K. Ounadjela, *J. Appl. Phys.* **81**, 4751 (1997).

S. W. Sun and R. C. O'Handley, *Phys. Rev. Lett.* **66**, 2798 (1991).

H. Takayama, K. P. Bohnen, and P. Fulde, *Phys. Rev. B* **14**, 2287 (1976).

Andrew C. Tam and Holger Schroeder, *IEEE Trans. Magn.* **25**, 2629 (1989).

G. I. Taylor, *Proc. Roy. Soc. A* **145**, 362 (1934).

J. Y. Tsao, *Materials Fundamentals of Molecular Beam Epitaxy*, Academic Press, Inc., 1993.

C. Uiberacker, J. Zabloudil, P. Weinberger, L. Szunyogoh, and C. Sommers, *Phys. Rev. Lett.* **82**, 1289 (1999).

R. H. Victora and J. M. MacLaren, *Phys. Rev. B* **47**, 11583 (1993).

G. Weber, G. Billot, and P. Barret, *Physica Status Solidi a* **75**, 567 (1983).

M. Weber, R. Koch and K. H. Rieder, *Phys. Rev. Lett.* **73**, 1166 (1994).

D. B. Williams and C. B. Carter, *Transmission Electron Microscopy, A Textbook for*

Materials Science, Plenum Press, 1996.

R. Q. Wu, J. J. Chen, A. Shick, A. J. Freeman, *J. Magn. Magn. Mater.* **177-181** 1216 (1998).

R. Zuberek, H. Szymczak, R. Krishmnan, and M. Tessier, *J. Phys. (Paris)*, Colloq. **49**, C8-1761 (1988).

Biographical Note

The author of this thesis, Kin Ha, is an ethnic Chinese who was born in Da Nang, Vietnam. He left the country with his family in the summer of 1978, on a boat to Taiwan. There, in a military camp, playing basketball and guitar were usually the activities of the day.

Kin came to Los Angeles in the fall of 1979, knowing about 100 words in the English language. He attended King Jr. High School. Belmont high school was the place where the author's potential was tapped. The author graduated first in his class in 1985.

The first year at Caltech was difficult. "Electricity and Magnetism" by Purcell was hellish. There were opportunities for a well-rounded education. The author received his Bachelor's of Science in Applied Physics and in Economics with high honors from Caltech in June of 1990.

Working for Oracle was a good experience. The project in Austin was fun. There, incubated in the dense pollen Texas environment, Kin has become a sensitive pollen detector since.

The author came to MIT in September of 1991. The transition from Physics to Materials Science was rough. The qualifier was difficult. This thesis was written when the author was a Teaching Assistant for 3.21 (a graduate course in Kinetic Processes in Materials).

The author took a leave of absence from MIT for seven months to work for Rocky Mountains Magnetics (it is now Quantum Corporation) in Colorado.

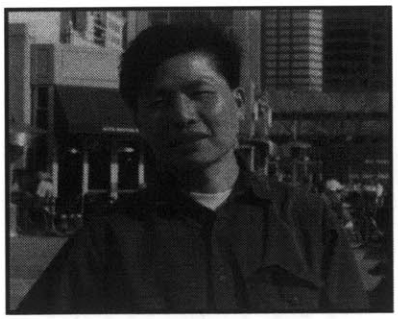

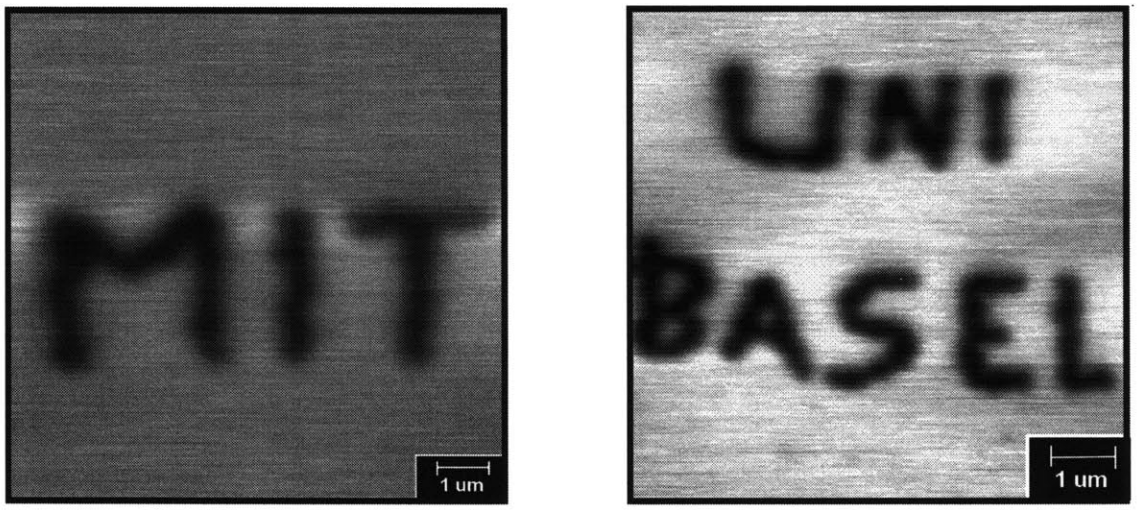

MFM Images of a Cu/Ni(75Å)/Cu/Si(001) film: the film was grown by Dr. Gabriel Bochi at MIT. The writing and imaging were done by Dr. Hans Hug at the University of Basel, Switzerland using a magnetic force microscope.